Molybdenum sulfide as efficient hydrogen evolving catalyst for light-induced water splitting

vorgelegt von
M. Sc.
Fanxing Xi
ORCID: 0000-0003-4252-6652

von der Fakultät III - Prozesswissenschaften
der Technischen Universität Berlin
zur Erlangung des akademischen Grades

Doktorin der Ingenieurwissenschaften
- Dr.-Ing. -
genehmigte Dissertation

Promotionsausschuss:

Vorsitzender: Prof. Dr. John Banhart
Gutachter: Prof. Dr. Frank Behrendt
Gutachter: Prof. Dr. Sebastian Fiechter

Tag der wissenschaftlichen Aussprache: 16. Mai 2019

Berlin 2019

Ich erkläre hiermit, dass ich die vorliegende Arbeit selbständig verfasst und keine anderen als die angegebenen Quellen und Hilfsmittel verwendet habe.

Berlin, den December 13, 2019

Abstract

In the presented work, molybdenum sulfide is investigated as a catalyst for hydrogen evolution reaction (HER) and CO_2 reduction reaction (CO_2RR). This thesis mainly consists of three parts: (i) a study of the catalytic performances and catalytic mechanism of semiconducting $(NH_4)_2Mo_3S_{13}$ cluster as an electro-catalyst and as a co-catalyst for WSe_2 photocathode, (ii) a study of the phase transformation during the activation of amorphous MoS_x catalyst prepared by reactive magnetron sputtering, (iii) on the role of sputtered molybdenum sulfide on gas diffusion electrodes as a candidate of CO_2RR catalyst.

In the first part, the performance of $(NH_4)_2Mo_3S_{13}$ cluster material is studied as an electro-catalyst for HER. Density functional theory (DFT) calculations are used to identify the catalytically active centers. The thermal stability is also studied in this part. From Kelvin Probe and UV-vis experiments, it can be concluded that this cluster material has the properties of an intrinsic semiconductor. When depositing $(NH_4)_2Mo_3S_{13}$ on a WSe_2 photocathode, the photocurrent of the electrode increased from $0.02\,mA/cm^2$ to $2.4\,mA/cm^2$ at $0\,V$ vs RHE. It is proposed in this chapter that $(NH_4)_2Mo_3S_{13}$ passivates surface states on the WSe_2 electrode, forms a heterojunction with WSe_2 and increases the photoelectrochemical (PEC) performance of the electrode.

In the second part, molybdenum sulfide, deposited by reactive magnetron sputtering, is investigated. The best catalytic activity was obtained from room temperature sputtered, amorphous MoS_x which initially has a structure consisting of linked Mo_3S_{13} and Mo_3S_{12} entities. An improvement of the catalytic activity was observed at the beginning of the electrochemical measurement, along with the release of H_2S. By *in-situ*/in-line Raman measurements, a phase transformation of the RT sputtered MoS_x, from an amorphous structure of Mo_3S_{13} and Mo_3S_{12} clusters to a MoS_{2-x} layer-like structure with sulfur defects on the edge site of S-Mo-S slabs, could be detected.

In the last part, molybdenum sulfide layers prepared on GDEs by reactive magnetron sputtering were tested as candidates for CO2RR catalyst. Combing electrochemical measurements with mass spectrometry, head space gas chromatography and high performance liquid chromatography, the products could be detected and studied.

Kurzfassung

In dieser Arbeit wird Molybdänsulfid als Katalysator für die Wasserstoffentwicklungsreaktion (HER) und CO_2-Reduktionsreaktion (CO_2RR) untersucht. Sie besteht im Wesentlichen aus drei Teilen: (i) einer Studie über die katalytischen Leistungen und den katalytischen Mechanismus der halbleitenden Clusterverbindung $(NH_4)_2Mo_3S_{13}$ als Elektrokatalysator und als Co-Katalysator für WSe_2-Photokathoden, (ii) einer Studie über die Phasenumwandlung während der Aktivierung von amorphem MoS_x, hergestellt durch reaktives Magnetronsputtern, (iii) der Rolle von gesputtertem Molybdänsulfid in Kombination mit Gasdiffusionselektroden (GDE) für die CO_2RR.

Im ersten Teil wird die Leistung von $(NH_4)_2Mo_3S_{13}$ als Elektrokatalysator für die HER untersucht. DFT-Berechnungen (Density Functional Theory) werden verwendet, um die katalytisch aktiven Zentren zu identifizieren. Die thermische Stabilität wird in diesem Teil ebenfalls untersucht. Aus Experimenten mit der Kelvin-Sonde und der UV-VIS-Spektroskopie kann geschlossen werden, dass dieses Clustermaterial die Eigenschaften eines intrinsischen Halbleiters aufweist. Beim Abscheiden von $(NH_4)_2Mo_3S_{13}$ auf eine WSe_2-Photokathode stieg der Photostrom der Elektrode von $0.02\,mA/cm^2$ auf $2.4\,mA/cm^2$ bei 0 V vs. RHE. In diesem Kapitel wird vorgeschlagen, dass $(NH_4)_2Mo_3S_{13}$ Oberflächenzustände an der WSe_2-Elektrode passiviert, eine Heterostruktur mit WSe_2 bildet und die photoelektrochemische (PEC) Leistung der Elektrode erhöht.

Im zweiten Teil wird mittels reaktivem Magnetronsputtern abgeschiedenes Molybdänsulfid untersucht.Die beste katalytische Aktivität wurde aus dem bei Raumtemperatur gesputterten, amorphen MoSx erzielt, das eine Struktur aufweist, welche aus verknüpften Mo_3S_{13}-und Mo_3S_{12}-Einheiten besteht. Eine Verbesserung der katalytischen Aktivität wurde zu Beginn der elektrochemischen Messung beobachtet, zusammen mit einer Freisetzung von H_2S. Durch *in-situ*/in-line Raman-Messungen konnte eine Phasenumwandlung des bei Raumtemperatur gesputterten MoSx von einer amorphen Struktur aus Mo_3S_{13}- und Mo_3S_{12}-Clustern zu einer schichtartigen MoS_{2-x} Struktur mit Schwefeldefekten an den Kanten der S-Mo-S-Platten nachgewiesen werden.

Im letzten Teil wurden Molybdänsulfidschichten mittels reaktivem Magnetronsputtern auf GDEs abgeschieden und als Katalysatoren zur CO_2RR getestet. Durch die Kombination elektrochemischer Messungen mit Massenspektrometrie, Headspace-Gaschromatographie und Hochleistungsflüssigkeitschromatographie konnten die Produkte erkannt und untersucht werden.

Contents

List of Figures

List of Tables

Chapter 1

Introduction

1.1 High energy demand, CO_2 emissions and climate change

Since the industrial revolution, technology and economy have experienced tremendous growth accompanied by a large increase of human population. Presently, about 7.7 billion people are living on this planet, consuming about 18.5 TWy/y of energy, corresponding to 1.62×10^{14} kWh/year. This number is still growing rapidly, especially due to the demand from developing countries. Currently among all consumed energy, over 80% comes from fossil fuels, including oil, gas, and coal. However, these energy resources are not renewable and they will be depleted in a relatively short time. In fact, there have been many debates already on the topic of "when the fossil fuels will be consumed". As estimated by Topal et al. in 2009, [30] the fossil fuel reserve depletion times for oil, coal and gas are approximately 35, 107 and 37 years, respectively.

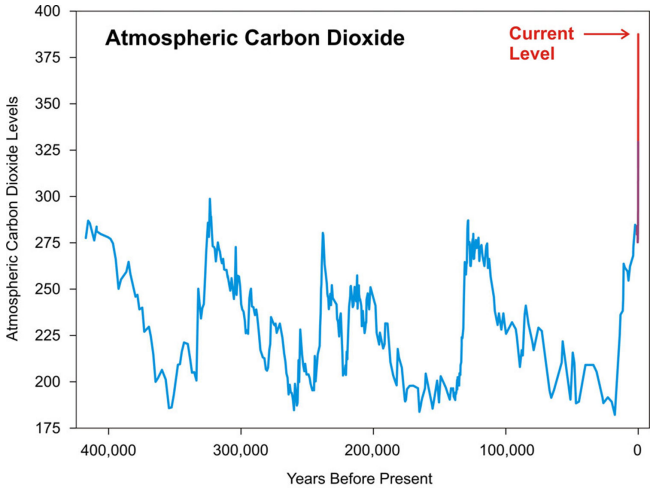

Figure 1.1: *Atomspheric CO_2 level in history [1]*

In addition to the limited amount and unsustainable nature of fossil fuels, the mining procedures of fossil fuels, such as brown and hard coal, and crude oil, are usually not environmental friendly processes, most critically due to the resulting air pollution including flying ashes and various gases produced during the combustion of fossil fuels, such as CO_2, SO_2, and NO_x. Since sulfur oxides are harmful to health and the environment, a desulfurization process has been introduced, which largely reduces the sulfur content in fossil fuels and the production of sulfur oxides during combustion. However, the amount of CO_2 released by burning fossil fuels cannot be prevented since the fuels themselves consist mostly of carbon and hydrocarbons.
Ideally, the level of atmospheric CO_2 has its own balance since CO_2 is a necessary source for photosynthesis of plants and other organisms; it is naturally produced by respiration and artificially by industry and household. [29]. However, because of the high rate of CO_2 release by human activities, consuming fossil reserves that accumulated slowly over billions of years, the balance has now been extremely disrupted. [29] According to list source, the atmospheric CO_2 level amounted to 410 ppm [1] in February 2019. However, the level was only 280 ppm at the beginning of the industrial revolution. Fig. 1.1 shows the historical atmospheric CO_2 level during the last 400,000 years. It clearly shows that our CO_2 level is currently over 100 ppm higher than at any other time in the past 400,000 years.

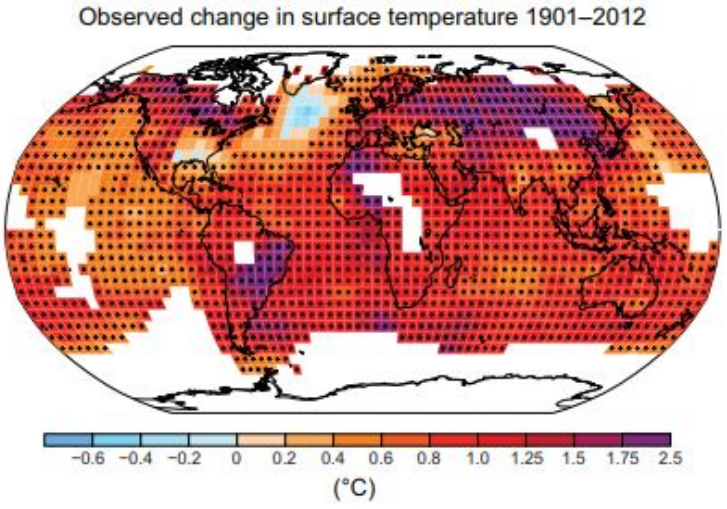

Figure 1.2: *Map of observed surface temperature change from 1901 to 2012 [2]*

As we know, CO_2 is a green house gas and one of the main reasons for climate change, due to its heat-trapping nature. Signs of climate change, such as rising global temperature, warming oceans, shrinking ice sheets and ocean acidification, have already been observed, connected to the dramatically increasing level of atomspheric

CO_2. Effects of global warming predicted by scientists are now occuring as well, including sea level rise, extreme weather conditions, such as long lasting droughts and heat waves. [31] Fig. 1.2 shows the surface temperature change on Earth from 1901 to 2012, and it's evident that most places have experienced an overall temperature rise during this time period.
Therefore, to prevent global warming and to decrease the atmospheric CO_2 level, efforts must be made to find cleaner energy resources and convert CO_2 released by burning fossil fuels back into hydrocarbons or other stable forms.

1.2 Solar fuels as a promising solution

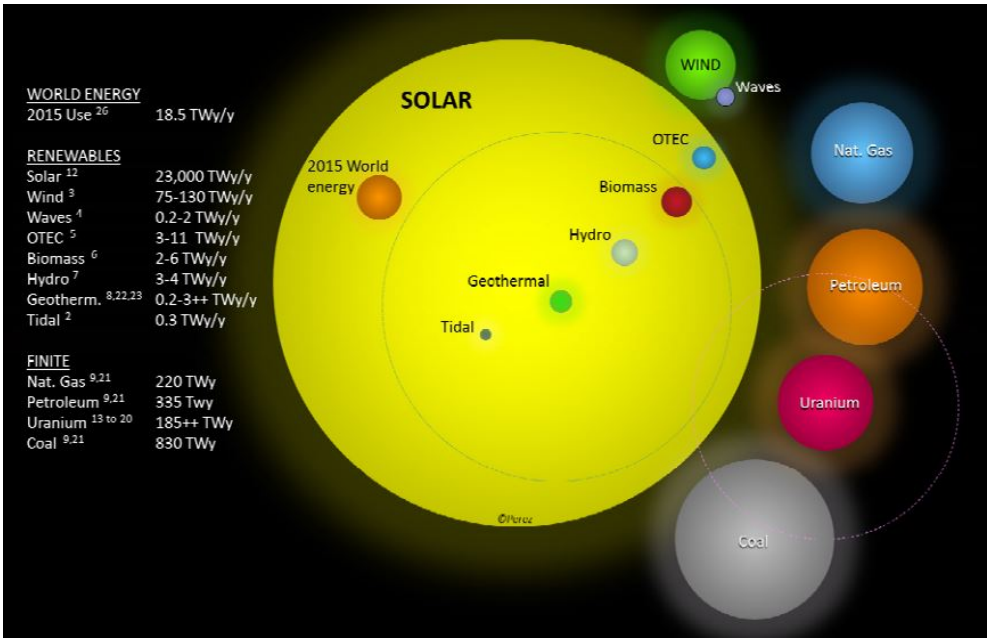

Figure 1.3: *Estimated finite and renewable planetary energy reserves (Terawatt-years) in 2015 [3]*

Fig. 1.3 shows the estimated renewable energy resources and finite energy reserves in 2015. It is obvious from the figure that the Sun is one of the most important sustainable energy resources, and compared to other renewable energy resources, such as wind, biomass or hydro power, solar energy is the only renewable source which can sufficiently meet the energy consumption of the world. In fact, the amount of energy consumed by human beings annually, which is about 5.8×10^{20} joules, can be delivered to the Earth by the Sun in about one hour. [32] Therefore, solar energy has great potential to become a practical alternative to fossil fuels. To use solar energy, efforts have been made to discover efficient ways to convert solar energy to other kinds of energy that can be directly used by human beings, such as electricity [33],

fuels [8] and heat [34].

However, one big drawback of solar energy is its intermittency. The availability of sunlight highly depends on geographical location, weather condition, season, and the day/night cycle. In addition, there is usually a temporal mismatch between the peak of the solar energy supply and the peak of humanity's energy demand, which makes the large-scale energy storage particularly important. Table 1.1 shows the energy densities of various energy storage techniques. Compared to capacitors, batteries and mechanical-based storage, fuels normally have 2-3 orders of magnitude higher gravimetric energy density [35] since the energy is stored in concentrated form by chemical bonds and the energy could be easily extracted from fuels just by combustion. [36] Additionally, over 80% of all energy is consumed in the form of fuel nowadays, so infrastructure for utilizing fuels already exists. Therefore, fuels represent one good option for the energy carrier of solar energy conversion, which leads us to the main topic of our research: solar fuels.

Table 1.1: *Gravimetric and volumetric energy densities of various energy carriers [25–27]*

Energy carriers	**Gravimetric energy density(MJ/kg)**	**Volumetric energy density(MJ/L)**
Fuels		
Coal	24	–
Gasoline	44	35
Diesel	46	37
Methanol	20	18
Natural gas	54	0.036
Hydrogen	143	0.011(1 bar)/5.6(700 bar)
Batteries		
Pb	~ 0.14	–
Li-ion	$\sim$0.9	–
Mechanical		
Compressed air	0.512	
Pump water uphill	0.001(100 m)	0.001(100 m)
Flywheels	1.1	–

Solar fuels are definded as the production of fuels via direct or indirect solar energy conversion. There are many possible ways to synthesize fuels with solar energy and also many possible fuels with potential to store energy such as hydrogen and hydrocarbons. This approach requires components for both light-absorbing and catalysis. [37] The light-absorber provides the electric potential to drive the fuel-generating reactions, while catalysts minimize the overpotentials and increase the reaction speed. In this thesis, I will discuss the process of developing catalysts

for hydrogen evolution reaction (HER) in solar-driven water splitting and for CO_2 reduction reaction (CO_2RR) as well.

1.3 Solar driven water splitting

1.3.1 Basic principles of solar driven water splitting

Hydrogen represents a clean and environmental-friendly energy carrier of the future with high energy density per mass (143 MJ/kg)as shown in Table. 1.1. It also doesn't emit CO_2 during combustion. Fig. 1.4 shows the main processes in industy for producing hydrogen. Among these methods, steam reforming using methane or coal with water is the most commonly-used method. There are some drawbacks to this method though, as methane and coal themselves are non-renewable energy resources and CO_2 is emitted during the H_2 production. However, using solar-driven water splitting, hydrogen can be produced from water, a much more convenient and abundant, clean resource compared to coal or methane. Therefore, solar-driven water splitting could be one of the most desirable methods to produce hydrogen in a clean and environmental-friendly way. [38]

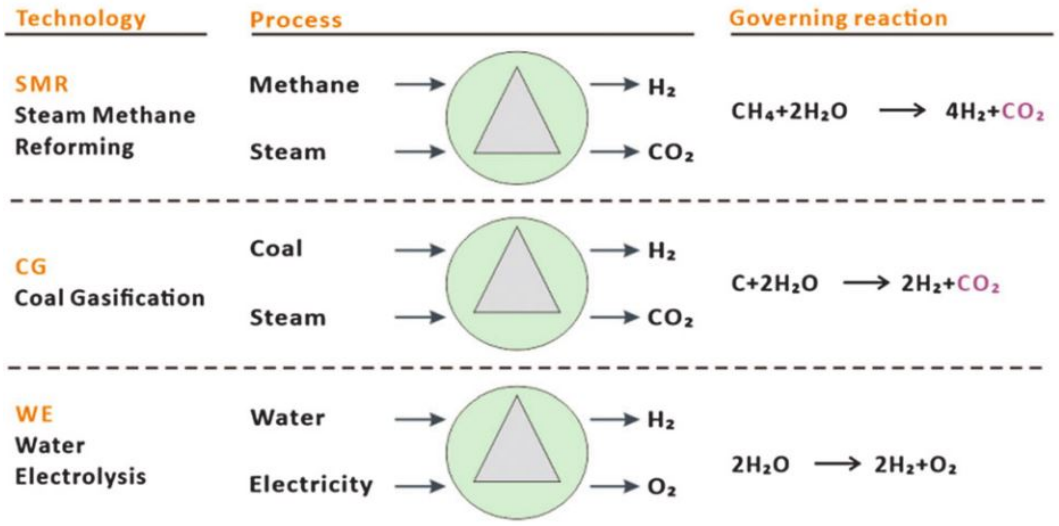

Figure 1.4: *Main methods for industrial hydrogen production [4]*

The overall reaction for water electrolysis is:

$$H_2O \rightleftarrows H_2 + \frac{1}{2}O_2 \qquad \Delta G = 238\,\mathrm{kJ/mol} \tag{1.1}$$

And in electrochemistry, this equation can be also formulated as:

$$H_2O \rightleftarrows H_2 + \frac{1}{2}O_2 \qquad \Delta E^0 = -1.23\,\mathrm{V} \tag{1.2}$$

There are two half reactions in water splitting. The oxygen evolution reaction (OER) happens in the anodic side while the hydrogen evolution reaction (HER) occurs at the cathodic side.
For an alkaline electrolyte (pH 14), the HER and OER can be written as:

$$4H_2O + 4e^- \rightleftarrows 2H_2 + 4OH^- \qquad {E_{\mathrm{red}}}^0 = -0.83\ Vvs.\ NHE \tag{1.3}$$

$$4OH^- \rightleftarrows O_2 + 2H_2O + 4e^- \qquad {E_{\mathrm{ox}}}^0 = +0.40\ Vvs.\ NHE \tag{1.4}$$

While in an acidic electrolyte (pH 0), the following equations are formulated:

$$4H^+ + 4e^- \rightleftarrows 2H_2 \qquad {E_{\mathrm{red}}}^0 = 0.00\ Vvs.\ NHE \tag{1.5}$$

$$2H_2O \rightleftarrows 4H^+ + O_2 + 4e^- \qquad {E_{\mathrm{ox}}}^0 = +1.23\ Vvs.\ NHE \tag{1.6}$$

In these equations, NHE stands for normal hydrogen electrode. As shown by these equations, a voltage of at least 1.23 V is needed to drive the water splitting reaction at 25 °C and 1 bar. Different approaches are employed to realize water splitting using solar energy, among them photoelectrochemical (PEC) water splitting and PV-electrolysis (a water electrolyzer coupled with photovoltaic cells) are the most studied methods. Therefore in this thesis, these two systems are going to be briefly introduced.

PV-electrolysis

PV-electrolysis represents the combination of standalone PV-cells for converting solar energy into electric power, and separate electrodes with electro-catalysts to drive electrochemical reactions. [39] This concept has attracted much attention since the discrete PV cells and electrolyzer can be investigated and optimized individually. Furthermore, there are already suited PV systems to provide sufficient current and voltage for water splitting. Fig. 1.5 shows the structure of a water splitting system, in which perovskite photovoltaic cells are coupled with an electrochemical cell that uses earth-abundant catalysts as described by Grätzel et al. [5] The system achieved 12.3% solar to hydrogen (STH) efficiency in 2014 but only for a short time because of the low stability of the perovskite solar cells.
Commercial electrolyzers for water splitting are normally operated at high current

density ($\sim$1 A/cm^2). Assuming an electrolyzer with an efficiency of 65% and operating voltage of 1.9 V, interconnected a PV cell of 12% efficiency, a STH efficiency of 7.8% can be achieved. [40]. To increase the electrolyzer efficiency, noble catalysts are used to minimize the overpotential, which unfortunately leads to an increase in overall cost. Hence, the price of hydrogen produced via PV-electrolysis is still more expensive than the price of hydrogen produced by steam reforming. For this reason, PV-electrolysis has not been commercially implemented. Nevertheless, PV-electrolysis still has a great potential and will be improved with advances in solar cells, catalysts, and electrolysis technologies.

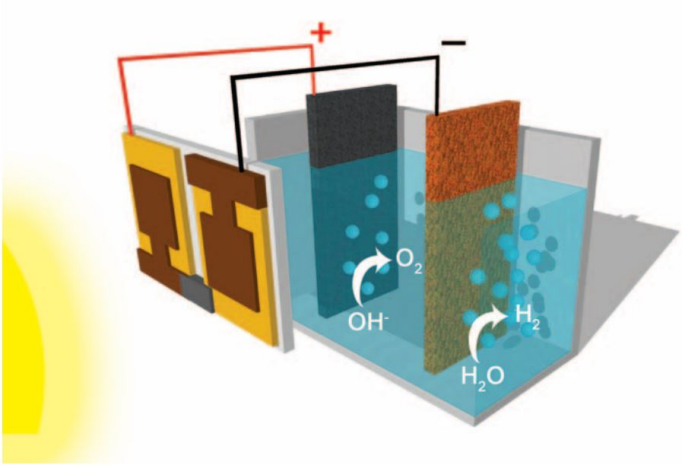

Figure 1.5: *Scheme of electrolysis cell coupled with perovskite solar cells [5]*

PEC water splitting

Potential improvements in cost, efficiency, and simplicity could be realized by directly intergrating the light harvesting and electrochemical steps. In 1968, Boddy, and four years later Honda and Fujishima, [41,42] investigated photoactive TiO_2 single crystal electrodes for PEC water splitting using semiconducting light-absorbers, this has become one of the most promising methods for solar driven water splitting. From the water splitting reaction equation (see Eq. 1.2), it is obvious that the semiconducting material to be used as photoelectrode in PEC devices should be able to provide photovoltage of at least 1.23 V to drive both half reactions in water splitting (see equations from Eq. 1.3 to 1.6). Additionally, to provide additional overpotential to overcome the kinetic energy barriers in both OER and HER, which are typically about 0.4 V and 0.2 V at a current density of 10 mA/cm^2, the photovoltage must exceed 1.8 V. Since it has so far proven difficult to reach this level from single junction device, tandem divices are sometime used to harvest more of the solar

spectrum while generating additive photovoltage, for instance, solar cells made from silicon or gallium arsenide can be coupled with the photoactive binary and tenary oxide electrodes. [43] Other requirements for the semiconducting photoelectrode material are high (visible) light absorption, high chemical stability in the electrolyte under both dark and illumination conditions, low cost, and proper band alignment with respect to the water reduction and oxidation potentials. [44] Researchers have studied many different semiconductors for PEC applications, such as multi-junction III-V semiconductors by Turner et al. [45] in 1998, and by Cheng et al. [46] in 2018 who achieved 19.3% solar to hydrogen (STH) efficiency. However, the stability of the III-V semiconductors in electrolyte remains problematic as well as the high cost of these multi-junction solar cells. For this reason, Earth-abundant metal oxide photoelectrodes with relatively high stability and low cost have attracted much interests. Among them are $BiVO_4$, [43] α-Fe_2O_3, [47] and $CuBi_2O_4$. [48] Fig. 1.6 shows different metal oxides that have been studied for PEC devices and their band edge positions with respect to the redox potentials of H^+/H_2 and H_2O/O_2.

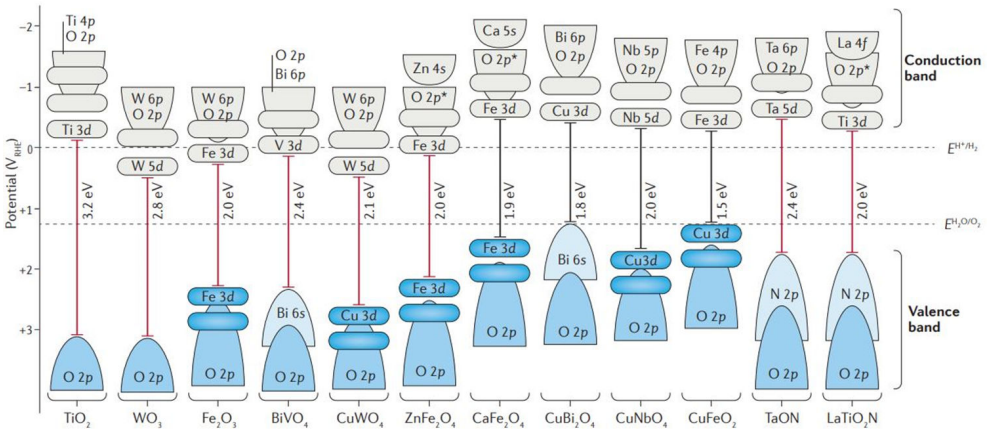

Figure 1.6: *Band structures of various metal oxides and oxynitrides for PEC application [6]*

The most simple setup to realize water splitting with a PEC device would be a n-type photoanode with a counter electrode (CE) or a p-type photocathode with a CE. Fig. 1.7A shows a possible structure of such a simple PEC cell. In the illustrated case, electron-hole pairs (e^--h^+) are generated in the n-type semiconductor $BiVO_4$, which has been deposited on a transparent conductive substrate, and then separated in the space charge region near the interface with electrolyte. Under this condition, holes move towards the semiconductor/electrolyte interface driving the OER (see Eq. 1.4 and Eq. 1.6). The electrons move in the opposite direction towards the external circuit and reduce water or protons on the CE/electrolyte interface (see

Eq. 1.3 and Eq. 1.5). A simplified energy diagram of the PEC water splitting cell with related reaction equations is shown in Fig. 1.7B.

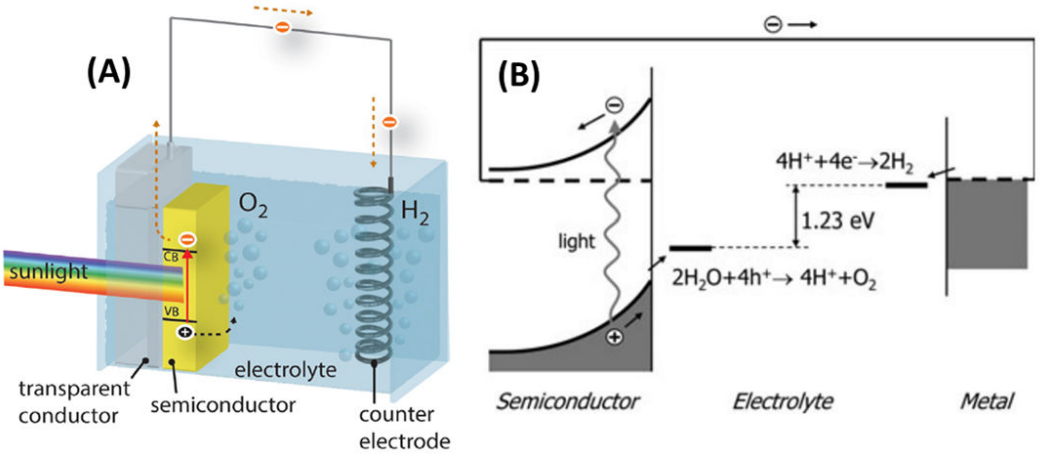

Figure 1.7: *(A) Scheme of a PEC water splitting device with n-type bismuth vanadate semiconductor as photoanode achieving a potential of at least* 1.23 V *and a metal wire as counter electrode in aqueous electrolyte [7]; (B) energy diagram of the PEC cell with respect to the position of the redox potentials of* H^+/H_2 *and* H_2O/O_2 *[8]*

1.3.2 Catalysts for water splitting

Typical polarization curves for HER and OER are shown in Fig. 1.8A. As mentioned above, certain overpotentials are needed to overcome the kinetic limitations during (photo)electrochemical water splitting. In this figure, it is shown that OER normally requires a higher overpotential than HER. The reason for the overpotential difference is because only two electrons need to be transferred in HER while four are needed in OER to form the O=O double bond [49] which makes the kinetics sluggish and therefore the overpotential high. In fact, these overpotentials can be minimized by using suited catalysts. Therefore, no matter if PV-electrolysis or PEC water splitting system is used, efficient catalysts are necessary for both HER and OER.

Enormous efforts have been made to find catalysts with high performance for water splitting including OER and HER. Fig. 1.8B shows different catalysts for HER and OER in alkaline and acidic conditions. Their electrocatalytic performance is depicted by their overpotentials at a current density of 10 mA/cm^2. It is shown in this figure that OER requires generally higher overpotentials, as mentioned before. In general, an OER catalyst with overpotential of 300-400 mV at 10 mA/cm^2 is considered as an excellent catalyst while there are many HER catalysts with overpotential

less than 200 mV. Only a limited number of OER catalysts work in acidic electrolyte, while a large amount of HER catalysts are functional under both alkaline and acidic conditions. The low activity of water oxidation at low potentials is a major obstacle for water splitting. [50] Discovering Earth-abundant catalysts with high catalytic activity and stability would be one of the key issues for efficient solar water splitting.

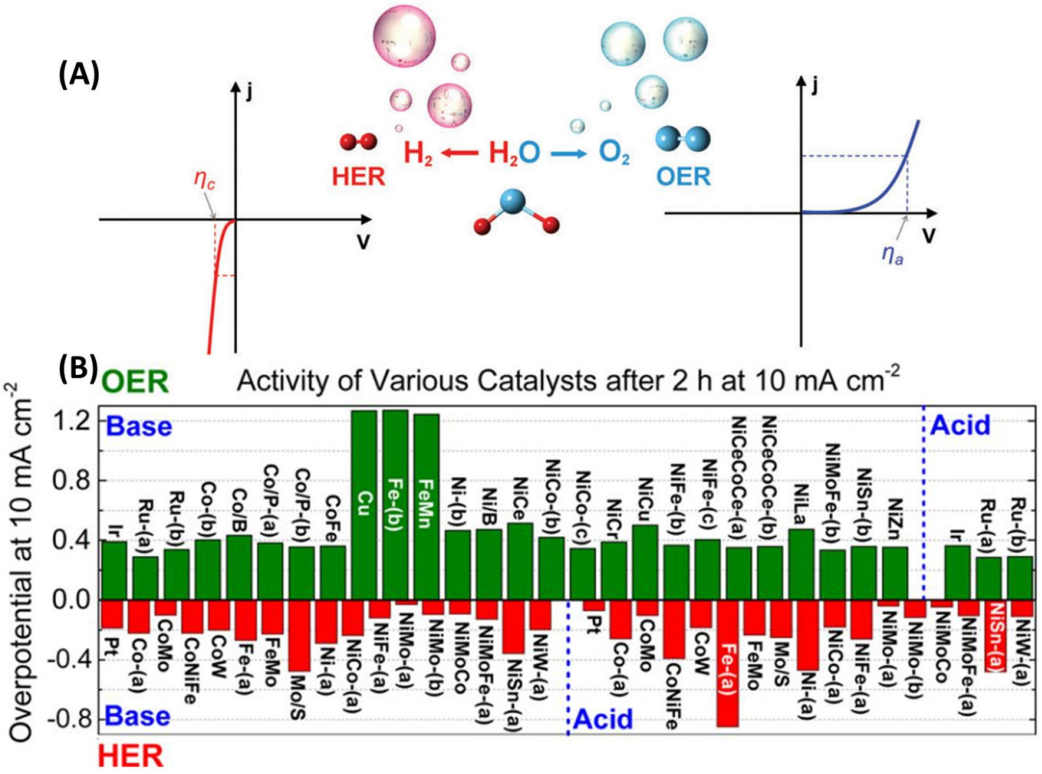

Figure 1.8: *(A) Typical polarization curves for HER and OER [9]; (B)Catalytic ability of various HER and OER catalysts in acidic and alkaline electrolytes [10]*

Mechanism and catalysts of OER

The mechanism of oxygen evolution is shown in Fig. 1.9. The reaction steps in case of acidic conditions are indicated by the blue lines. The reaction equations under acidic conditions can be written as:

$$M + H_2O \rightleftarrows MOH + H^+ + e^- \tag{1.7}$$

$$MOH \rightleftarrows MO + H^+ + e^- \tag{1.8}$$

$$MO + H_2O \rightleftarrows MOOH + H^+ + e^- \tag{1.9}$$

$$MOOH \rightleftarrows M + O_2 + H^+ + e^- \tag{1.10}$$

In Fig. 1.9, the red lines indicate the reactions under alkaline conditions which can be formulated as:

$$M + OH^- \rightleftarrows MOH \tag{1.11}$$

$$MOH + OH^- \rightleftarrows MO + H_2O + e^- \tag{1.12}$$

$$MO + OH^- \rightleftarrows MOOH + e^- \tag{1.13}$$

$$MOOH + OH^- \rightleftarrows M + O_2 + H_2O + e^- \tag{1.14}$$

Interestingly, it is also possible in both cases that two of the reaction intermediates (M-O) can react to form oxygen as shown by green lines in Fig. 1.9. This reaction equation is written as:

$$2MO \rightleftarrows 2M + O_2 \tag{1.15}$$

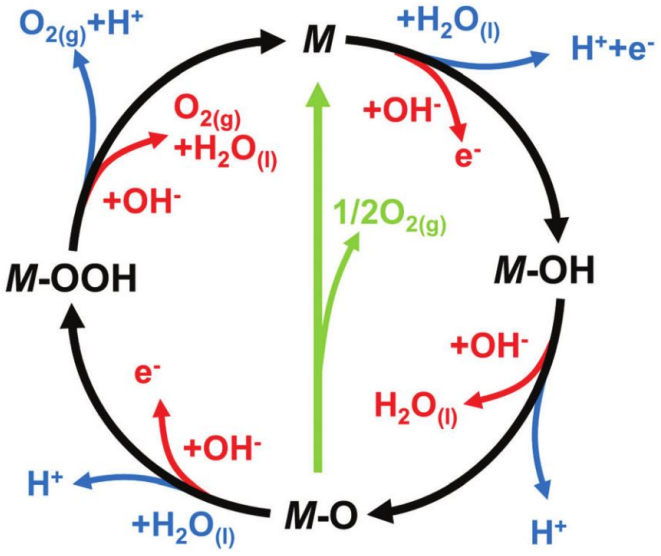

Figure 1.9: *The mechanism of OER in acidic (blue line) and alkaline (red line) electrolyte. Another mechanism possible in both conditions is two M-O intermediates reacting diretly to produce O_2 (green line) [9]*

The details of this complex reaction mechanism are still under debate, although, it is well accepted that OER is a heterogeneous process. It can be assumed that the bonding between metal M with reaction intermediates forming M-OH, M-O and M-OOH are crucial for the OER catalytic activity of the catalyst. [9]

The devolpment of a low-cost and efficient OER catalyst is critical since most conventional catalysts are based on precious metals [51] such as Pt, Ru and Ir [52], and their alloys and oxides. [53] For instance, rutile-type RuO_2 works remarkably as an OER catalysts in both acidic and alkaline electrolytes. [54] However, the material is not stable under high anodic potentials at which it can be oxidized to

RuO_4 which dissolves in the electrolyte. [55] Currently, there are already many studies on noble metal-free catalysts for OER such as metal oxides (cobalt, [56], and manganese oxides [57]), nickel hydroxides ($Ni(OH)_2$, [58]) and metal phosphates such as Co-Pi. [59] Some of these catalysts have achieved competitive performances with noble metal catalysts. For instance, a graphene oxide supported FeNi double hydroxide (FeNi-LDH/GO) was used as OER catalyst by Long et al. in 2014, [49] demonstrating an overpotential of 195 mV at 10 mA/cm^2.

Mechanism and catalysts of HER

The reaction equations of HER under alkaline and acidic conditions have been shown in Eq. 1.3 and Eq. 1.5. There are two steps in hydrogen evolution reaction: firstly proton reduction (also know as Volmer step), and secondly, hydrogen desorption. The equation of proton reduction, for instance, in an acidic electrolyte, can be expressed as:

$$H^+ + e^- + * \rightarrow H^* \tag{1.16}$$

Then for the hydrogen desorption step, two alternative reactions are possible. The first one is the so-called Heyrovsky step, expressed by the following equation:

$$H^+ + e^- + H^* \rightarrow H_2 \tag{1.17}$$

Or alternatively the Tafel step:

$$2H^* \rightarrow H_2 + 2* \tag{1.18}$$

In these equations, the asterisk * stands for an active site on the catalyst surface. For the hydrogen desorption step, one surface active site is needed in the Heyrovsky step, while in the Tafel step two active sites are needed. From these reactions, it can be said that a good catalyst for HER should be able to bind with hydrogen in the proton reduction step and hydrogen should be easy to release from the catalyst surface in the desorption step. This means that the Gibbs energy of chemisorbed H at material surface should be close to zero.

Jerkiewicz [60] and Barber et al. [61] have shown that trends in HER activity can be comparatively characterized in a so-called "volcano plot", in which the exchange current density (j_0) is plotted against a descriptor, such as the bond energy of H chemisorbed on material surface or alternatively the standard Gibbs energy of

chemisorption of H. [62] The exchange current density, which is the rate of HER per surface area at equilibrium, is usually used to demonstrate the ability of a catalyst to catalyze the HER. [63] In 2007, Jaramillo et al. [16] calculated the ΔG_{H^*} and measured the exchange current densities of different HER catalysts including MoS_2 and some metals such as Pt, Mo,Ni and so on as shown in Fig. 1.10.

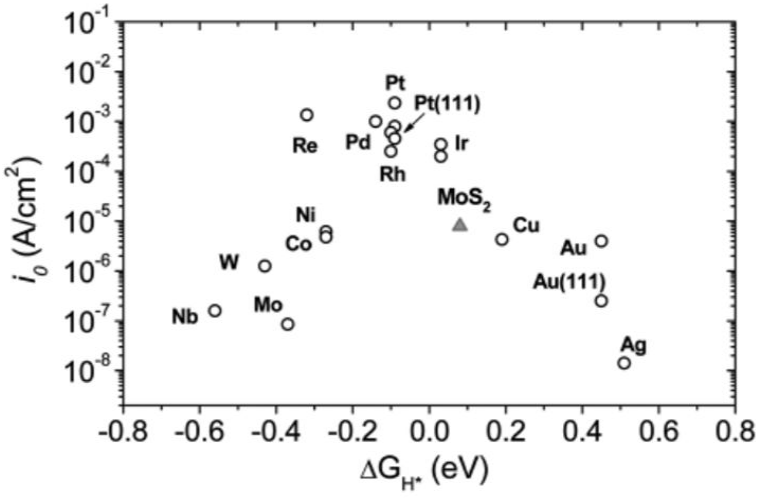

Figure 1.10: *Volcano plot of the exchange current density as a function of the DFT-calculated Gibbs free energy of adsorbed atomic hydrogen for nanoparticulate MoS_2 and the pure metals such as Pt and others*

According to this figure, platinum (Pt) has a Gibbs energy of chemisorbed H close to zero and the highest exchange current density among these materials, which makes Pt a highly efficient catalyst for HER. In fact, Pt is used as the benchmark catalyst for HER since no catalyst has shown better catalytic ability than this material to date. [36] In practical experiments at low overpotentials, Pt can achieve exchange current density (j_0) of about 1 mA/cm^2 and a Tafel slope of 30 mV/decade (see details about Tafel plots in Chapter. 3.2.4). [64] After optimazation, a j_0 of about 500 mA/cm^2 can be reached at higher overpotentials with a Tafel slope of 140 mV/dec, and a mass activity of about 1000 A/(mgPt). [65] However, the industrial performance can be orders of magnitude lower than lab performance where the best catalysts can only achieve about 10 A/(mgPt). [64, 66] Hence, to produce hydrogen on TW scale, using Pt as HER catalyst will not be feasible since the element is too rare and too expensive.

Therefore, worldwild research activities have been seek to develop cheap, Earth-abundant and environmentally friendly catalysts to replace Pt as HER catalyst. In the past years, many materials have shown the potential as alternative, and

Fig. 1.11 [4] shows the elements mostly used to synthesize HER catalysts, including transition metal elements such as Mo, W, Co, Fe and Ni, and non-metal elements like S, P, Se, C and N. Alloys and compounds combining these elements form the new HER catalyst materials that have been mostly studied so far. These include Ni alloys, [67,68], metal sulfides such as molybdenum, [69] cobalt, [70] and tungsten sulfide [71], metal phosphides using nickel, [72], cobalt, [73] and molybdenum. [74]

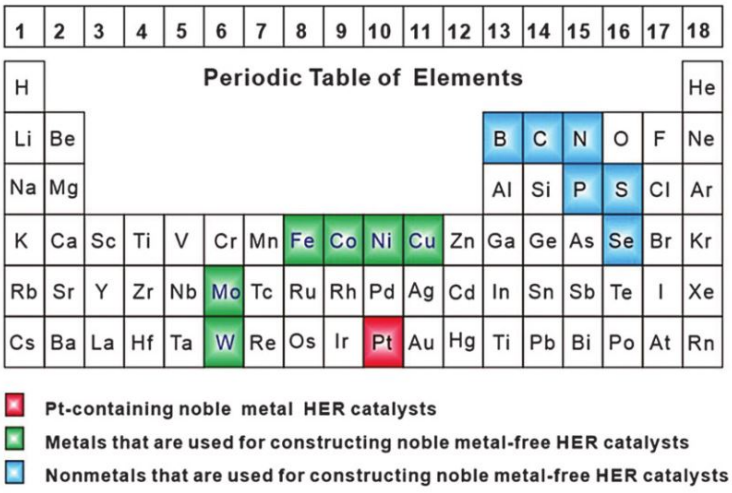

Figure 1.11: *Elements used for synthesizing HER catalysts [4]*

1.4 CO_2 reduction reaction (CO_2RR) using solar energy

1.4.1 Basic principles of CO_2RR

As mentioned above, hydrogen has great potential as an ideal energy carrier for the future. However, as shown in Table 1.1, hydrogen in the gas phase has much lower volumetric energy density than liquid fuels. In addition, hydrogen storage and transportation remain major challenges. [75] CO_2 reduction and conversion into fuels using electrochemical catalysis have also attracted great attention in recent years, since this process could yield more versatile carbon-based fuels and this CO_2RR process can be driven by renewable energy, e.g. solar energy. In addition, the conversion process is controllable by electrode potentials and reaction temperature. [29]

Table 1.2: *Selected half reactions of CO_2RR and the associated potentials under standard conditions (*1.0 atm *at* 25 °C*) [28, 29]*

Half reactions of CO_2RR	**Potentials (V vs. SHE) under standard conditions**
$CO_2(g) + 4H^+ + 4e^- \leftrightarrow C(s) + 2H_2O(l)$	0.210
$CO_2(g) + 2H_2O(l) + 4e^- \leftrightarrow C(s) + 4OH^-$	-0.627
$CO_2(g) + 2H^+ + 2e^- \leftrightarrow HCOOH(l)$	-0.250
$CO_2(g) + H_2O(l) + 2e^- \leftrightarrow HCOO^-(aq) + OH^-$	-1.078
$CO_2(g) + 2H^+ + 2e^- \leftrightarrow CO(g) + H_2O(l)$	-0.106
$CO_2(g) + H_2O(l) + 2e^- \leftrightarrow CO(g) + 2OH^-$	-0.934
$CO_2(g) + 4H^+ + 4e^- \leftrightarrow CH_2O(l) + H_2O(l)$	-0.070
$CO_2(g) + 3H_2O(l) + 4e^- \leftrightarrow CH_2O(l) + 4OH^-$	-0.898
$CO_2(g) + 6H^+ + 6e^- \leftrightarrow CH_3OH(l) + H_2O(l)$	0.016
$CO_2(g) + 5H_2O(l) + 6e^- \leftrightarrow CH_3OH(l) + 6OH^-$	-0.812
$CO_2(g) + 8H^+ + 8e^- \leftrightarrow CH_4(g) + 2H_2O(l)$	0.169
$CO_2(g) + 6H_2O(l) + 8e^- \leftrightarrow CH_4(l) + 8OH^-$	-0.659
$2CO_2(g) + 2H^+ + 2e^- \leftrightarrow H_2C_2O_4(aq)$	-0.500
$2CO_2(g) + 2e^- \leftrightarrow {C_2O_4}^{2-}(aq)$	-0.590
$2CO_2(g) + 12H^+ + 12e^- \leftrightarrow CH_2CH_2(g) + 4H_2O(l)$	0.064
$CO_2(g) + 8H_2O(l) + 12e^- \leftrightarrow CH_2CH_2(g) + 12OH^-$	-0.764
$2CO_2(g) + 12H^+ + 12e^- \leftrightarrow CH_3CH_2OH(l) + 3H_2O(l)$	0.084
$2CO_2(g) + 9H_2O(l) + 12e^- \leftrightarrow CH_3CH_2OH(l) + 12OH^-$	-0.744

The half reaction equations of CO_2RR are summarized in Table 1.2 together with their associated reaction potentials. The easiest products obtained from CO_2RR are carbon monoxide (CO) and formic acid/formate ($HCOOH/COOH^-$) since only two electrons have to be transferred. More complex processes are the formation of formaldehyde (HCHO), methane (CH_4), methanol (CH_3OH), ethanol (C_2H_5OH) and so on. In CO_2RR, the concentration of CO_2 that can be dissolved in aqueous electrolyte is low, compared to the concentration of protons or water that are reactants for HER. Since HER is also taking place under cathodic conditions and even enhanced by high overvoltages, the competition between HER and CO_2RR leads to low selectivity for CO_2RR. Moreover, the electrochemical reduction of CO_2 is a multi-electron transfer process including complex reaction pathways (see Table. 1.2). For example, up to 12 electrons need to be transferred to produce ethanol or ethylene, which makes the kinetics of CO_2RR complicated and relatively slow even with the presence of catalyst. [76] And normally, the products of CO_2RR are a mixture of different compounds rather than single species. This suggests that most catalysts don't show high selectivity towards a certain product. Up to now, the catalysts that have been studied are in general not active enough to overcome the kinetic barrier of those reactions. [29] Therefore, discovering CO_2RR catalysts with

both good activity and selectivity are of great importance.

1.4.2 Catalysts for CO_2RR

The key potential-dependent steps can be written by the equations below [77]:

$$CO_2 + H^+ + e^- \leftrightarrow COOH^* \tag{1.19}$$

$$COOH^* + H^+ + e^- \leftrightarrow CO^* + H_2O \tag{1.20}$$

$$CO^* + H^+ + e^- \leftrightarrow CHO^* \tag{1.21}$$

The asterisk * stands for an active site on the catalyst surface. DFT studies have shown that during CO_2RR, the activity of catalysts is limited by linear scaling relations between the binding energies of CO_2RR intermediates. [78] During CO_2RR, catalysts with a strong bond with COOH intermediate (E_b(COOH)) at a low negative range and a weaker bond with CO (E_b(CO) not far from zero) have the ability to reduce CO_2 to CO, while further reduction of CO is usually limited by the third step in which CHO is formed. Following this principle, to produce more complex hydrocarbons other than CO during CO_2RR, catalysts should be able to stabilize COOH and CHO intermediates ($COOH^*$, CHO^*) more than they do for CO. [79]

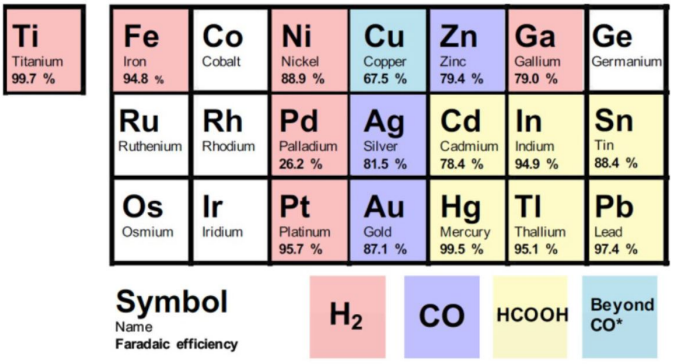

Figure 1.12: *Major products of various metal catalyst for electroreduction of CO_2 [11, 12]*

Until recently, the most studied catalysts for CO_2RR are metal catalysts. In 1954, Teeter first investigated the production of formic acid during CO_2RR on Mercury (Hg) electrodes. [80] Since then, numerous studies on the electrochemcial reduction of CO_2 on metal surfaces have been performed. For example, Hori et al. (1985) studied CO_2RR using catalysts such as Zn, Cd, Sn, Cu, and Pb. The products of

CO_2RR using these metal catalysts are later classified by Bagger et al. in 2017 as shown in Fig. 1.12. [12]. Here, the catalysts are divided into four categories based on their major products: H_2, CO, formic acid and beyond CO^*. For instance, Pt, Fe, and Ni mainly produce H_2 while Zn, Ag and Au favor CO production. Cd, In and Hg reduce CO_2 to primarily formic acid. The faradaic efficiencies of these catalysts are shown in the figure as well. Among all the listed catalysts, only Cu shows a pronounced catalytic ability for a further reduction of CO^*.

When using Cu as a catalyst for CO_2RR, the main products are formate, CO, and hydrocarbons such as methane and ethylene [81]. In 2014, Strasser et al. [13] discovered that the product preference of Cu catalysts is dependent on the size of the nanoparticles as shown in Fig. 1.13. When the nanoparticles have a size below 5 nm, the catalysts showed high H_2 and CO production. Larger particles in the 15-35 nm region showed increasing catalytic activity towards hydrocarbon (CH_4, C_2H_4) formation while the faradaic efficiencies of H_2 and CO production decrease with particle size.

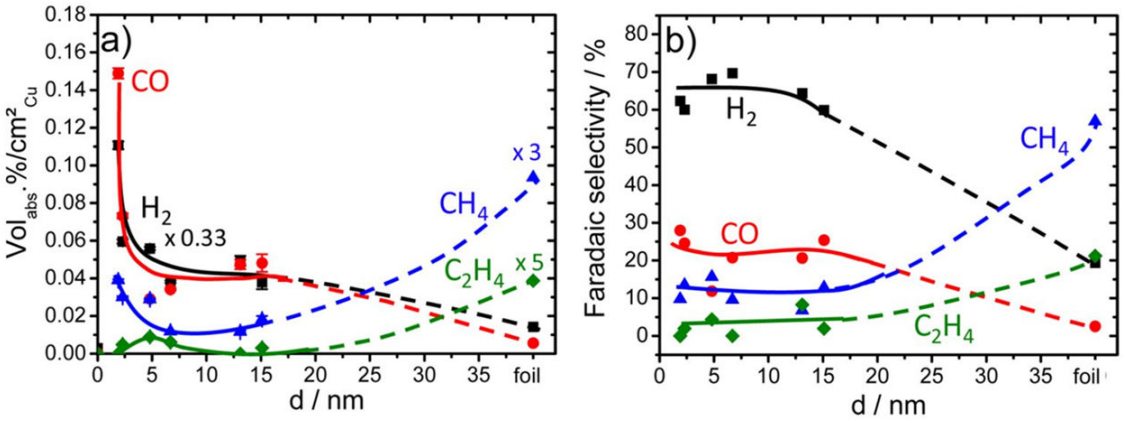

Figure 1.13: *Cu particle size dependence of CO_2RR products: (a) composition of the gaseous products; (b) faradaic efficiencies of the gaseous products [13]*

1.5 Molybdenum sulfide

Molybdenum sulfide has been used for different fields because of its layer structure, [82] for instance as a catalyst for hydrodesulfurization, [83] as a transistor material, [84] and also as a solid lubricant. [85] Molybdenum sulfide crystallize in

different structures, such as 2H-MoS_2, 3R-MoS_2 and 1T-MoS_2. All three phases have two dimensional (2D) layer structures in common as shown in Fig. 1.14. Among them, 2H and 3R are the two main phases and the 2H phase is the dominant and most stable phase in nature. As shown in Fig. 1.14, 2H-MoS_2 has two S-Mo-S slabs per unit cell showing a trigonal prismatic coordination of Mo by sulfur while 3R-MoS_2 has three S-Mo-S slabs per unit cell. [86] 1T-MoS_2 phase with octahedral coordination, one S-Mo-S slab per unit cell and metallic property [87] was discovered by Frindt et al. by exfoliation of lithium-intercalated MoS_2 powder in water. [88]

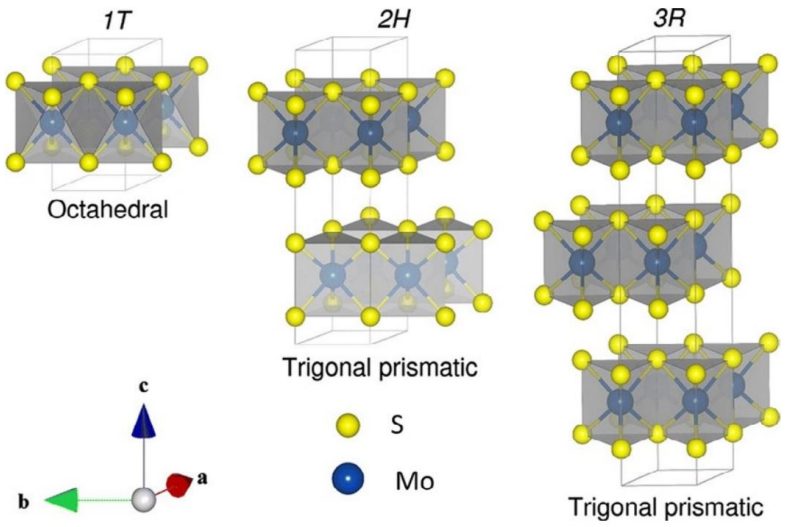

Figure 1.14: *Coordinations of MoS_2 in unit cells: octahedral (1T), trigonal prismatic (2H) and trigonal prismatic (3R) unit cell structures [14, 15]*

According to Late et al. [89], each 2D layer of MoS_2 crystal has a hexagonal plane of Mo atoms and two of S atoms, and each single layer with a lamellar S-Mo-S structure has a thickness of about 0.66 nm according to Kibsgaard et al. [17] Bulk MoS_2 has an indirect band gap of 1.29 eV. [90]. For ultra-thin MoS_2, monolayer of MoS_2 has a direct band gap while multi-layer MoS_2 has an indirect band up of 1.9 eV that shifts downwards with increasing layer number by more than 0.6 eV. [91]

1.5.1 MoS_2 as catalyst for HER

Among the non-precious metal catalysts that have been studied, molybdenum sulfide is well known for its high catalytic activity for hydrogen evolution and its high chemical stability, especially under acidic conditions. Interestingly as shown

in former studies, MoS_2 was thought to have a low catalytic activity for HER. [92] However, according to theoretical calculations, MoS_2 should be highly active as a HER catalyst since it has a modest binding energy with atomic hydrogen and a relatively high exchange current density, as first described by Jaramillo et al. [16] (see Fig. 1.15A). In the same paper, it is also shown that the exchange current density of the material is proportional to the edge length of the hexagonal particles rather than the surface area of MoS_2 (see Fig. 1.15), suggesting that the active sites of MoS_2 are located on the edges of the S-Mo-S slabs and the basal planes are catalytically inert. Therefore the reason for the low catalytic activity of bulk MoS_2 was found to be low density of active edge sites.

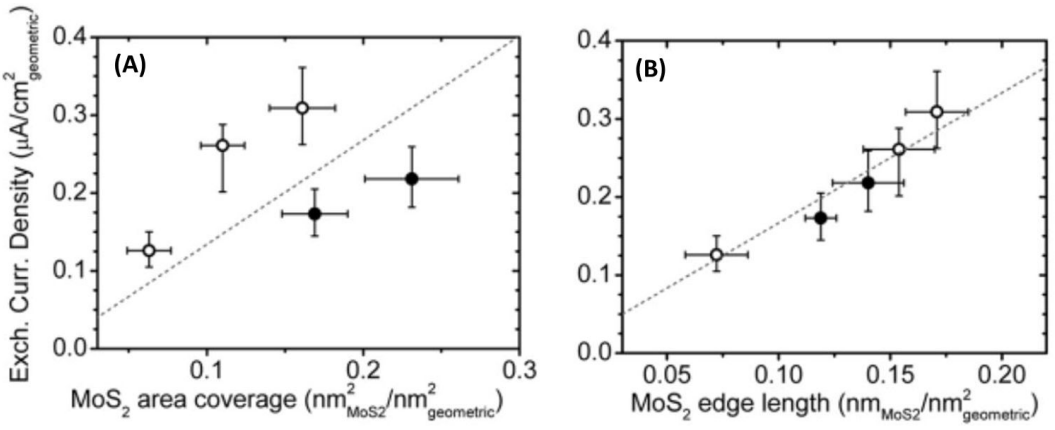

Figure 1.15: *Exchange current density of MoS_2 as the function of: (A) MoS_2 area coverage; (B) MoS_2 edge length [16]*

Since then, researchers have devoted much effort toward increasing the catalytic activity of MoS_2 as a HER catalyst.

One strategy to increase the catalytic activity is simply introducing more active sites at the surface. To achieve this goal, Kibsgaard et al. 2012 [17] engineered the surface structure of mesoporous MoS_2 thin films with a high degree of surface curvature to preferentially expose more edge sites than basal planes in the electrolyte, leading to an improved catalytic activity, as shown in Fig. 1.16A. Kiriya et al. [93] discoverd that by thermal texturization of MoS_2 using high temperature hydrogen annealing, an improvement of the catalytic activity of molybdenum sulfide using bulk, powder and nanoflake MoS_2 as precusors, can be achieved because of the increased surface area and the number of active edge sites. In 2016, Li et al. [18] increased the active site number by introducing sulfur vacancies and straining the lattice to activate the basal planes of MoS_2 particles as shown in Fig. 1.16B. DFT calculation suggested higher hydrogen adsorption and optimal ΔG_H in the strained MoS_2 with sulfur va-

cancies. Electrochemical measurement showed indeed lower overpotential of 170 mV at 10 mA/cm^2.

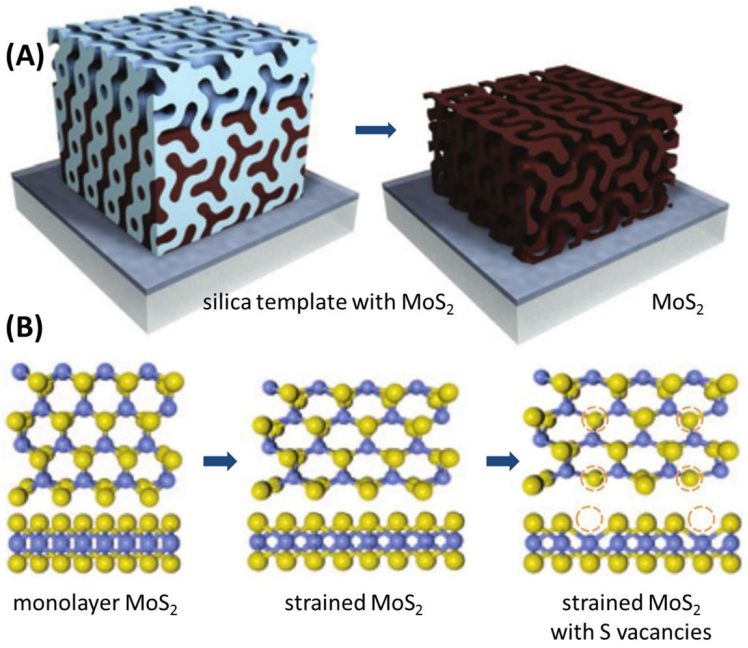

Figure 1.16: *(A) structural model for mesoporous MoS_2 with a double-gyroid (DG) morphology [17]; (B) activating MoS_2 by introducing strain and S vacancies [18]*

Other than modifying the structure of MoS_2 itself, molybdenum sulfides with different structures have also been studied.

As mentioned above, HER active sites of molybdenum sulfide are located on the edges. Therefore, cluster-type molybdenum sulfides characterized by a high number of edge sites could also lead to a better HER catalytic ability. For example, incomplete cubane-type $[Mo_3S_4]^{2-}$ cluster with structure shown in Fig. 1.17A were used for HER in 2008 by Jaramillo et al. [19] and a similar overpotential as nanoparticulate MoS_2 of about 300 mV at $-10\,mA/cm^2$ was obtained. Then in 2014, thiomolybdate $[Mo_3S_{13}]^{2-}$ cluster with a high ratio of edge sulfur atoms, which were thought to be catalytic active for HER, was discovered as an efficient HER catalyst showing relatively low overpotential (in the range from 180 mV to 220 mV at $-10\,mA/cm^2$) and high stability (10-20 mV overpotential increase at $-10\,mA/cm^2$) after 1000 cycles in the potenial range from 0.2 to -0.3 V with a scan rate of 100 mV/s). [20] The structure of $[Mo_3S_{13}]^{2-}$ cluster is shown in Fig. 1.17B. Three kinds of sulfur species are present in this cluster: terminal $[S_2]^{2-}$, bridging $[S_2]^{2-}$ and apical S^{2-} moieties.

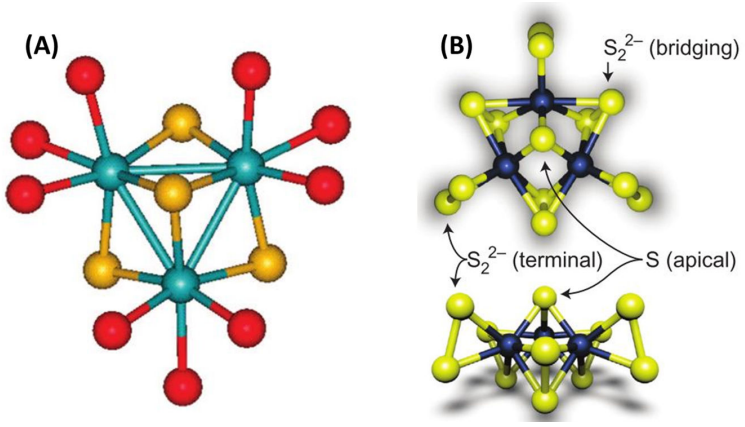

Figure 1.17: *Structural scheme of: (A)$[Mo_3S_4]^{2-}$ cluster; [19] (B) $[Mo_3S_{13}]^{2-}$ cluster [20]*

In addition, amorphous MoS_x was also discovered and described as HER catalyst for its excellent catalytic activity. Amorphous MoS_x has a local structure which is different from that of hexagonal MoS_2. Fig. 1.18 shows the structure of amorphous MoS_x proposed by Hu et al. [21] in 2014. Amorphous MoS_x can be synthesized through different methods, such as electrodeposition, [94] wet chemical reaction, [95] and sulfurization of molybdenum metal without thermal treatment. [96, 97] The origin of its high catalytic performance was not clear at this time. Possible reasons were thought to be the high surface area [98] and the existence of bridging and terminal $[S_2]^{2-}$ units [95]. In 2016, Yeo et al. [99] found that the composition of S species in amorphous MoS_x was changing during the HER process and in the meantime, Artero et al. [100] observed a loss of terminal $[S_2]^{2-}$ during HER, suggesting that MoS_x undergoes structural changes in HER catalysis process.

There are further methods to improve the catalytic ability of molybdenum sulfide. Recent publications have already shown that doping MoS_x with elements such as Co, Fe and Ni could improve its catalytic ability. [98] Another approach, a partial phase transformation, from the thermodynamically favored 2H-MoS_2 to metallic 1T polymorph by electrochemical process, could lead to more competitive HER activities. [101]

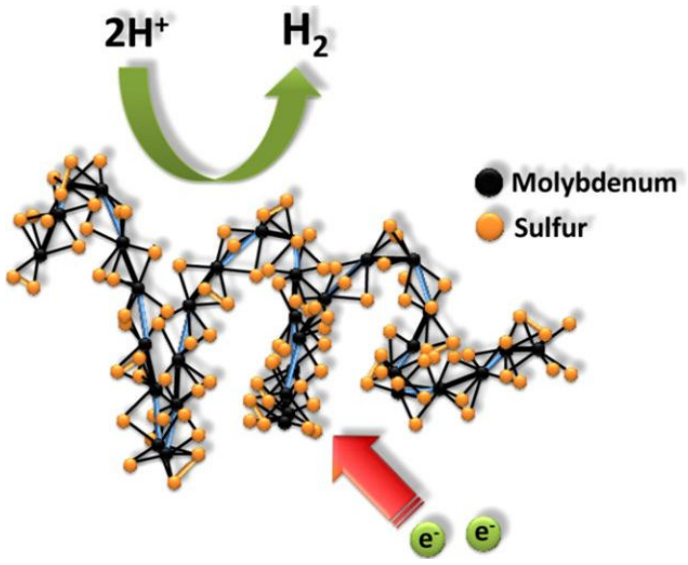

Figure 1.18: *Proposed structure of amorphous MoS_x [21]*

However, despite the progress has been achieved during the past years, the catalytic performance of MoS_2 as HER catalyst, in both activity and stability, is still inferior to that of Pt. In addition, the catalytic mechanism of MoS_2 as HER catalyst is not yet fully understood. For this reason, efforts are still needed to further improve its catalytic activity and to better understand the catalytic mechanism of molybdenum sulfide for hydrogen production.

1.5.2 MoS_2 as catalyst for CO_2RR

In 2014, Nørskov et al. [79] proposed that molybdenum sulfides and selenides as possible electro-catalyst candidates for CO_2RR based on theoretical DFT calculations. They predicted significant improvement in activity compared with transition metal catalysts. As a result of their calculations, the edge S atoms in MoS_2 are predicted to bind with CHO and COOH, while the Mo edges tend to bind with CO and S edge could be more selective than Mo edges for CO_2RR over H_2 evolution.
Unlike MoS_2 as catalyst for HER, only a few publications on MoS_2 report its behavior as a CO_2RR catalyst. Asadi et al. [102] firstly investigated bulk MoS_2 for CO_2RR in ionic liquid in 2014 and later in 2016, TMDC (transition metal dichalcogenide) nanoflakes including MoS_2, $MoSe_2$, WS_2, WSe_2 were tested as CO_2RR catalysts showing promising catalytic performance. [103] In 2018, Francis et al. [22] studied single crystal and thin films of MoS_2 as catalysts for CO_2RR. As shown in Fig. 1.19A, 1-propanol and formate were produced as major products for bulk MoS_2 catalyst.

Production of ethylene glycol ($C_2H_6O_2$), t-Butanol ($C_4H_{10}O$), and methanol were detected with low faradaic efficiency, while most of the current observed was attributed to hydrogen production. According to Li et al., [104], amorphous MoS_x can also be used for CO_2RR, producing CO with a maximum faradaic efficiency of 85.1%.

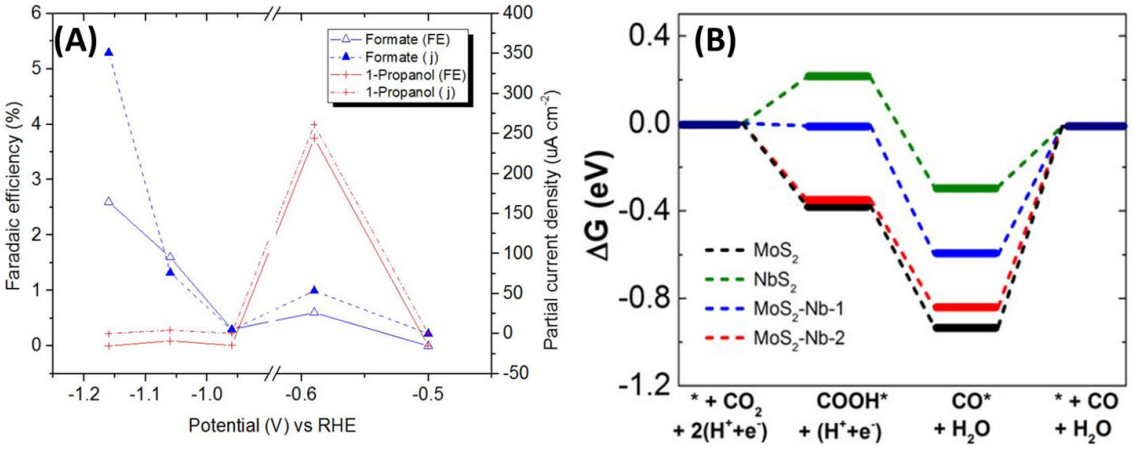

Figure 1.19: *(A) Faradaic efficiencies of 1-propanol and formate in CO_2RR using a MoS_2 single crystal catalyst; [22] (B) ΔG in CO production pathways for different MoS_2 catalyst [23]*

However, following DFT calculation by Abbasi et al. [23], pure MoS_2 has too strong binding energy to CO, which should inhibit the desorption of CO and thus decrease the turnover frequency (TOF). Fig. 1.19B shows the ΔG values in the reaction pathways for CO production for different MoS_2 catalysts. By doping Nb, the binding strength between Mo edge and CO could be decreased, leading to an improvement in the catalytic ability. Over 80% faradaic efficiency for CO production could be reached at $-0.8\,\mathrm{V}$ vs. RHE.

1.6 This thesis

As mentioned above, molybdenum sulfide has been studied as a catalyst for both HER and CO_2RR and it already shows promising results. However, the catalytic mechanism of this material is still partially unclear, and the performance as hydrogen evolving catalyst is still inferior compared to well-known catalyst such as Pt. Therefore in our study, molybdenum sulfide was chosen as the main subject of investigation. We aimed to further improve its catalytic ablility by investigating its behavior during the catalysis process.

In Chapter 2, the preparation methods and the characterization techniques used

during the study of molybdenum sulfide as catalyst for HER and CO_2RR are described in detail.

In Chapter 3, ammonium thiomolybdate ($(NH_4)_2Mo_3S_{13}$) as a HER electro-catalyst was studied first. An overpotential of 0.22 V at $-10\,mA/cm^2$ was achieved by the spin-coated $(NH_4)_2Mo_3S_{13}$ thin film. The identification of the active sites in this cluster material was performed through DFT calculations. In addition, the $(NH_4)_2Mo_3S_{13}$ cluster was studied as a semiconducting co-catalyst for WSe_2 photocathode for the first time. The catalyst is able to form a hetero-junction with WSe_2, and passivate the surface states of the textured WSe_2 layer at the thiomolybdate-WSe_2 interface. A significant improvement of the photocurrent in 0.5 M sulfuric acid electrolyte could be achieved after the deposition of a thin $(NH_4)_2Mo_3S_{13}$ film on WSe_2. The semiconducting properties and the thermal stability of $(NH_4)_2Mo_3S_{13}$ are also described in this chapter.

In Chapter 4, molybdenum sulfide films prepared by reactive magnetron sputtering with different degrees of crystallinity were studied as HER catalyst. An activation process during the first three to four electrochemical cycles accompanied by massive release of H_2S has been observed for room temperature (RT) sputtered amorphous MoS_x. Optimal catalytic activity was achieved by the activated amorphous MoS_x with overpotential of 180 mV at $-10\,mA/cm^2$. The catalytic ability of the sputtered MoS_x films decreases with increasing sputtering temperature. For amorphous MoS_x electrode, a phase transformation from polymerized Mo_3S_{13} and Mo_3S_{12} ligands to MoS_{2-x} layer structure during electrochemical cycling could be identified through *in-situ*/in-line Raman measurements.

The catalytic ability of sputtered molybdenum sulfide for CO_2RR is investigated in Chapter 5. The molybdenum sulfide films are prepared by reactive magnetron sputtering at different temperatures on gas diffusion electrode (GDE) substrates. Combining electrochemical measurements with mass spectrometry, headspace gas chromatography, and high performance liquid chromatography, the products of CO_2RR can be detected and studied. Although high current could be obtained from the sputtered molybdenum sulfide electrodes, the current is mainly attributed to HER, and the detected products from CO_2RR, such as formaldehyde, methanol and ethanol, are only found in small quantities.

Chapter 2

Experimental

2.1 Sample preparation

2.1.1 Synthesis of ammonium thiomolybdate ($(NH_4)_2Mo_3S_{13}$)

$(NH_4)_2Mo_3S_{13}$ was synthesized according to the method described by Müller et al. in 1978. [105] Firstly, $(NH_4)_6Mo_7O_{24} \bullet 4H_2O$ (4 g) was dissolved in 20 mL deionized water in a round flask (250 mL). A solution of ammonium polysulfide (120 mL, 8%, Fisher Scientific) was then added into the same flask and heated under reflux at 90 °C overnight. Then, a dark red precipitate of $(NH_4)_2Mo_3S_{13}$ was formed. After filtering and washing with ethanol and water, the product was annealed at 80 °C in toluene (50 mL) for about 2 h. A dark red thiomolybdate powder, as shown in Fig. 2.1 was obtained after filtering and drying.

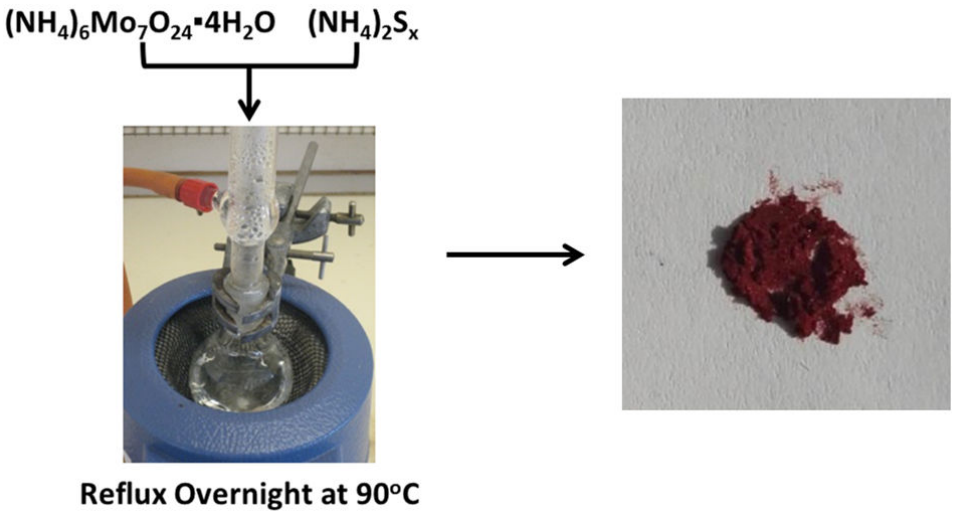

Figure 2.1: *Synthesis of $(NH_4)_2Mo_3S_{13}$*

To deposit thin films of $(NH_4)_2Mo_3S_{13}$, the synthesized powder was dissolved in dimethyl sulfoxide (DMSO) or methanol and deposited by spin-coating or drop-casting on fluorine-doped tin oxide (FTO) glass substrates or WSe_2 electrode. Afterwards, the samples were dried in vacuum for 30 min and later annealed at 100 °C for 2 h to evaporate the solvent.

2.1.2 Molybdenum sulfide prepared by reactive magnetron sputtering

Magnetron sputtering is a plasma deposition technique invented by Penning in the 1930s. [106] It is an efficient deposition method to prepare films of metallic, semiconducting and isolating materials with high deposition rate, high film homogeneity, low film contamination and extremely high film adhesion. [107] Therefore, magnetron sputtering was chosen as the technique to prepare catalyst films in our study.

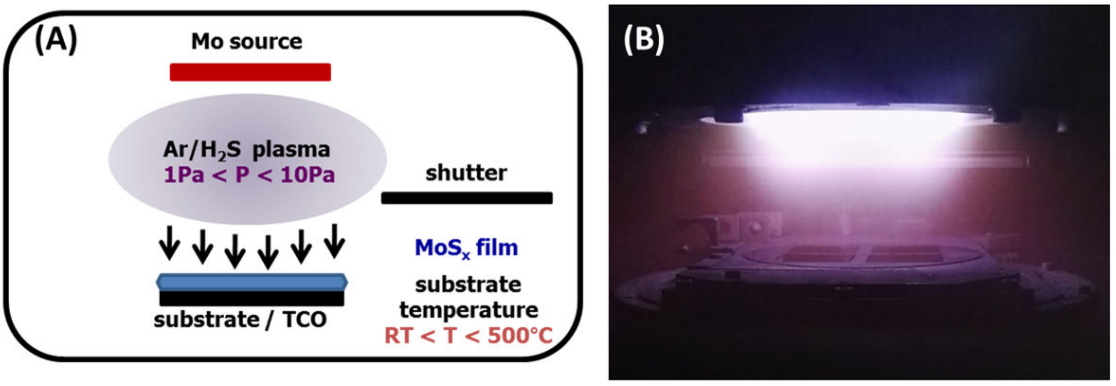

Figure 2.2: *(A) Scheme of the sputtering chamber; (B) Optical photograph of our sputtering chamber during the sputtering process*

A side view of the sputtering chamber is shown in Fig. 2.2 by a schematic drawing including a photo of the chamber under operation. In the sputtering chamber, a molybdenum target was mounted on a magnet. Argon (Ar) was added as working gas to eject atoms from the surface of Mo target (99.99%, Freiberger NE-Metall GmbH) while hydrogen sulfide (H_2S) was used as reactive gas. The ratio between H_2S and Ar was kept as 3:1, and the flow rates for H_2S and Ar are adjusted to 5.1 sccm and 1.7 sccm respectively. The total pressure (P) in the chamber under operation condition is about 1.3 Pa.
During sputtering process, a negative potential is applied on the sputtering target.

Electrons emitted from the cathode are accelerated towards the substrates by the electric field. During this period, the accelerated electrons are able to ionize Ar atoms in the chamber to produce new electrons and Ar^+. Then the Ar^+ ions move in the opposite direction to the cathode and hit the target producing neutral Mo atoms and secondary electrons. Due to the presence of a magnetic field produced by the magnet behind the target, the electrons are trapped in a region close to the cathode causing more ionization which can improve the sputtering process while the neutral sputtered Mo atoms deposit on the surface of the substrate. A value of 100 W DC power was kept constant during the whole sputtering process. A heater beneath the substrate holder allows us to control substrate temperature during sputtering from room temperature (RT) up to 500 °C. To acquire films of high purity, the shutter between the target and substrate was kept closed in the first 5 min of the sputtering process to get rid of contamination on the surface of the target, which is the so-called pre-sputtering process.
Molybdenum sulfide catalysts for HER were prepared on fluorine doped tin oxide (FTO) substrates with the size of 2.2 cm * 2.2 cm. All the substrates were cleaned in acetone, ethanol, and deionized water for 20 min in an ultrasonic bath and blow dried in N_2 gas flow before sputtering.
Catalysts for CO_2RR were deposited on gas diffusion electrodes (GDE) with gas diffusion layer (GDL) as provided by SIGRACET (GDL 31BC) with hydrophobic treatment. GDE substrates usually contains a macro-porous backing material (carbon fiber paper) and a micro-porous carbon based layer (MPL). [108] And it is widely used in proton exchange membrane fuel cells (PEMFCs) since they regulate all relevant transport processes (fuel, reation products, electricity and heat). [109, 110]

2.2 Characterization methods

2.2.1 Electrochemcial and photoelectrochemical measurements

The catalytic ability of the HER catalysts was studied electrochemically using different methods, including cyclic voltammetry (CV), stability measurement, differential electrochemical mass spectroscopy (DEMS) and intensity modulated photocurrent spectroscopy (IMPS).
A three-electrode configuration was used with Pt as counter electrode (CE) and Ag/AgCl electrode in saturated KCl aqueous solution (−0.197 V vs. reversible hy-

drogen electrode (RHE)) as reference electrode (RE). The structure of the cell used for both electrochemical and PEC measurements is shown in Fig. 2.3. To exclude the possiblity of Pt getting oxidized and dissolved in electrolyte, [111] a glassy carbon electrode was also used as CE for comparison in CV and DEMS measurements.

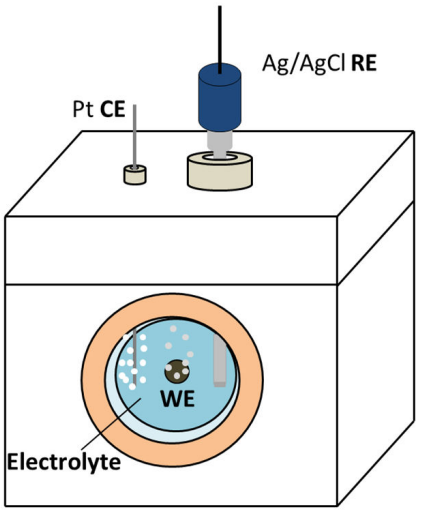

Figure 2.3: *Scheme of (photo)electrochemical cell*

CV, stability measurement, iR drop and capacitance measurement were performed using a VersaSTAT potentiostat (Princeton Applied Research). The iR drop in the electrolyte was calculated by measuring the resistance of the sample in the electrolyte at 100 kHz using electrochemical impedance spectroscopy (EIS) with a modulation frequency of 10 mV. The current density was evaluated from CV measurements performed within the potential range from 0.2 V to −0.3 V vs. RHE with a scan rate of 10 mV/s. The capacitance measurements were performed using CV by sweeping the potential in the range from 0.1 V to 0.31 V vs. RHE using different scan rates (from 10 mV/s to 160 mV/s). Photoelectrochemical (PEC) measurements were performed with a EG&G PAR 273A potentiostat under AM1.5 illumination provided by a solar simulator from WACOM (type WXS-50S-5H, class AAA). All electrochemical measurements concerning molybdenum sulfide catalysts for HER were measured in 0.5 M H_2SO_4 (sulfuric acid) aqueous electrolyte (pH=0.3) and the contacting area of the sample with the electrolyte was fixed to 0.238 cm^2 using a 0.55 cm diameter O-ring to isolate the electrolyte from the rest part of the electrode and the back contact.

For CO_2RR measurements, a different cell was used since CO_2 is simultaneously purged from the back side of GDE substrate during electrochemical measurements.

The reason of using GDE substrates is the low solubility of CO_2 in aqueous electrolytes. In a common setup for CO_2RR, CO_2 is continuously purged to the electrolyte, but the diffusion of CO_2 in the electrolyte to the surface of WE is slow, which is a limiting factor for the reaction. In our setup, GDE allows the direct purging of CO_2 from the back side of WE, leading to an continuous saturation of CO_2 in the electrolyte near the electrolyte/catalyst interface.
The structure of the cell used for CO_2RR is shown in Fig. 2.4. During the reaction, the WE with GDE substrate was positioned in the middle of the bottom plate in the cell and connected to the potentiostat via a glassy carbon contact beneath WE. The CE was fixed in the left hole on the upper part while the RE was positioned on the right side. The three holes in the cell are connected and filled with CO_2 saturated aqueous electrolyte containing 0.5 M K_2SO_4 and 0.5 M $KHCO_3$. Under operating conditions, CO_2 is purged through the gas inlet beneath the WE which then diffuse into the electrolyte through GDE with a purging speed of 250 mL/h. The gaseous products, produced at the surface of WE can diffuse through GDE and flow out to the gas outlet and then can be measured by a mass spectrometer. Since the mass spectrometry is not a quantitative measurement, calibration is always needed to quantify the gaseous products. And the electrolyte used for CO_2RR was later collected and analyzed by headspace gas chromatography (HS-GC) and high performance liquid chromatography (HPLC) to investigate the liquid products of CO_2RR.

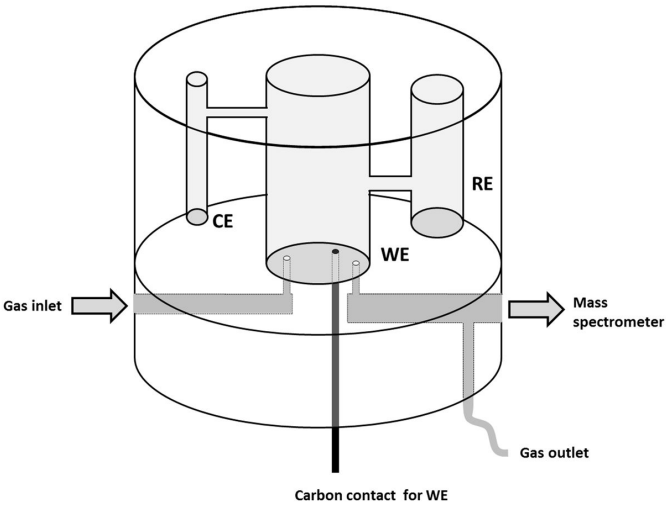

Figure 2.4: *Scheme of electrochemical cell for CO_2 reduction*

The electrochemical measurements in CO_2RR normally consists of two parts. Firstly, the line scan voltammetry (LSV) from 0 V to −2.3 V vs. SHE was applied to evaluate

the onset potential and different gaseous products. Secondly, fixed potentials were applied to the electrode for a certain time and the signals of the gaseous products and the electrolyte were both measured for the calculation of faradaic efficiency.
In the following section, two important electrochemical techniques used in this work will be introduced in detail.

Differential electrochemical mass spectroscopy (DEMS)

Differential electrochemical mass spectroscopy (DEMS) was employed to measure gases released during electrochemical measurements for HER. The DEMS system consists of a three-electrode electrochemical cell and a differentially pumped vacuum system attached to a mass spectrometer (QMG 220 M1, PrismaPlus 1-100 amu). The scheme of the DEMS cells is shown in Fig. 2.5. A membrane with a mechanical support is located in between the electrolyte and the puming system. The electrolyte between the working electrolde (WE) and the membrane has a thickness of about 200 µm. Using this geometry, the gases produced at the working electrode can diffuse through the electrolyte and the membrane, then be sucked into the vacuum chamber to be analyzed by the mass spectrometer. Further details can be found in an earlier publication from Bogdanoff et al. [112] In DEMS measurements, CV is performed in the potential range from 0.2 V to −0.3 V vs. RHE with a scan rate of 1 - 2 mV/s.

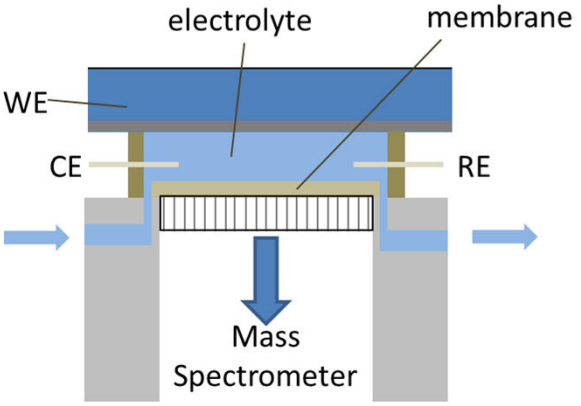

Figure 2.5: *Scheme of the DEMS cell*

Intensity modulated photocurrent spectroscopy (IMPS)

In order to investigate the role of $(NH_4)_2Mo_3S_{13}$ as a co-catalyst deposited on semiconductor surface, we used Intensity Modulated Photocurrent Spectroscopy (IMPS) to study charge transfer and surface recombination at the semiconductor/electrolyte interface and semicondutor/co-catalyst/electrolyte interface. This technique was first described by L. Peter et al. in 1984. [113] Since then, IMPS has been used as a powerful tool to study the interaction of a semiconductor with co-catalysts. [114–116] In principle, the photocurrent generated by a photoelectrode can be expressed as:

$$J = \varphi \cdot q \cdot \eta_{\mathrm{LH}} \cdot \eta_{\mathrm{CS}} \cdot \eta_{\mathrm{CT}} \tag{2.1}$$

In this equation, φ stands for the illumination intensity, q is the charge, η_{LH} is the light harvesting efficiency which is determined by the band gap and the absorption coefficient of the semiconductor, η_{CS} is the charge separation efficiency, which represents the fraction of photogenerated minority carries that reach the surface, and η_{CT} is the charge transfer efficiency which means the fraction of the minority carriers that get transferred from the semiconductor into the electrolyte.
During PEC process, the function of a co-catalyst is to increase the charge transfer by catalysis, suppressing the surface recombination through passivation, and/or by modifying the band bending. These functions normally have impact on the η_{CT} and/or η_{CS}. And it is possible to study the role of a co-catalyst by IMPS, since the recombination and charge transfer process in the photoelectrode can be investigated using this technique.

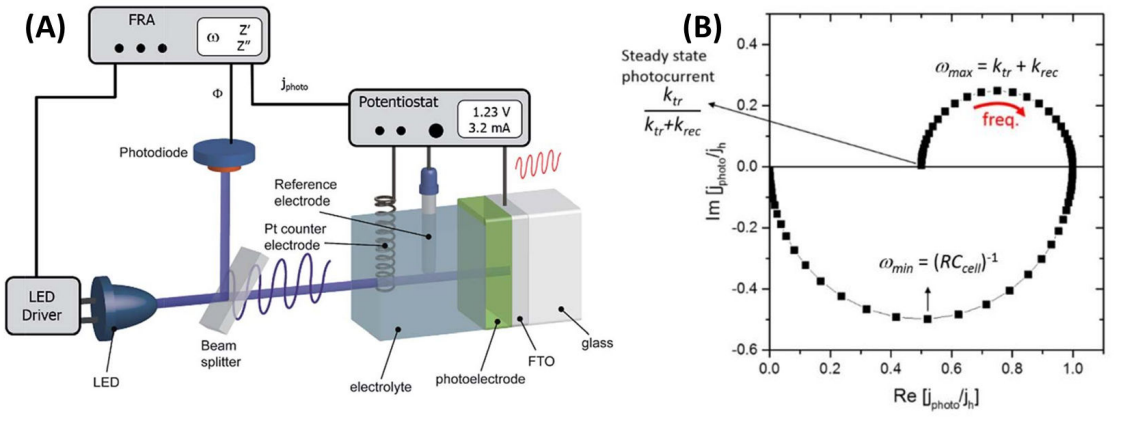

Figure 2.6: *(A) Scheme of IMPS setup; (B) Illustration of IMPS spectrum where $BiVO_4$ is used as a photoanode for PEC water splitting [24]*

Fig. 2.6A shows the scheme of the IMPS equipment used in our study. In this system, the illumination was provided by a light emitting diode (Thorlabs M455L3). The light source had the intensity of 4 mW/cm^2 with a wavelength (λ) of 455 nm and a 10% modulated amplitude. A beam splitter was used to split the light into two parts: one goes to a high speed Si photodiode (Thorlabs PDA10A-EC) and the other one goes to the PEC cell. A frequency response analyzer (FRA, Solartron 1250, Schlumberger) was used to modulate light intensity sinusoidally. During electrochemical measurements, a potentiostat (EG&G PAR 283) was used to apply potential to the photoelectrode. Then, the photocurrent (I_{photo}) measured by the potentiostat was recorded by channel 1 of FRA while the voltage signal of the high speed Si photodiode was recorded by channel 2 of the FRA. The opto-electrical gain was derived by dividing the signals from channel 1 and channel 2.

During IMPS measurement, the obtained photocurrent at fixed potential is also modulated due to the modulated illumination. The fluctuated photocurrent consists of the minority carrier current and the majority carrier current which precedes the minority carrier current. In a p-type semiconductor, electrons are the minority carriers and holes are the majority carriers while in a n-type semiconductor, holes are the minority carriers and electrons are the majority carriers. Therefore, the in-phase part and out-of-phase part lead to an overall photocurrent with real and imaginary components. Then the imaginary photocurrent can be plotted as the function of the real photocurrent as shown by a typical IMPS spectrum in Fig. 2.6B demonstrated by Zächaus et al. [24] In this example, there are two semicircles. The semicircle at negative imaginary photocurrent region is measured in a higher frequency range where the recombination is less evident because of fast modulation. The upper semicircle measured in a lower frequency range is more dominated by surface recombination. And the larger intercept of the higher frequency semicircle with the x-axis is normalized to 1 for easier comparison with the IMPS spectra measured at different potentials. The original value of this intercept stands for the minority current (j_h) given that the space charge capacitance (C_{sc}) is far less than the Helmholtz double layer capacitance (C_H). Besides, when the modulation frequency matches the characteristic relaxation constant of the system, the imaginary current reaches a maximum which can be expressed as:

$$\omega_{max} = k_{tr} + k_{rec} \tag{2.2}$$

ω in this equation is the angular velocity while k_{tr} is pseudo-first order charge transfer rate and k_{rec} represent the rate for surface recombination.

Besides, as shown in Fig. 2.6B, the smaller intercept of the upper semicircle equals to the charge transfer efficiency:

$$Re(Im = 0) = \eta_{\mathrm{CT}} = \frac{k_{\mathrm{tr}}}{k_{\mathrm{tr}} + k_{\mathrm{rec}}} \tag{2.3}$$

From these two equations, the charge transfer rate and the surface recombination rate can be calculated using the IMPS results. In this approach, by comparing the values of k_{tr} and k_{rec} of the sample with and without catalyst, the role of the catalyst can be determined.

2.2.2 Structural characterization

The morphology of the films was measured by Field Emission Scanning Electron Microscopy (FESEM) using a LEO GEMINI 1530 instrument from ZEISS, operated with an acceleration voltage ranging from 5 kV to 10 kV.
High Resolution Transmission Electron Micrographs (HRTEM) of amorphous MoS_x electrodes were measured using Philips CM12/ STEM with LaB_6 cathode as electron source, the acceleration voltage of which was 120 kV. To perform cross section analysis of the samples by TEM, the electrodes were cut into two halves and glued face-to-face prior to cut them with a diamond wire saw into small bars of 0.5 mm thickness. Afterwards, the samples were polished down to a thickness of 4-6 µm. Finally, they were ion milled (Baltec-RES 100) to prepare a grove where the thin edges could be analyzed by TEM.
Some of the important structural characterization methods are explained in detail in the following sections.

UV-vis spectroscopy

Ultraviolet-visible (UV/vis) spectroscopy was performed to study the optical properties of $(NH_4)_2Mo_3S_{13}$ films deposited on FTO substrates. A PerkinElmer Lambda 950 spectrophotometer was used for the UV/vis measurement with integrating sphere where the transflectance (TR) including transmittance (T) and reflectance (R), is measured directly. From UV/vis measurements, the absorption coefficient(α) of the sample can be calculated from the thickness (t) of the film and the transflectance (TR) using the equation:

$$\alpha = -ln(TR)/t \tag{2.4}$$

Then the band gap of the material can also be determined from the absorption coefficient (α) using *Tauc* plots derived from the following equation:

$$\alpha h\nu \propto (h\nu - E_{\mathrm{g}})^{1/\mathrm{n}} \tag{2.5}$$

In this equation, E_g is the band gap while ν is the light frequency, h is the Planck's constant and n can take values of 3, 2, 3/2, or 1/2, correspnding to indirect (forbidden), indirect (allowed), direct (forbidden), and direct (allowed) transitions. [117–120]

X-ray diffraction (XRD)

X-ray diffraction (XRD) is used to study the crystal structure of the prepared samples. A Bruker AXS D8 Advance X-ray diffractometer with Cu Kα radiation (λ=0.154 06 nm) was used to obtain X-ray diffractograms. Two measurement geometries used for XRD are shown in Fig. 2.7. The θ/2θ geometry was used for powder analysis while grazing incidence geometry shown in Fig. 2.7 is used for thin film analysis. In the θ/2θ geometry, the angle between diffracted X-ray and the sample stage was kept the same as the angle between incident X-ray and the sample stage. And in grazing incident geometry shown in Fig. 2.7, the angle between incident X-ray and the stage was fixed at a small angle (0.5 °) to increase the surface sensitivity.

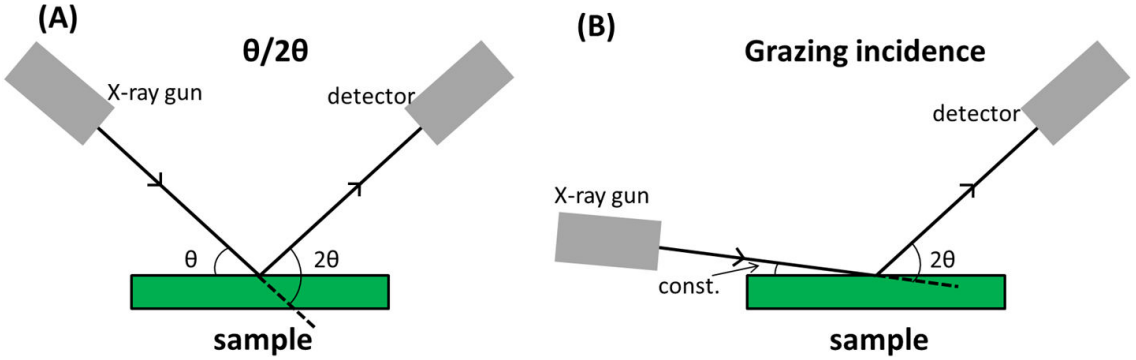

Figure 2.7: *Scheme of XRD measurement geometry: (A)θ/2θ geometry(B) grazing incidence geometry*

Raman spectroscopy

Raman spectroscopy is a powerful technique to study the structures and vibrations of molybdenum sulfide catalysts. It is a structural characterization method based on

Raman scattering effects. Fig. 2.8 shows the schematic diagram of different kinds of light scattering. The virtual states in the figure are formed by the cloud of distorted electrons, interacting with the scattered light. Fig. 2.8a is Rayleigh scattering where the scattered light has the same energy as the incident light. Fig. 2.8b and c show the Raman scattering. In Fig. 2.8b, the anti-Stokes scattering implies that the scattered light has higher energy than the incident light while in Stokes scattering as shown in Fig. 2.8c, the scattered light has lower energy than the incident light. Normally in Raman measurements, anti-Stokes scattering is filtered and only Stokes Raman scattering is recorded.

Besides, in Raman spectra, the y-axis shows the Raman intensity and the x-axis shows the Raman shift (cm^{-1}), demonstrating the information about the scattered light. The calculation of the Raman shift is given in Eq. 2.6:

$$Ramanshift = \frac{1}{\lambda_{\text{incident}}} - \frac{1}{\lambda_{\text{scattered}}} \tag{2.6}$$

In this equation, $\lambda_{\text{incident}}$ represents the wavelength of the incident light and $\lambda_{\text{scattered}}$ is the wavelength of the scattered light.

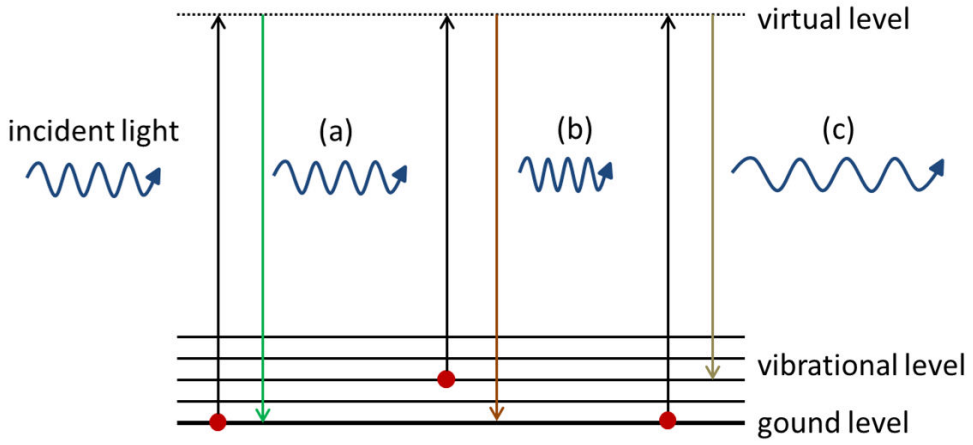

Figure 2.8: *Scheme of light scattering: (a) Rayleigh scattering; (b) Anti-Stokes Raman scattering; (c) Stokes Raman scattering*

In our work, an XploRA equipment from Horiba (λ = 532 nm, light intensity 0.112 mW) was used for normal Raman measurement. But to investigate the structural change of molybdenum sulfide catalyst during electrochemical measurement, an *in-situ*/in-line Raman system (DILOR LabRAM micro Raman system (λ = 632.8 nm, light intensity 4.3 mW/mm^2 (D2) or 47.1 mW/mm^2 (D1)) was used. The structure of the *in-situ* cell is shown in Fig. 2.9. In this scheme, QW stands for a quartz window. During *in-situ*/in-line Raman measurement, Raman laser illumi-

nates through the QW and a thin layer of electrolyte and then focuses on the surface of WE.

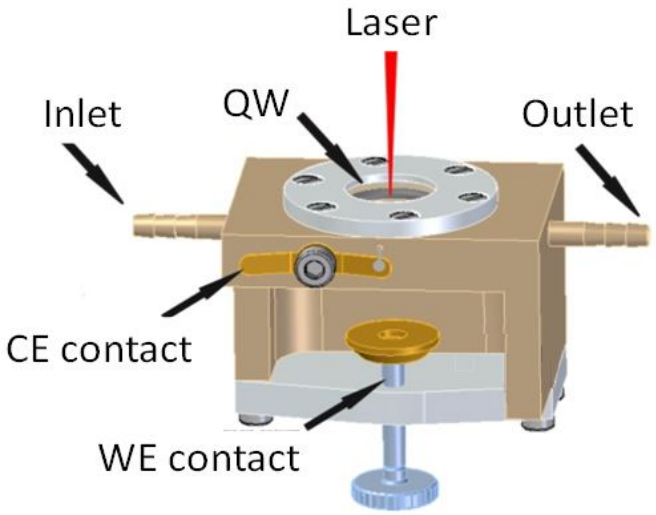

Figure 2.9: *Scheme of electrochemical cell for in-situ/in-line Raman*

X-ray photoelectron spectroscopy

To elucidate the chemical compositions and valence states of the elements in the catalyst and to study the change in the material during the catalytic process, X-ray photoelectron spectroscopy (XPS, the analyzer from SPECS, PHOIBOS 100) with a monochromatic X-ray source (SPECS FOCUS 500 monochromator, Al Kα radiation, 1486.74 eV) was used to investigate both sputtered molybdenum sulfide films and $(NH_4)_2Mo_3S_{13}$ layers. During the measurements, X-ray photons normally excite the core electrons of the atoms in a depth of 0-10 nm from the sample surface. The kinetic energy ($E_{kinetic}$) and the number of the escaped electrons are measured. From the kinetic energy, the binding energy of the electrons ($E_{binding}$) in the material can be calculated by:

$$E_{\text{binding}} = E_{\text{ph}} - E_{\text{kinetic}} - \chi \tag{2.7}$$

Here, E_{ph} stands for the incident light energy which is 1486.74 eV as mentioned and χ stands for the work function of the spectrometer which is 4.343 eV. The data obtained from XPS measurements are later calibrated using the carbon peak at 284.8 eV.

Kelvin probe microscopy/ Ambient pressure photoemission spectroscopy

Kelvin probe microscopy and ambient pressure photoemission spectroscopy (KP Technology Ltd.) is used to study the work function and the valence band maximum (VBM) of $(NH_4)_2Mo_3S_{13}$ cluster compound, respectively.
The work function measurement process is shown in Fig. 2.10. Fig. 2.10A shows the energy level diagram for two isolated metals with different work functions. When connecting two metals by a wire as shown in Fig. 2.10B, the Fermi levels of the metals equalize, causing electrons to flow from the metal with smaller work function to the one with higher work function. Therefore, an electric potential difference is created between two metals, known as contact potential (V_c in Fig. 2.10B). In equilibrium, this created potential is equal to the work function difference. Then a backing potential (V_b) is applied until the vacuum level is flat again. V_b at this point equals to -V_c. In practical experiments, the Kelvin probe with known work function, normally made of gold (Au) acts as one of the metals shown in Fig. 2.10. Oscillation of the Kelvin probe generates an AC current which is measured by an electrometer. Therefore, V_c can be found by gradually ramping of V_b until the AC current goes to zero. [121]

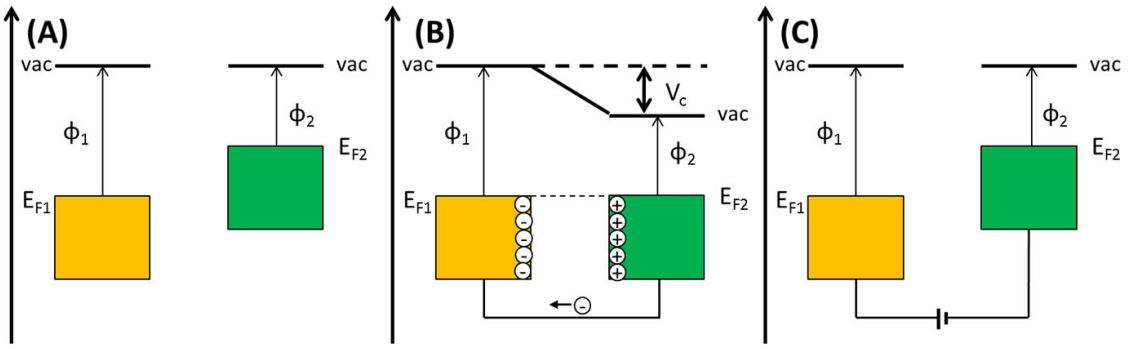

Figure 2.10: *Scheme of work function measurement process using Kelvin Probe*

For VBM identification, ambient pressure photoemission spectroscopy (AES) was used. A UV light source provided by a deuterium lamp with motorised monochromator has the energy range from 3.4 eV to 6.9 eV, corresponding to a wavelength range from 340 nm to 180 nm. During the measurement, the sample under UV illumination emits electrons from the surface which can be detected by the Kelvin probe position at about 1 mm from the sample. According to Fowler et al. [122], when plotting the square root of the photoemission current for metal samples (or cube root for most semiconductors) as a function of incident photon energy, the intercept of the straight region of the plotted curve equals to the VBM of the sample.

Thermogravimetric analysis/ mass spectrometry (TGA/MS)

To study the thermal stability of ammonium thiomolybdate (ATM), about 50 mg of the $(NH_4)_2Mo_3S_{13}$ powder was filled into an Al_2O_3 crucible, which was placed on a stem of a carrier system connected to the balance and heated in a furnace belonging to a simultaneous thermal analyzing system from Netzsch Company (STA 409 C). The sample was heated under Ar gas flow (80 ml/min) with a heating rate of 10 °C/min from room temperature (RT) up to 1000 °C. The products evolved during heating of $(NH_4)_2Mo_3S_{13}$ were transported by the Ar gas and in part extracted by passing through a 10 µm hole of an integrated ceiling located at the upper part of the furnace tube. It was then pumped via a skimmer hole in the formation chamber of a quadrupole mass spectrometer where the products were ionized before mass spectrometric analysis.

Headspace gas chromatography (HS-GC)

Headspace gas chromatography (Trace 1310, Thermo Scientific) equipped with a flame ionization detector (FID) and a pulsed discharge detector (PDD) was employed in our study, to detect and quantify the volatile products of CO_2RR in liquid phase such as methanol, ethanol, formaldehyde, etc. During HS-GC measurement, 5 mL electrolyte, saturated with potassium chloride (KCl) was stored in a sealed vial (Thermo Scientific, 20 mL HEADSPACE SCREW TOP vial) with a screw cap (Thermo Scientific X125 18 mm TOP) as shown in Fig. 2.11. During the incubation period, the vials were kept at 80 °C for 10 min due to which molecules of volatile components in the liquid sample can migrate to headspace. Then part of the headspace vapor is injected into the GC system and split by the column, analyzed by the FID detector in the GC system.

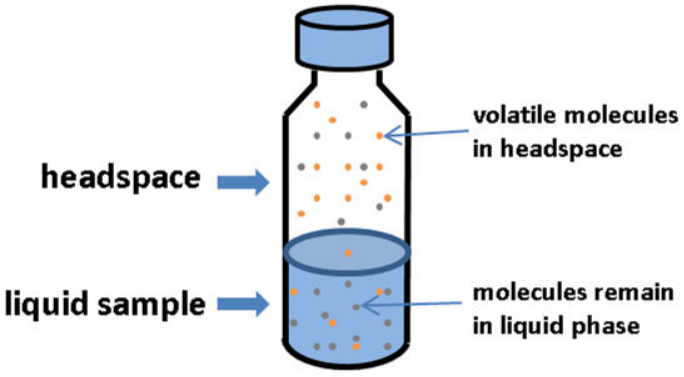

Figure 2.11: *Sealed vial with liquid sample for GC measurement*

FID is widely used to detect combustible components like hydrocarbons. During the measurement, the headspace injector with a temperature of 150 °C injects 1 mL/min to the column with He purge of 5 mL/min. 35 mL/min of H_2 and 350 mL/min of air are flown to FID to cause the flame with 30 mL/min of makeup gas (N_2) to sweep the components through the detector. When a gas sample is introduced into FID, the hydrocarbons present are burnt because of the hydrogen flame in FID. Then the ions produced from the combustion are collected by a metal collector leading to an ionization current which is proportional to the concentration of the hydrocarbons in injected gas.

High performance liquid chromatography (HPLC)

High performance liquid chromatography (HPLC) is a powerful technique to identify and quantify different components in a liquid mixture. Therefore it is very useful to study the liquid products of CO_2RR in the electrolyte, especially suited for organic acids like formic acid/formate ($COOH^-$) which are non-volatile, and therefore not detectable in HS-GC. In the Ultimate 3000 (Thermo Scientific) HPLC system, a HyperREZ XP Carbohydrate H+ LC column is used to separate different compounds in the electrolyte sample, and UV, as well as IR detectors are used to detect the organic acids in the sample.

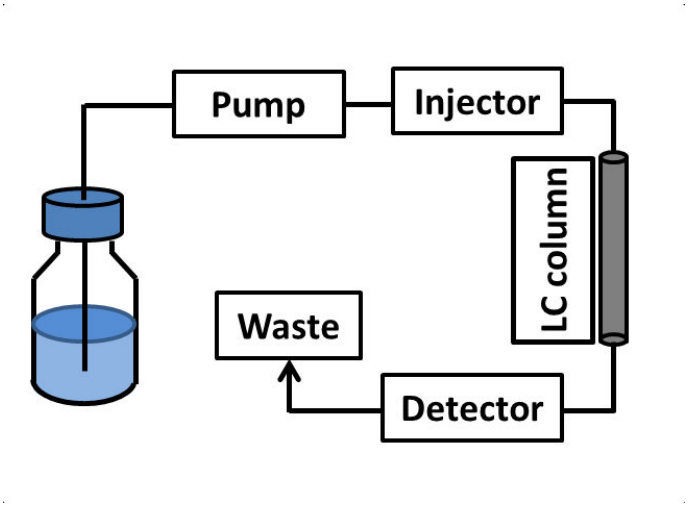

Figure 2.12: *Simplified scheme of HPLC system*

Chapter 3

$(NH_4)_2Mo_3S_{13}$ as electrocatalyst and semiconducting co-catalyst on WSe_2 for HER

Ammonium thiomolybdate ($(NH_4)_2Mo_3S_{13}$, ATM), has been described as highly active HER electro-catalyst in literature. In this contribution, the cluster material was tested as electrocatalyst for HER, and as semiconducting co-catalyst deposited on highly (001)-textured p-type WSe_2 photocathodes, which were earlier grown by an amorphous solid-liquid crystallization process (aSLcS). The $(NH_4)_2Mo_3S_{13}$ catalyst forms a heterojunction with WSe_2, and passivate surface states of the textured WSe_2 layer at the thiomolybdate-WSe_2 interface, leading to a significant improvement in the photocurrent under illumination. Besides that, the thermal stability of $(NH_4)_2Mo_3S_{13}$ will be discussed as well.

Parts of this chapter were adapted from: Xi F, et al. $(NH_4)_2Mo_3S_{13}$ as electrocatalyst and semiconducting co-catalyst deposited on WSe_2 photocathode for water splitting. *In preparation.*

3.1 Introduction

As mentioned in Chapter 1, MoS_2 has been studied as HER catalyst since 1977 when Tributsch et al. worked on it for the first time. [123, 124] According to Jaramillo et al. [16], the active sites of the MoS_2 catalyst are located on the edge sites of the layer structure while the basal planes are catalytically inert. Therefore later, molybdenum sulfides with different structures and higher ratio of edge sites attracted much attention. Among them, ammonium thiomolybdate ($(NH_4)_2Mo_3S_{13}$) stood out because of its high catalytic ability. It was firstly used as a HER catalyst in 2014 by Kibsgaard et al. [20], showing overpotentials between 0.18 V and 0.22 V at a current density of 10 mA/cm^2 (η_{10}). Since then, more researchers have begun to study this cluster compound to identify the reason for its high activity and to further improve its performance.

For example in 2014, Benck et al [125] deposited $[Mo_3S_{13}]^{2-}$ thiomolybdate nanoclusters on top of a MoS_2-Si electrode which shifted the onset potential by 80 mV anodically. Later in 2017, the interaction of $[Mo_3S_{13}]^{2-}$ clusters with different metal substrates such as Au, Ag, C and Cu, was studied by Hellstern et al. [126] for the HER activity where $[Mo_3S_{13}]^{2-}$ on Au substrate showed the highest activity.

In this chapter, $(NH_4)_2Mo_3S_{13}$ nanoclusters were studied as an electrocatalyst for HER and in addition as a co-catalyst deposited on the surface of WSe_2, a p-type semiconductor with high stability in both acidic and alkaline solutions. WSe_2 has an indirect band gap of 1.4 eV and a direct band gap of 1.7 eV according to literature. [127] As an electrocatalyst, the ATM thin film deposited on FTO by spin-coating, obtained an overpotential of 220 mV vs. RHE at 10 mA/cm^2. Differential electrochemical mass spectrometry (DEMS) measurements prove that the H_2 evolution was accompanied by a release of H_2S during HER. The active sites of the Mo_3S_{13} cluster were identified by DFT calculations showing that the sulfur atoms at the terminal positions of the cluster are the most active sites. When used as a co-catalyst deposited on WSe_2 photocathode, a large improvement in the photocurrent of 2.4 mA/cm^2 at 0 V vs. RHE, was achieved while only a relatively low photocurrent of about 0.02 mA/cm^2 at 0 V vs. RHE was achieved without the catalyst. The catalytic mechanism of Mo_3S_{13} nanoclusters as a co-catalyst was studied electrochemically by Intensity Modulated Photocurrent Spectroscopy (IMPS). The conclusion can be made from our study that a thin layer of $(NH_4)_2Mo_3S_{13}$ could influence the band bending and passivate the surface states of the WSe_2 photoelectrode. Combining with the study of the semiconducting properties of $(NH_4)_2Mo_3S_{13}$

and WSe_2, a beneficial band alignment at the WSe_2/ATM interface was discovered.

3.2 Results and discussion

3.2.1 Structural characterization of $(NH_4)_2Mo_3S_{13}$ electrodes

The crystal structure of $(NH_4)_2Mo_3S_{13}$ is shown in Fig. 3.1. In this figure, the red, purple, yellow, blue and pink balls stand for crystal water, molybdenum, sulfur, nitrogen, and hydrogen, respectively. In the $[Mo_3S_{13}]^{2-}$ ligands, three different kinds of sulfur atoms are present: one apical S^{2-} in the middle of the cluster which is bonded with three Mo atoms, three bridging $[S_2]^{2-}$ units where each sulfur atom is bonded with two Mo atoms each, and three terminal $[S_2]^{2-}$ units where each sulfur atom is bonded with one Mo atom each.

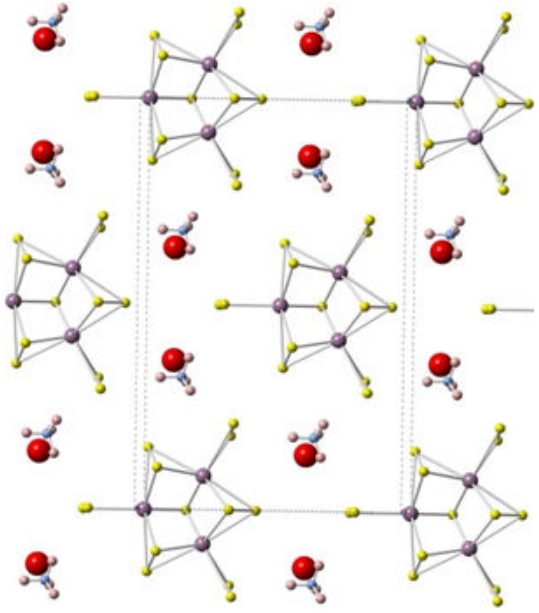

Figure 3.1: *$(NH_4)_2Mo_3S_{13}$ crystal structure: crystal water molecules (red balls), molybdenum atoms (purple), sulfur atoms (yellow), nitrogen atoms (blue), hydrogen atoms (pink)*

The XRD pattern of the synthesized $(NH_4)_2Mo_3S_{13}$ powder is shown in Fig. 3.2A which corresponds to the typical pattern of $(NH_4)_2Mo_3S_{13}$. [20] After spin-coating using solvents such as methanol and dimethyl sulfoxide (DMSO) for ATM, a compact and homogeneous thin film of $(NH_4)_2Mo_3S_{13}$ with a brownish color can be deposited on FTO substrate. The appearance of the spin-coated film using DMSO

solvent is shown by the photograph in Appendix A Fig. A.1. The thickness of the spin-coated film was determined by the cross-sectioned SEM. Fig. A.2 shows that the thickness of $(NH_4)_2Mo_3S_{13}$ film, which was spin-coated for five times, was about 70 nm. However, the crystallinity of the material vanishes after spin-coating, since in the XRD pattern of the spin-coated $(NH_4)_2Mo_3S_{13}$ on FTO, no diffraction peaks were observed from the film other than the peaks from the FTO substrate itself (see Fig. A.3).

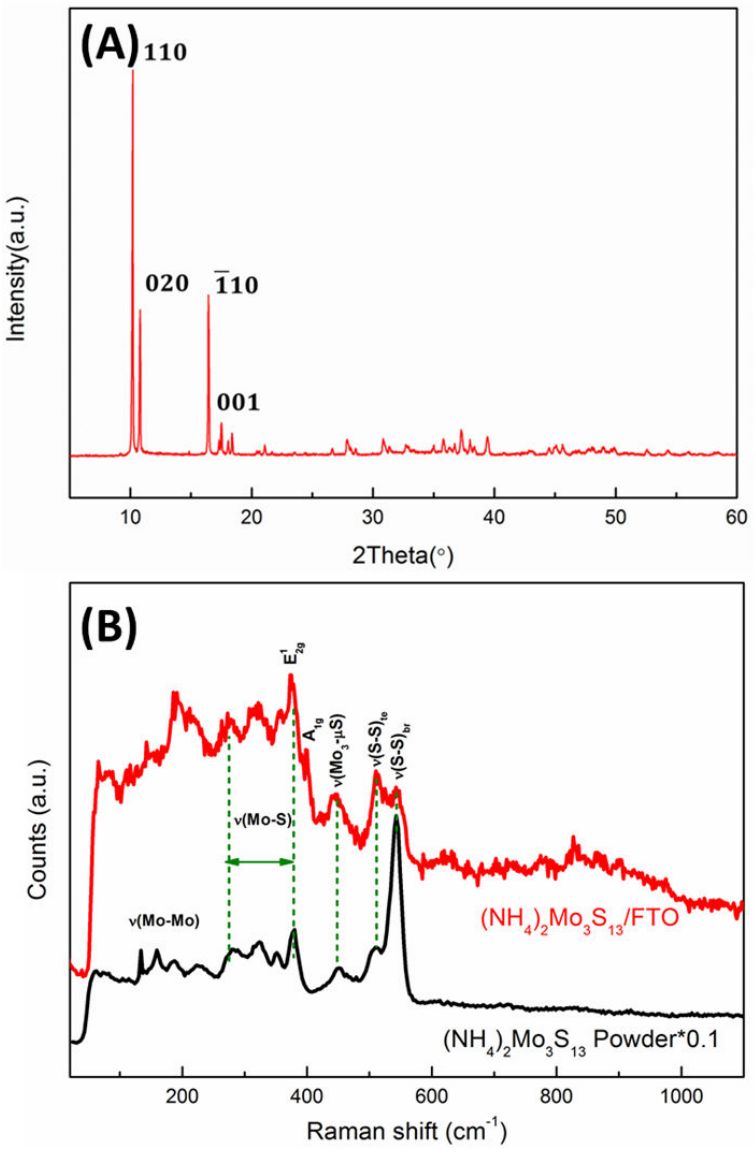

Figure 3.2: *(A) XRD pattern of $(NH_4)_2Mo_3S_{13}$ powder; (B) Raman spectra of $(NH_4)_2Mo_3S_{13}$ powder (black) and $(NH_4)_2Mo_3S_{13}$ thin film on FTO (red)*

Fig. 3.2 shows the Raman spectra of $(NH_4)_2Mo_3S_{13}$ in the form of powder and thin film. As it is shown by the red curve in Fig. 3.2B, the Raman spectrum of the thin

film is similar to the original powder documented by the characteristic vibrational modes of $(NH_4)_2Mo_3S_{13}$, i.e. the vibrational modes of terminal S-S bonding (ν(S-S)$_{te}$) at 510 cm^{-1} and bridging S-S bonding (ν(S-S)$_{br}$) at 542 cm^{-1}. It was noticed that the height of ν(S-S)$_{te}$ is lower than the peak of ν(S-S)$_{br}$ in the Raman spectrum of $(NH_4)_2Mo_3S_{13}$ as shown by the black curve. Possible reason for that could be that the terminal $[S_2]^{2-}$ has another small peak at 504 cm^{-1} according to Müller et al. [128] which could be observed in the Raman spectrum of the original powder as shown by the black curve in Fig. 3.2B. The vibration mode at 450 cm^{-1} can be assigned to the bonding between Mo and apical S. From the XRD pattern and Raman spectra, it can be concluded that, although the spin-coated $(NH_4)_2Mo_3S_{13}$ film has lesser crystallinity than the original powder, the characteristic bonding in the cluster structure still exist.

3.2.2 Thermal stability of $(NH_4)_2Mo_3S_{13}$ powder

The thermal stability of $(NH_4)_2Mo_3S_{13}$ powder was studied through a thermogravimetric analyzer (TGA) system coupled with a quadrupol mass spectrometer (MS) in the temperature range from 30 °C to 1000 °C using a heating rate of 10 °C/min. An Argon(Ar) flow with a flow rate of 80 mL/min was used during the whole measurement. Fig. 3.3 shows the TGA/MS results of $(NH_4)_2Mo_3S_{13}$ powder. The TG curve is shown by the red solid curve and the black dotted line shows the related differential thermal analysis (DTA) curve. The left Y axis represents the ion current monitored with the mass spectrometer.

At the beginning of the measurement, the weight of $(NH_4)_2Mo_3S_{13}$ powder slightly increases until 100 °C due to a buoyancy effect. In the temperature range from 100 °C and 250 °C, the weight of $(NH_4)_2Mo_3S_{13}$ starts to decrease because of the loss of crystal water. The first decomposition step can be described as:

$$(NH_4)_2Mo_3S_{13} \bullet nH_2O(s) \rightarrow (NH_4)_2Mo_3S_{13}(s) + nH_2O(s) \tag{3.1}$$

In this equation, n stands for the number of crystal water per molecule in the $(NH_4)_2Mo_3S_{13}$ powder, which is normally between 0 to 2. Therefore, the weight of the powder at 250 °C where all crystal water is released, is set to 100% for easier calculation of further decomposition steps. At a temperature higher than 250 °C, the decomposition of $(NH_4)_2Mo_3S_{13}$ starts along with the increase in the MS signals. The mass/charge ratio of 17, 16, 15 are related to the ions NH_3^+, NH_2^+ and NH^+, pointing to the release of NH_3 and the signal 34, represents the release of H_2S. DTA

signal shows that this reaction happens at about 330 °C. Therefore, the reaction equation in this decomposition range can be formulated as:

$$(NH_4)_2Mo_3S_{13}(s) \rightarrow NH_3 + H_2S(g) + Mo_3S_{12}(s) \tag{3.2}$$

However, in this temperature range, the reaction under the release of NH_3 and H_2S is not completely finished because as the temperature increases to 405 °C, another part of ammonium and sulfur ion in $(NH_4)_2Mo_3S_{13}$ was released as NH_3 and H_2S as shown by the MS signals. Later at around 415 °C, signals with mass/charge ratios 64, 160 and 192, which can be addressed to $[S_2]^+$ and $[S_5]^+$, $[S_6]^+$, show a large increase. This means that sulfur is released in this decomposition step. In the considered temperature range, the weight of the material decreases from 93.0% to 72.5%. The main reaction of decomposition in this region could be written as:

$$Mo_3S_{13}(s) \rightarrow 3MoS_3(s) + mS_g \tag{3.3}$$

It should be noticed that sulfur is released not only in the form of S_2 molecules, but also higher sulfur polymers (S_2-S_8). Therefore, the number of S atoms (x) in each molecule and the number of the molecules are not fixed in the reaction equation.
After this pronounced loss of weight, the speed of weight loss begins to decrease whereas sulfur in the material is continuously released according to the broad peak with mass/charge ratio of 64 in the temperature range from 470 °C to 600 °C. The weight in this part decreases from 72.5% to 66.8%. The reaction equation in this region can be written as:

$$MoS_3(s) \rightarrow MoS_2(s) + 0.5S_2(g) \tag{3.4}$$

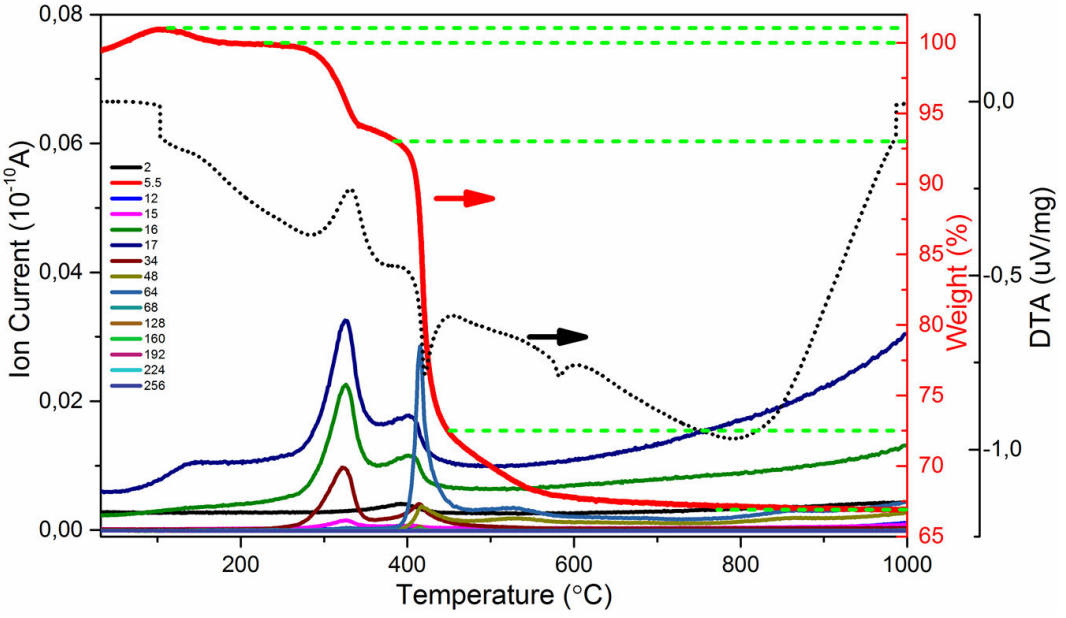

Figure 3.3: *TGA/MS of $(NH_4)_2Mo_3S_{13}$ in a temperature range from* 30 °C *to* 1000 °C

XRD pattern of the powder after TG measurement is shown in Fig. A.4 in Appendix A, which corresponds to the standard pattern of 2H-MoS_2. Therefore, it can be said from the TG measurement that the $(NH_4)_2Mo_3S_{13}$ decomposes to MoS_2 eventually by releasing H_2S, NH_3 and sulfur gas species with increasing temperature.

In the following chapters, it will be shown that not only $(NH_4)_2Mo_3S_{13}$, but also sulfur rich MoS_x has the characteristic of releasing sulfur. In contrast to TGA properties discussed above, the release of sulfur that would be discussed in the following section, is initiated electrochemically.

3.2.3 Semiconducting properties of $(NH_4)_2Mo_3S_{13}$

The optical band gap and the absorption coefficient of spin-coated $(NH_4)_2Mo_3S_{13}$ were deviated from UV-vis spectroscopy. Fig. 3.4A shows the absorption coefficient (α) of $(NH_4)_2Mo_3S_{13}$ plotted as a function of wavelength in the range of800 nm to 400 nm. For a wavelength lower than about 650 nm, which corresponds to photons with energy higher than 1.9 eV, the absorption coefficient is in the range from 9.3×10^3 cm^{-1} to 2.3×10^4 cm^{-1}. Therefore, the penetration depth (α^{-1}) for $(NH_4)_2Mo_3S_{13}$ is $\sim$ 435 nm - 1 µm. As shown by the Tauc plots, an indirect optical transition starts at about 1.7 eV (see Fig. 3.4B) and a direct transition starts at 1.9 eV (see Fig. 3.4C).

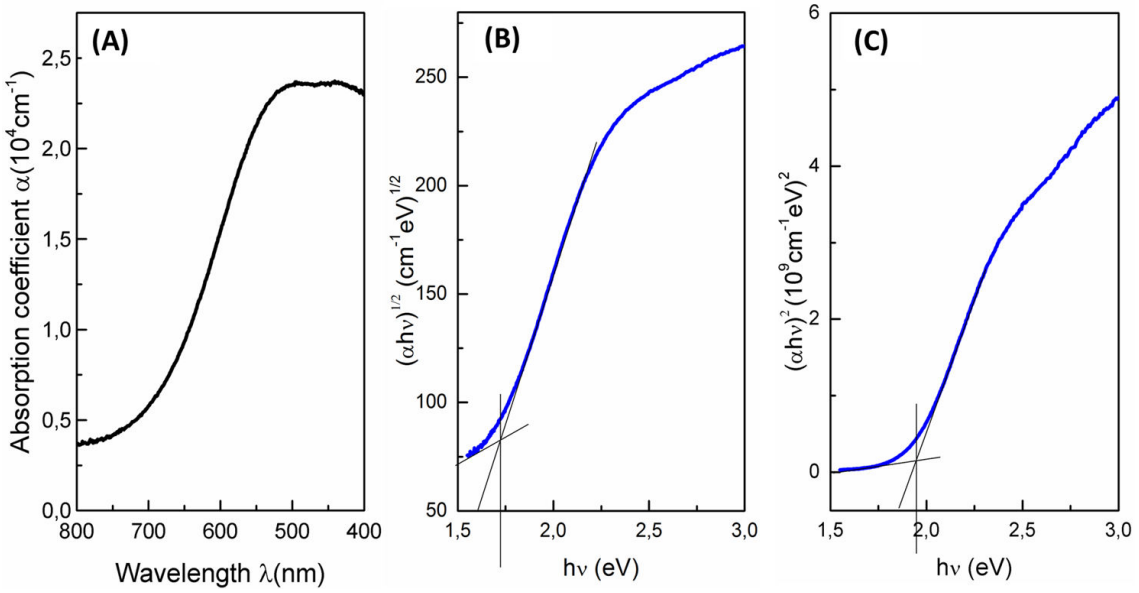

Figure 3.4: *UV-vis measurement of $(NH_4)_2Mo_3S_{13}$ deposited on FTO: (A) Absorption coefficient as a function of wavelength; (B) indirect Tauc plot (band gap evaluated from $((\alpha h\nu)^{1/2})$; (C) direct Tauc plot (band gap evaluated from $((\alpha h\nu)^2)$ as a function of light energy*

To determine the work function (Fermi level of a semiconductor, Φ) and the valence band maximum (VBM) of $(NH_4)_2Mo_3S_{13}$, contact potential difference (CPD) measurements and air photoemission spectroscopy (AES) measurements were performed using Kelvin probe microscopy. Since a decrease of crystallinity was observed after the deposition of $(NH_4)_2Mo_3S_{13}$ on FTO, thin film and powder sample were both measured for comparison. For powder analysis, 11 mg of $(NH_4)_2Mo_3S_{13}$ powder was pressed into a pellet with a diameter of 5 mm.

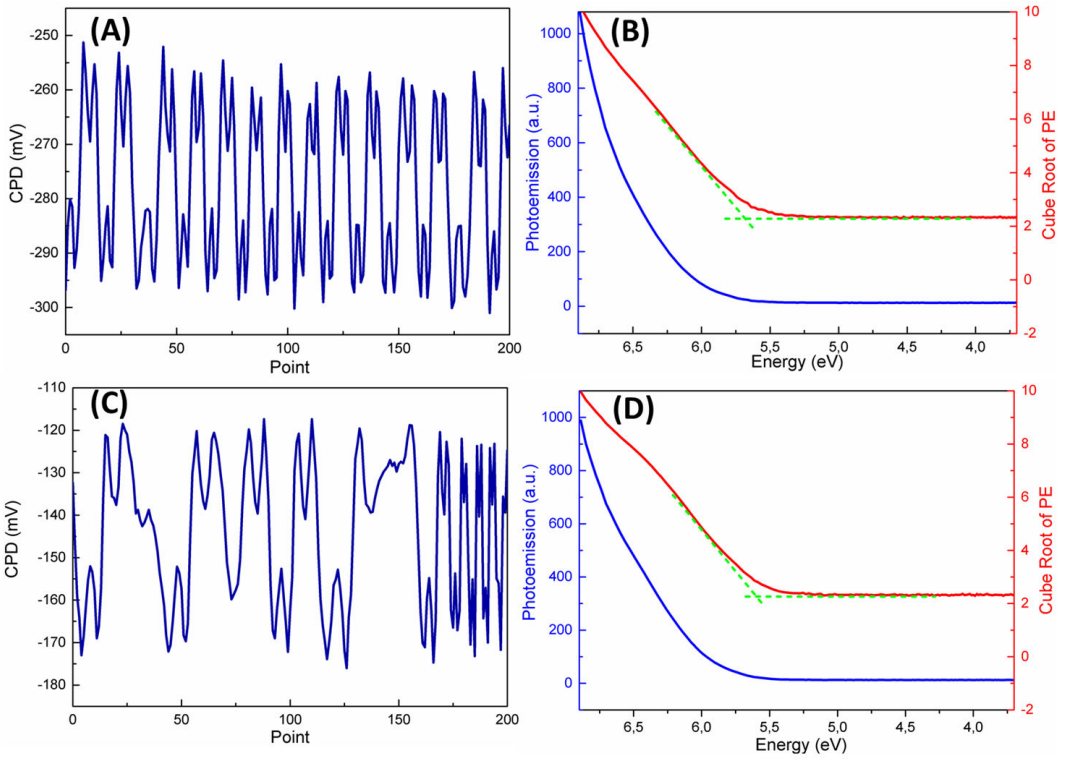

Figure 3.5: *Work function and valence band maximum of $(NH_4)_2Mo_3S_{13}$: (A)(B) spin-coated $(NH_4)_2Mo_3S_{13}$ on FTO; (C)(D) $(NH_4)_2Mo_3S_{13}$ powder*

The CPD measured by Kelvin probe for the thin film sample and the powder are shown in Fig. 3.5A and C. The work function of the sample can be determined by the equation:

$$\Phi_{\text{sample}} = \Phi_{\text{tip}} + CPD \tag{3.5}$$

The work functions of the tip in Fig. 3.5A and C, calibrated with standard Au, were 4.904 eV and 4.948 eV respectively. The CPD values obtained from Fig. 3.5A and C are about -270 mV, -145 mV. Therefore the work function can be calculated from Eq. 3.5. For each sample, the work functions were measured at three different points and the average value was taken. Finally, the work function of the thin film $(NH_4)_2Mo_3S_{13}$ sample which amounts to about 4.7 eV and the work function of

$(NH_4)_2Mo_3S_{13}$ powder at about 4.8 eV was determined.

In AES measurement, as a semiconductor, the VBM could be extracted from the cube root of the photoemission according to Fowler et al. [122]. The intercept of the straight part of the cube root photoemission curve with the baseline gives the energetic position of VBM. In Fig. 3.5B, the VBM measured from a $(NH_4)_2Mo_3S_{13}$ thin film lied at about 5.7 eV. And for $(NH_4)_2Mo_3S_{13}$ powder, as shown in Fig. 3.5C, it was positioned at 5.6 eV. The small differences of the work function and the VBM in thin film and powder can be explained by the structural changes of $(NH_4)_2Mo_3S_{13}$ during the spin-coating process, which was also confirmed by XRD measurements (see Fig. A.3)

By combining Kelvin Probe measurements and UV-vis results, the band diagram of $(NH_4)_2Mo_3S_{13}$ thin film with respect to the vacuum level and the electrochemical scale vs. NHE could be derived as illustrated in Fig. 3.6. The position of redox potential of H^+/H_2 is located between the conduction band minimum (CBM) and the Fermi level of $(NH_4)_2Mo_3S_{13}$ while the position of the redox potential of (H_2O/O_2) is close to the VBM position. The position of the Fermi level in the middle between CBM and VBM reveals that the $(NH_4)_2Mo_3S_{13}$ is nearly an intrinsic semiconductor.

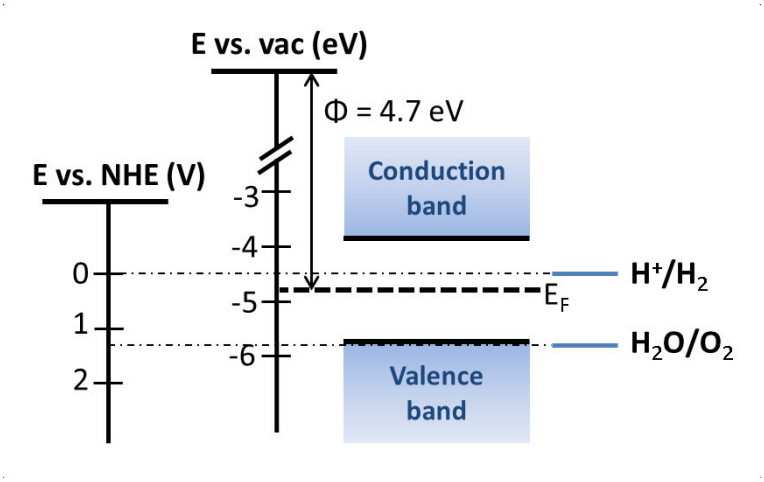

Figure 3.6: *Band positions of $(NH_4)_2Mo_3S_{13}$ thin film deposited on FTO with respect to vacuum level and electrochemical scale vs. NHE*

3.2.4 $(NH_4)_2Mo_3S_{13}$ as electro-catalyst for HER

Electrocatalytic performance of $(NH_4)_2Mo_3S_{13}$ electrodes

$(NH_4)_2Mo_3S_{13}$ was deposited on FTO substrates by drop-casting and spin-coating, repectively, using different solvents such as methanol and DMSO. The performance of

the electrodes prepared with different methods and solvents were measured by cyclic voltammetry in the voltage range from 0.2 V to −0.3 V vs. RHE in 0.5 M H_2SO_4 aqueous electrolyte with a scan rate of 10 mV/s. The results are shown in Fig. 3.7A. Best performance (235 mV at $-10\,mA/cm^2$) was achieved with spin-coated samples fabricated using DMSO as solvent. $(NH_4)_2Mo_3S_{13}$ is less soluble in methanol and the drop-casted layers using methanol as solvent exhibited lesser homogeneity and adherence, causing higher overpotentials. On the other hand, the layers deposited by spin-coating, using DMSO solvent, leads to a homogeneous distribution of the material on the FTO surface. The thickness of the film after five depostion cycles was about 70 nm as shown in Fig. A.2. The catalytic capability of these electrodes is still inferior to Jaramillo's best results (180 mV at $-10\,mA/cm^2$) [20]. A possible explanation is that the graphite paper used as substrate in their study has higher surface area and larger loading of catalyst than the FTO substrate used in our experiments.

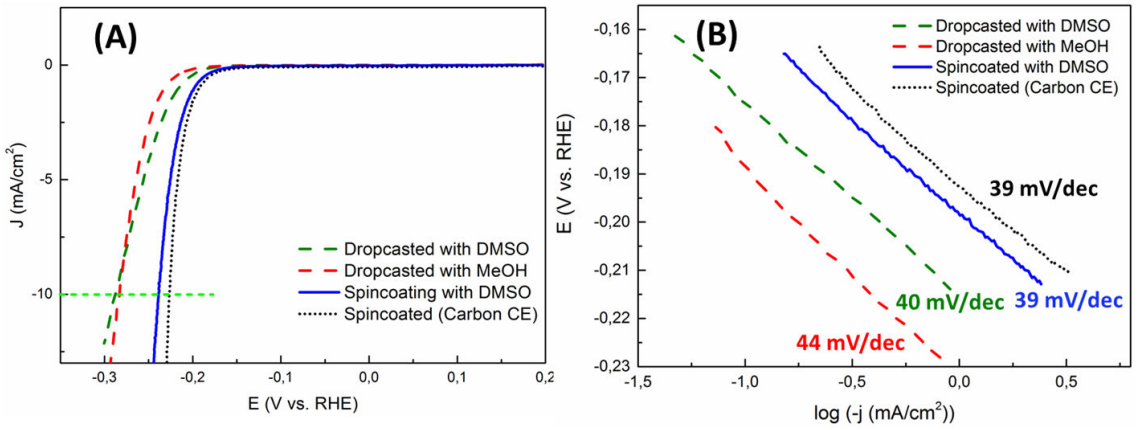

Figure 3.7: *(A) CV measurements of $(NH_4)_2Mo_3S_{13}$ electrodes, (B) Tafel plot of $(NH_4)_2Mo_3S_{13}$ electrodes deviated from CV measurements*

In our study, glassy carbon was also used as CE besides Pt, since when measuring HER using Pt as CE in the electrochemical measurement, Pt can get dissolved in the electrolyte and then be redeposited on the surface of WE, causing an improvement in its catalytic activity. The black dotted line in Fig. 3.7A shows a spin-coated $(NH_4)_2Mo_3S_{13}$ sample measured with carbon CE instead of Pt CE. The overpotential of this sample at $-10\,mA/cm^2$ is about 220 mV which is similar to the results obtained with Pt as CE.

Fig. 3.7B shows the potential plotted as a function of the logarithm of the absolute current density extracted from CV results. The obtained curves are called Tafel plots. The Tafel plots of $(NH_4)_2Mo_3S_{13}$ electrodes with corresponding values of

Tafel slopes are shown in Fig. 3.7B which elucidate the rate-limiting step during the hydrogen production. [98] As mentioned before, hydrogen evolution is a two-step process which can be formulated by firstly a proton reduction step (also known as Volmer step):

$$H^+ + e^- + * \rightarrow H^* \tag{3.6}$$

with a Tafel slope b = 2.3RT/αF ≈ 120 mV.
Followed by a hydrogen desorption step. Two alternatives are possible in this step. One is the Heyrovsky step:

$$H^+ + e^- + H^* \rightarrow H_2 \tag{3.7}$$

with b = 2.3RT/(1+α)F ≈ 40 mV.
And the other is the Tafel step corresponding to the equation:

$$2H^* \rightarrow H_2 + 2* \tag{3.8}$$

with b= 2.3RT/2F ≈ 30 mV.

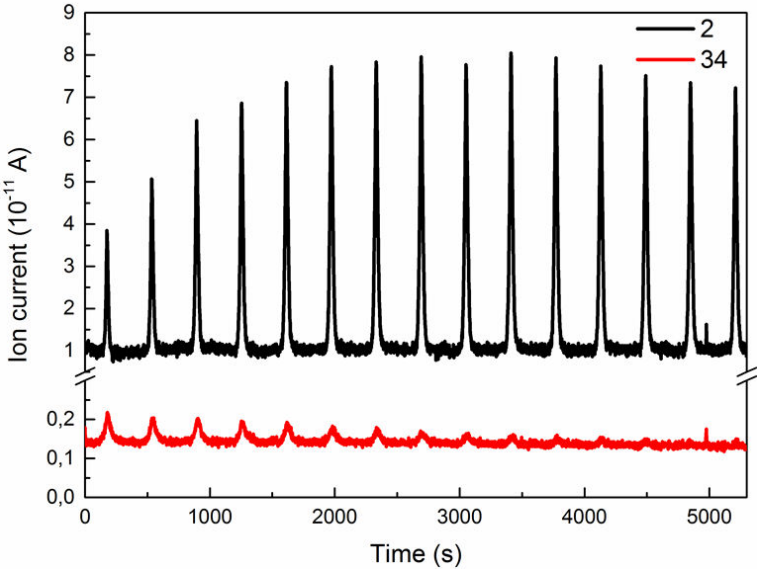

Figure 3.8: *DEMS measurement of $(NH_4)_2Mo_3S_{13}$ thin film*

The asterisk * in these equations represents a reactive site on the catalyst surface, R is the ideal gas constant (8.314 $JK^{-1}mol^{-1}$, T is the absolute temperature (in Kelvin) and α is related to the barrier symmetry factor, which is about 0.5. [129]. For Pt as an HER catalyst, the Tafel slope is usually around 30 mV/decade, which means that the hydrogen evolving process is following the Volmer-Tafel mechanism whereas the Heyrovsky step is the rate limiting step. For $(NH_4)_2Mo_3S_{13}$ samples

prepared using DMSO solution, similar Tafel slopes of around 40 mV/decade was observed. The sample prepared with methanol has slightly higher Tafel slope values with 44 mV/decade. The Tafel slope of $(NH_4)_2Mo_3S_{13}$ electrodes may suggest a Volmer-Heyrovsky HER mechanism and the Heyrovsky step in hydrogen desorption is the rate limiting step.

To study the gaseous products during electrochemistry, DEMS measurement was performed on spin-coated $(NH_4)_2Mo_3S_{13}$ electrode. Fig. 3.8 shows the DEMS result while measuring CV in 0.5 M H_2SO_4 aqueous electrolyte with a scan rate of 2 mV/s. The black curve in Fig. 3.8 shows the signal with mass/charge ratio of 2 which corresponds to H_2 evolution and the red curve with a MS signal of 34 stands for H_2S evolution. At the beginning of the CV measurement, the signal of H_2 is increasing while the signal of H_2S is decreasing. After 2000 s the production of H_2 stabilizes while the production of H_2S becomes negligible. The spikes appearing at about 5000 s in both signals of H_2 and H_2S is caused by a replenishment of the electrolyte at that time. Therefore, from this measurement, it can be concluded that the hydrogen production of the $(NH_4)_2Mo_3S_{13}$ catalyst is proven accompanied by a release of sulfur in the form of H_2S, which suggests that part of the sulfur in $(NH_4)_2Mo_3S_{13}$ catalyst is released during HER.

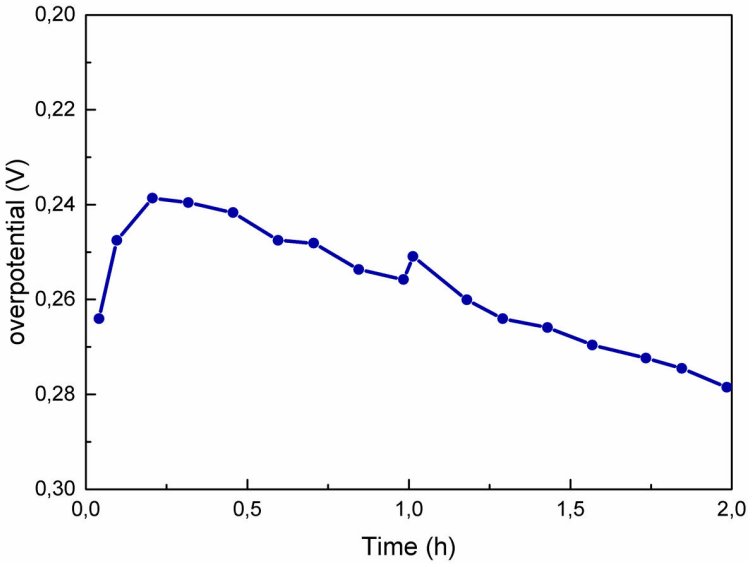

Figure 3.9: *Stability measurement of $(NH_4)_2Mo_3S_{13}$ under CV for* 2 h

Stability is one of the important parameters that should be considered when testing a catalyst. Here, the stability of $(NH_4)_2Mo_3S_{13}$ as electro-catalyst for HER is measured by applying electrochemical cycling for 2 h in the potential range from

0.2 V to −0.3 V vs. RHE. The overpotential of the sample at a current density of $-5\,mA/cm^2$ is plotted as a function of measurement time. The result is shown in Fig. 3.9. As shown in this figure, the overpotential of the electrode decreases in the first 15 min of CV cycling from 0.264 V to 0.238 V, but increases by 40 mV in the 2 h measurement. The peak decrease of the overpotential after 1 h is caused by an exchange of the electrolyte and by removing gas bubbles from the electrode surface. Since the $(NH_4)_2Mo_3S_{13}$ catalyst film is relatively thin (70 nm thick as shown in Fig. A.1), possible reasons for the decrease in the catalytic property during the stability measurement could be a corrosion process as we observed formation of H_2S in the DEMS measurement, or a loss of catalyst material during H_2 bubble formation in electrochemical measurement, due to delamination.

Identification of active centers in $(NH_4)_2Mo_3S_{13}$

To identify the catalytic active centers of $(NH_4)_2Mo_3S_{13}$ as a HER catalyst, DFT calculations were performed. The calculations were based on the following equations:

$$E_{\mathrm{ad}} = E_{\mathrm{total}} - E_{\mathrm{cluster+H}} - \frac{1}{2}E_{\mathrm{H_2}} \tag{3.9}$$

$$\Delta G_{\mathrm{H}}{}^{0} = E_{\mathrm{ad}} - T\Delta S + \Delta ZPE \tag{3.10}$$

where $E_{cluster+H}$ represents a cluster with a certain number of H adsorption, and E_{H_2} is the energy of the H_2 molecule. In the calculation of the Gibbs free energy, T is the temperature in Kelvin, ΔS represents the entropy change of adsorption of H, and ΔZPE is the zero-point energy.

Fig. 3.10 shows the structures of Mo_3S_{13} ligands where hydrogen atom is bonded to sulfur atoms at different positions. The corresponding Gibbs free energy values (ΔG_{H^*}) of H calculated by DFT are listed in Table. 3.1. The upper and lower sulfur atoms are defined by whether they are located on the same side of apical sulfur atom or on the opposite side respectively. As mentioned in Chapter 1, the Gibbs energy of chemisorbed H at the material surface should be close to zero to guarantee that H can be easily absorbed in the first step of HER to the catalyst surface and released as H_2 in the second step. From Table. 3.1, it can be learnt that the sulfur atoms at the terminal sites have lowest absolute values (about −0.1 eV to −0.2 eV) of ΔG_{H^*}, compared to bridging and apical sulfur atoms.

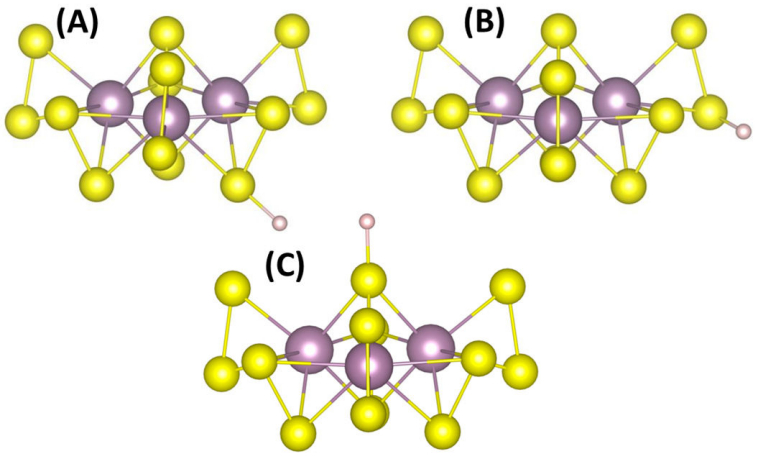

Figure 3.10: *H bonded with different sulfur sites of Mo_3S_{13} cluster: (A) with bridging sulfur; (B) with terminal sulfur; (C) with apical sulfur. Sulfur atoms: yellow balls, molybdenum atoms: purple balls, hydrogen atoms: pink balls*

Table 3.1: *The binding energy of an adsorpted H atom (E_{ad}) (eV) and the Gibbs free energy (ΔG_{H^*}) (eV), the bond length (Å) of first H^* adsorpted on different sulfur sites in Mo_3S_{13} cluster*

Sulfur sites	$\mathbf{E_{ad}}$**(eV)**	$\mathbf{\Delta G_{H^*}}$	**bond length(Å)**
apical	0.895	1.13	1.364
$\mathbf{terminal_{up}}$	-0.36	-0.117	1.369
$\mathbf{terminal_{lower}}$	-0.45	-0.209	1.368
$\mathbf{bridging_{up}}$	1.678	1.92	1.383
$\mathbf{bridging_{lower}}$	1.567	1.80	1.410

The corresponding ΔG of the reaction intermediate in $(NH_4)_2Mo_3S_{13}$ is also shown in Fig. 3.11. This result means that $(NH_4)_2Mo_3S_{13}$ possesses excellent HER catalytic ability mainly due to the terminal $[S_2]^{2-}$ which are the most active sulfur sites.

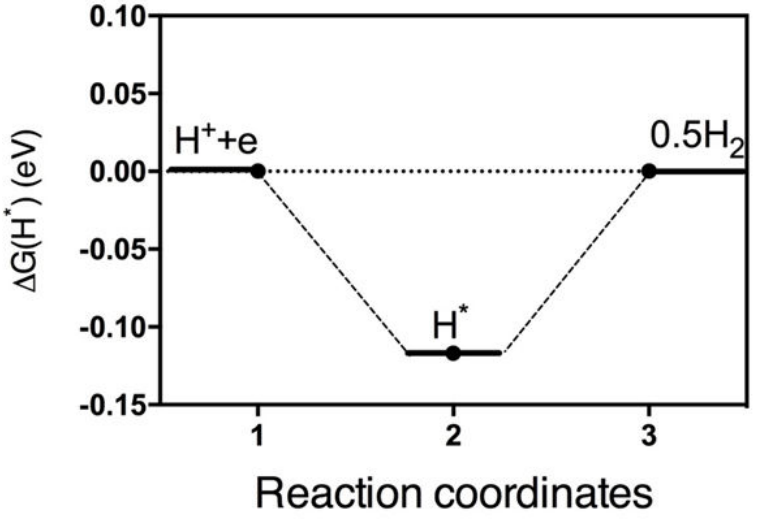

Figure 3.11: *Calculated free energy of the reaction intermediate in $(NH_4)_2Mo_3S_{13}$(in eV).*

3.2.5 $(NH_4)_2Mo_3S_{13}$ as co-catalyst for WSe_2 photocathode

Photoelectrochemical performance of $(NH_4)_2Mo_3S_{13}/WSe_2$

$(NH_4)_2Mo_3S_{13}$ can not only be used as an efficient HER electro-catalyst, but also as a co-catalyst deposited on p-type semiconductors to improve the overall photoelectrochemical performance of the photocathode. In this aspect, WSe_2 electrodes prepared by aSLcS method using reactive magnetron sputtering, exhibiting a (001)-textured polycrystalline layer structure were chosen as an example. The $(NH_4)_2Mo_3S_{13}$ catalyst was deposited on WSe_2 by spin-coating using DMSO as a solvent. Fig. 3.12 shows the linear scan voltammetry (LSV) results of WSe_2 electrodes immersed in 0.5 M sulfuric acid electrolyte under chopped AM1.5 illumination. As shown in the figure by the black curve, before the deposition of $(NH_4)_2Mo_3S_{13}$, the photocurrent of the bare WSe_2 electrode was relatively small (about 0.02 mA/cm^2 at 0 V vs. RHE). However, the photocurrent of the electrode after the deposition of $(NH_4)_2Mo_3S_{13}$, onsets at about 0.2 V, and considerably increases to about 2.4 mA/cm^2 at 0 V vs. RHE. According to Bozheyev et al. [130], after optimization of the preparation parameters of WSe_2 film and the thickness of $(NH_4)_2Mo_3S_{13}$ layer, a maximum photocurrent of 5.6 mA/cm^2 could be reached at 0 V vs. RHE.

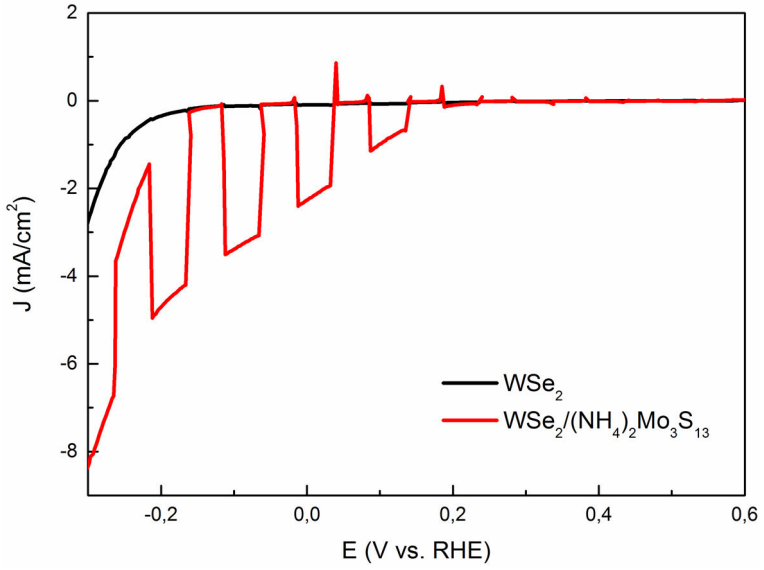

Figure 3.12: *LSV curves of WSe_2 and $WSe_2/(NH_4)_2Mo_3S_{13}$ under AM1.5 illumination using chopped light*

Catalytic mechanism study of $(NH_4)_2Mo_3S_{13}$ as a co-catalyst for WSe_2

In principle, co-catalysts deposited on the surface of a semiconductor can either improve the charge transfer, and/or suppress the surface recombination at the electrode/electrolyte interface, modify the band alignment. In these cases, the deposition of a co-catalyst affects the charge separation (η_{CS}) and/or the charge transfer effiency (η_{CT}). [24] When p-type WSe_2 is used as photocathode for hydrogen evolution, η_{CS} means the fraction of photogenerated electrons that reaches the electrode surface while η_{CT} is defined as the fraction of electrons transferred from the semiconductor surface into the electrolyte. Normally, η_{CT} equals to $k_{tr}/(k_{tr}+k_{rec})$ where k_{tr} is the first order rate constant of electron transfer and k_{rec} is first order rate constant of surface recombination. Hence, the fraction of electrons lost by surface recombination is 1 - η_{CT}. [131]

The catalytic mechanism of $(NH_4)_2Mo_3S_{13}$ as a co-catalyst on WSe_2 was studied through IMPS measuremenst by modulating the light intensity and recording the photocurrent response. The values of reaction rate constants of charge transfer (k_{tr}) and surface recombination (k_{rec}) can be later calculated based on a simplified model described by L. Peter et al. [132] (see details in Chapter 2, part 2.2.1).

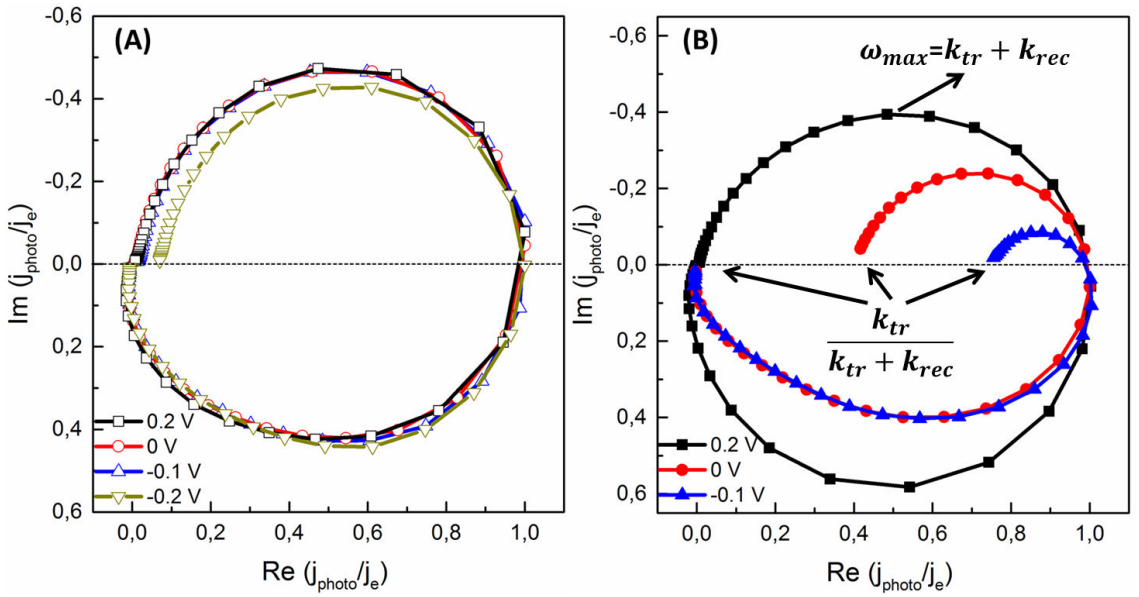

Figure 3.13: *IMPS spectra at different potentials: (A) bare WSe_2; (B) $(NH_4)_2Mo_3S_{13}$ spin-coated on WSe_2*

During the measurement, the $(NH_4)_2Mo_3S_{13}/WSe_2$ and the bare WSe_2 photocathodes were fixed at different potentials for each IMPS spectrum ranging from $-0.1\,V$

to 0.5 V vs. RHE. The obtained spectra are shown in Fig. 3.13 where all high frequency intercepts (Real current intercept in x-axis) of the obtained spectra were normalized to 1 for a comparison. As a response, the imaginary current parts shown by the y-axis were divided by the high frequency intercepts as well. Fig. 3.13A shows the measured IMPS spectra of bare WSe_2 at −0.2 V, −0.1 V, 0 V and 0.2 V vs. RHE. As mentioned before, the value of low frequency intercept in normalized IMPS spectrum yields the value of $k_{rec}/(k_{rec}+k_{tr})$, which represents the charge transfer efficiency (η_{CT}). Therefore for a bare WSe_2 photocathode, the η_{CT} values are close to zero, even at −0.2 V, which means that most of the photo-generated electrons that reaches the semiconductor surface are lost due to surface recombination other than being injected into the electrolyte. However, the IMPS results in Fig. 3.13B show that for $(NH_4)_2Mo_3S_{13}$ coated WSe_2 electrode, nearly all electrons recombines at −0.2 V, but the η_{CT} value is increasing as the potential goes towards negative direction according to the shrinking size of the recombination semicircles.

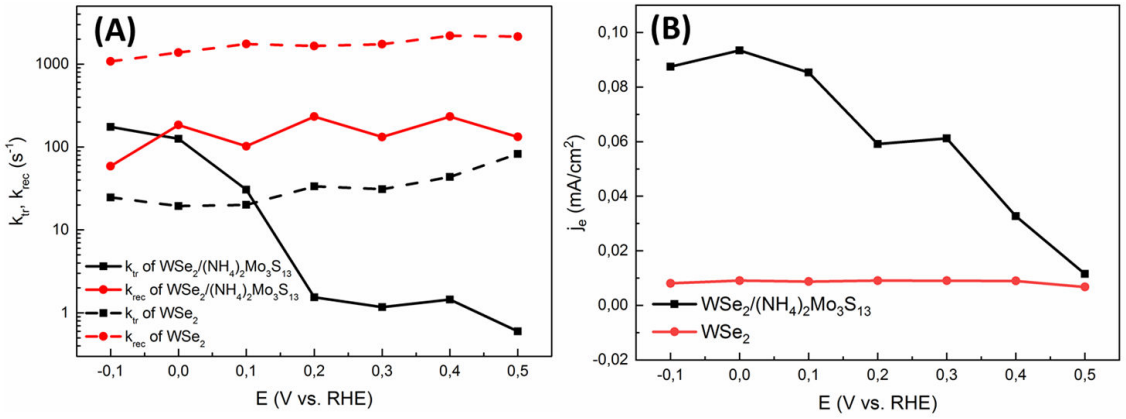

Figure 3.14: *(A) k_{rec} (red color) and k_{tr} (black color) calculated from IMPS: $WSe_2/(NH_4)_2Mo_3S_{13}$ (solid curves), WSe_2 (dashed curve); (B) electron current before recombination: WSe_2 (red), $WSe_2/(NH_4)_2Mo_3S_{13}$ (black)*

To study the function of the $(NH_4)_2Mo_3S_{13}$ catalyst on WSe_2 in detail, k_{rec} and k_{tr} values were calculated from IMPS spectra based on Eq. 2.2 and Eq. 2.3 which are also shown in Fig. 3.13B. The results are given in Fig. 3.14A as a function of applied potentials. WSe_2 coated with $(NH_4)_2Mo_3S_{13}$ is shown as solid curves while bare WSe_2 is shown as the dashed curves. It can be concluded from this figure that k_{rec} of the sample is suppressed by a factor of 10 to 20 after the deposition of $(NH_4)_2Mo_3S_{13}$ in complete potential range, which suggests that $(NH_4)_2Mo_3S_{13}$ passivats the WSe_2 surface and decreases the recombination rate. Considering the bare WSe_2 electrode, the k_{tr} value is relatively constant at all potentials. However,

after being coated with $(NH_4)_2Mo_3S_{13}$, the k_{tr} becomes much smaller than that of bare WSe_2 in the potential range from 0.5 V to 0.2 V, but it starts to increase from 0.2 V while scanning towards the negative potentials, corresponding to the photocurrent onset observed in Fig. 3.12. At 0.1 V, the k_{tr} of $WSe_2/(NH_4)_2Mo_3S_{13}$ is already higher than that of bare WSe_2. At −0.1 V, the k_{tr} is higher by a factor of 7 as compared to bare WSe_2.

Interestingly, other than the changes in k_{tr} and k_{rec}, the high frequency intercepts of the semicircles with x-axis in the the IMPS spectra of $WSe_2/(NH_4)_2Mo_3S_{13}$, which correspond to the current of electrons that arrive at the semiconductor surface before they can recombine, is also different compared to the that of uncoated WSe_2. In Fig. 3.14B, the intercepts of the two electrodes are plotted versus the applied potentials. At 0.5 V, the electron current of these two samples are similar. But when the potential changes in the cathodic direction, the electron current for WSe_2 remains below 0.01 mA/cm^2 as shown by the red curve, while the current for $WSe_2/(NH_4)_2Mo_3S_{13}$ shown by the black curve keeps increasing and reaches a value of about 0.1 mA/cm^2 at potential lower than 0 V. If $(NH_4)_2Mo_3S_{13}$ was only passivating the surface states or increasing the charge transfer rate at the interface, a similar amount of photo-generated electrons that can reach the semiconductor surface before recombination should have been observed in both samples. But since that is not the case, the result can be interpreted as a change of band bending in the electronic structure after the deposition of $(NH_4)_2Mo_3S_{13}$.

To prove the changes in the band bending after the deposition of $(NH_4)_2Mo_3S_{13}$ on WSe_2, the change in the open-circuit potential (ΔOCP) was measured for both samples. The results are shown in Fig. A.5. In this measurement, an Ar ion laser with a wavelength of 457.9 nm was used to provide higher illumination intensity to flatten the band. The power density of the illumination for ΔOCP measurement is 216 mW/cm^2. The results are shown in Fig. A.5. The ΔOCP of bare WSe_2 was around 20 mV while the ΔOCP of $WSe_2/(NH_4)_2Mo_3S_{13}$ is around 150 mV indicating that a change in the band bending at the semiconductor/electrolyte interface is evident. To look into this, the band diagram of $WSe_2/(NH_4)_2Mo_3S_{13}$ will be investigated in the next section.

Band diagram of $WSe_2/(NH_4)_2Mo_3S_{13}$

As suggested by IMPS and ΔOCP measurements, the band bending at the semiconductor/electrolyte interface is modified by the deposition of $(NH_4)_2Mo_3S_{13}$ on

WSe_2. To observe the band alignment of this electrode, Kelvin probe experiments were performed again to determine the VBM and the work function of the WSe_2 electrode. As shown in Fig. A.6, the VBM and the work function of WSe_2 are about 5.3 eV and 5.1 eV respectively. According to Bozheyev et al. [130], the polycrystalline, (001)-textured WSe_2 has a band gap of around 1.51 eV, therefore the band positions of WSe_2 can be drawn as shown in Fig. A.7.
Combining the band positions of WSe_2 and $(NH_4)_2Mo_3S_{13}$, the band diagram of $WSe_2/(NH_4)_2Mo_3S_{13}$ is shown in Fig. 3.15A. The Fermi level of the sample is lower than the redox potential of H^+/H_2. Therefore, when the $WSe_2/(NH_4)_2Mo_3S_{13}$ is in contact with the electrolyte, a slight downwards band bending can be expected as shown in Fig. 3.15B which is beneficial for electrons to be injected into the electrolyte and to further reduce protons resulting in hydrogen evolution.

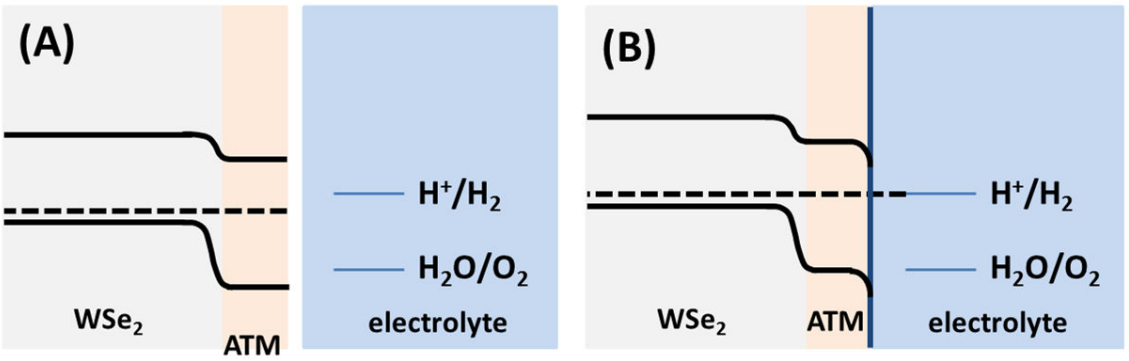

Figure 3.15: *Band alignment of the $WSe_2/(NH_4)_2Mo_3S_{13}$ junction: (A) before contact with the electrolyte; (B) after contact with the electrolyte*

3.3 Conclusion

$(NH_4)_2Mo_3S_{13}$ was synthesized and used as electrocatalyst and as co-catalyst deposited on highly (001)-textured p-type WSe_2 photocathode for hydrogen evolution. As electrocatalyst, best result was obtained for spin-coated electrodes with an overpotential of 220 mV at $-10\,mA/cm^2$. The production of hydrogen using $(NH_4)_2Mo_3S_{13}$ catalyst is accompanied with a release of H_2S in small amount as confirmed by DEMS. The active sites for HER in $(NH_4)_2Mo_3S_{13}$ are located at the terminal $[S_2]^{2-}$ entities. When used as a semiconducting co-catalyst for WSe_2, the catalyst with a direct band gap of 1.9 eV, is able to form a hetero-junction with WSe_2 to improve the band bending, and passivate surface states of the textured WSe_2 film. A significant improvement in the photocurrent of the electrode immersed in 0.5 M

sulfuric acid electrolyte (pH 0.3) could be achieved after the deposition of a thin $(NH_4)_2Mo_3S_{13}$ layer on top of WSe_2. The results described in this chapter allow us to identify the active sites of the $(NH_4)_2Mo_3S_{13}$ cluster as an electro-catalyst, and its impact on the band structure of a $WSe_2/(NH_4)_2Mo_3S_{13}$ in light-induced hydrogen evolution.

Chapter 4

Activation of amorphous sputtered MoS_x in aqueous electrolysis

Molybdenum sulfide, a transition metal sulfide material with a unique layer structure, has promoted its use in many fields, for example, as lubricant or as catalyst for hydrodesulfurization of crude oil. In the last decades, it has attracted much interest as a catalyst for the hydrogen evolution reaction (HER) because of its low overpotential and high stability under acidic conditions. Recently, amorphous molybdenum sulfide has been studied as a HER catalyst because of its high catalytic activity. However, the catalytic mechanism of amorphous molybdenum sulfide is still under debate and different catalytic active centers are discussed in literature. In order to further study the catalytic mechanism of molybdenum sulfide, we've prepared a seires of MoS_x with different degrees of crystallinity using reactive magnetron sputtering by varying the substrate temperature from room temperature to 500 °C. The best performing sample were obtained from amorphous MoS_x sputtered at room temperature, showing an overpotential of 180 mV at a current density of $-10\,mA/cm^2$. During electrochemical cycling in the range from 0.2 V to −0.3 V vs. RHE, a release of H_2S connected with an improvement of HER activity were observed from MoS_x sputtered at room temperature which has originally amorphous structure. A phase transformation of room temperature sputtered MoS_x from amorphous structure consisting of $[Mo_3S_{13}]^{2-}$ and $[Mo_3S_{12}]^{2-}$ entities to nano-crystalline MoS_2 was identified by *in-situ*/in-line Raman spectroscopy.

Results described in this chapter are already published in ACS Catalysis in 2019 with the title: "**Structural transformation identification of sputtered amorphous MoS_x as efficient hydrogen evolving catalyst during electrochemical activation**".

4.1 Introduction

As introduced in Chapter 1, MoS_2 has been studied as HER catalyst for decades, but its catalytic ability is still inferior to that of Pt. Therefore, many strategies have been used to improve its HER performance. Besides nanoclusters such as $(NH_4)_2Mo_3S_{13}$, as we discussed already in Chapter 3, amorphous molybdenum sulfide also has attracted much attention since the short range order in this material is dominant, giving the material unique catalytic properties [21, 95]
For instance, Merki et al. [98] prepared amorphous MoS_x thin film catalyst layers electrochemically, which resulted in a significant increase of current density for water reduction at a lower overpotential (15 mA/cm^2 at an overpotential of η=200 mV) compared to the crystalline material. Amorphous MoS_2 HER catalysts were also prepared by Shin et al. using atomic layer deposition. [133] However, the catalyzing mechanism of the amorphous material and the reason for its high catalytic activity are still under debate. As mentioned before, possible reasons were thought to be the high surface area [98] and the existence of bridging and terminal $[S_2]^{2-}$ units [95] in the amorphous material. However, recently, Yeo et al. [99] found that the composition of S species in amorphous MoS_x was changing during HER and in the meantime, Artero et al. [100] observed the loss of terminal $[S_2]^{2-}$ during HER condition also suggesting that MoS_x undergoes structural changes in HER catalysis process. It was concluded from these results that a structural change of the material occurs during the catalytic process. Therefore, to understand the catalytic mechanism and to identify the catalytically active centers of amorphous molybdenum sulfide, detailed studies are still required to investigate this material, in order to further improve its catalytic activity and stability.
In our study, reactive magnetron sputtering using an argon / hydrogen disulfide (Ar/H_2S) atmosphere was used as a fast and effective technique to directly deposit homogeneous molybdenum sulfide films on fluorine-doped tin oxide (FTO) substrates. In addition, this technique allows us to produce molybdenum sulfides of different degrees of crystallinity by simply varying the substrate temperature. Therefore, the relationship between the catalytic property of molybdenum sulfide and its crystallinity was studied by electrochemical measurements and additional characterization methods. Best HER catalytic ability has been achieved from amorphous MoS_x thin films as electrodes, which were sputtered at room temperature. Different sulfur species such as bridging and terminal $[S_2]^{2-}$ units are typical for this material. These units are analogous to those found in crystalline cluster compounds such as $(NH_4)_2Mo_3S_{13}$. [20] It will be described in the following section the identi-

fication of the active centers of amorphous MoS_x and the structural transformation during electrochemical measurements.

4.2 Results and discussions

4.2.1 Structural characterization of MoS_x films sputtered on FTO

The morphology of the molybdenum sulfide films prepared by reactive magnetron sputtering at different substrate temperatures was investigated by SEM. FTO was used as substrate and the deposition time was kept at 5 min. Related figures are shown in Fig. 4.1 with both top view and cross section. When sputtered at RT, uniform and compact films of molybdenum sulfide with a specular and grey optical appearance, and the thickness of 350 nm were formed (see Fig. 4.1A and B). As the sputtering temperature increases to 100 °C, leaf-like flakes begin to grow on the dense amorphous bottom layer as shown in Fig. 4.1C; the film becomes darker and anti-reflecting (see opitcal photographs of molybdenum sulfide sputtered at different temperatures in Appendix A Fig. A.8). When sputtered at temperatures higher than 150 °C, a double-layer structure of molybdenum sulfide film forms, the morphology of which is shown in Fig. 4.1E. The top layer of the molybdenum sulfide is black and porous characterized by upright standing dendritic leaf-like crystallites. When carefully removing the top layer of these films, a silver shining molybdenum sulfide bottom layer appears with metallic luster as known from the mineral molybdenite. The "thickness" of the porous film is about 450 nm according to the cross section SEM in Fig. 4.1F.

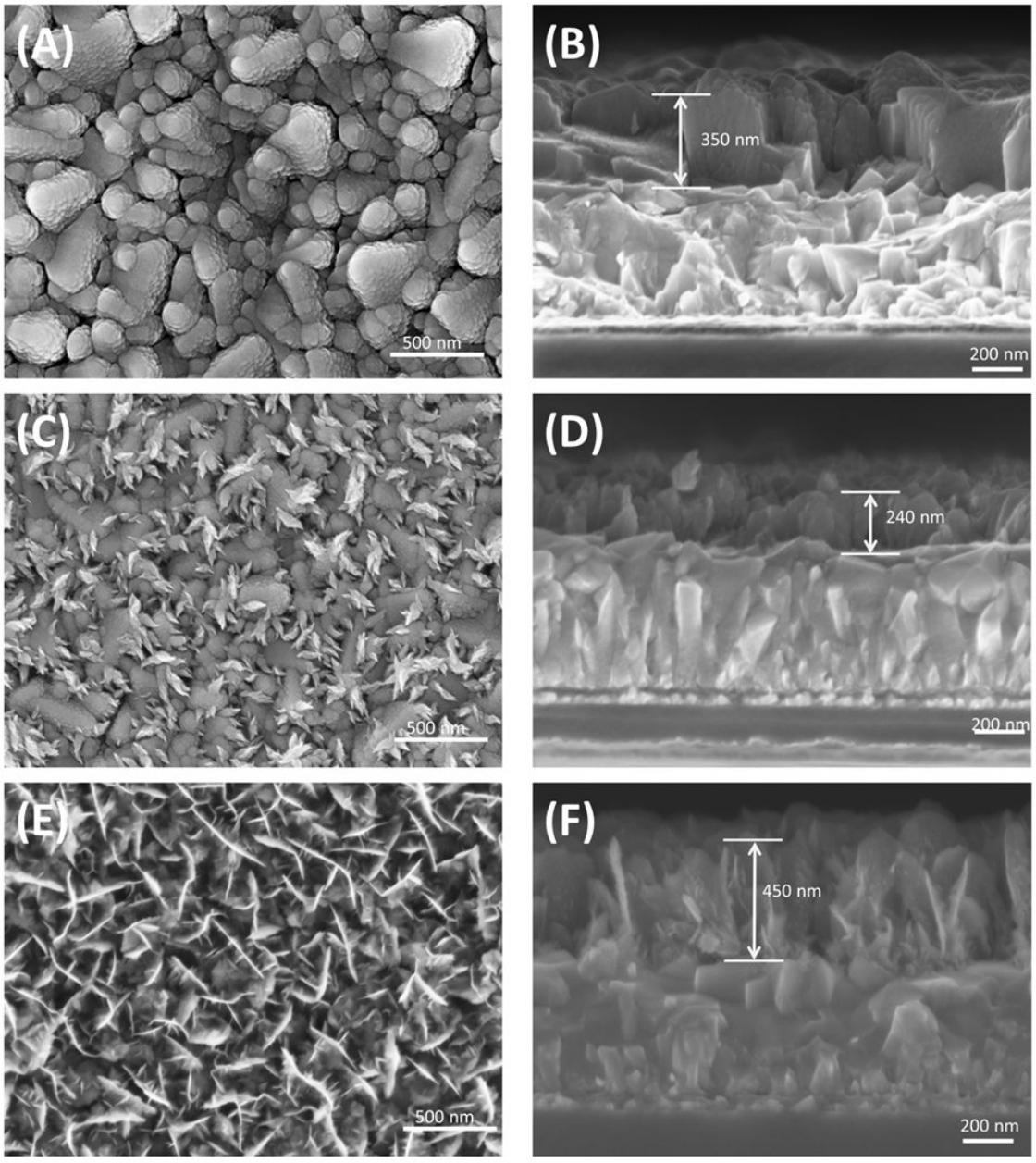

Figure 4.1: *Morphology of MoS_x films deposited at different temperatures: (A),(B) room temperature; (C),(D)* 100 °C*; (E),(F)* 500 °C

X-ray diffractograms of MoS_x films sputtered at different substrate temperatures are shown in Fig. 4.2A. When sputtered at room temperature, only one broad peak at 13.8 ° corresponding to MoS_2 can be observed form the pattern except the peaks from FTO substrate, suggesting that the film is XRD amorphous. As the sputtering temperature increases to temperatures higher than 150 °C, the peak at 13.8 ° becomes more obvious and increases in intensity, indicating improved crystallinity in the material. Other additional diffraction features appear at $2\theta = 33$ ° and 58 °, which stand for the 10.0, and 11.0 planes, respectively, correspond to the

nanoflakes observed at higher substrate temperatures, which can be explained by a (hk.0) texture of 2H-MoS_2 nanocrystals. This interpretation is consistent with the observation that after removal of the porous black top film, the silver shining bottom layer shown in Appendix A Fig. A.8 appears, and the XRD pattern of the bottom layer obtains much more pronounce 00.2 peak at $2\theta = 13.8\,^\circ$ compared to the XRD pattern of the original sample (see Fig. A.9 in Appendix A).

To elucidate the different Mo-S and S-S vibrations in the films, Raman spectra were measured to characterize different molybdenum sulfide samples (see Fig. 4.2B). Films sputtered at 500 °C show vibrational modes (E^1_{2g} mode at 376 cm^{-1} [in-plane Mo-S mode] and an A_{1g} mode at 401 cm^{-1} [out of plane S-S mode]) which are characteristic for layer compounds such as 2H-MoS_2 [134], indicating a crystallized form of MoS_2. However, these characteristic vibration signals for 2H-MoS_2 are relatively small in amorphous molybdenum sulfide films sputtered at RT. However as we can see from the pink curve of RT sputtered MoS_x, both vibrations of terminal $[S_2]^{2-}$ ($\nu(S\text{-}S)_{te}$) at about 510 cm^{-1} and bridging $[S_2]^{2-}$ ($\nu(S\text{-}S)_{br}$) at 542 cm^{-1} can be observed which are typical for $[Mo_3S_{13}]^{2-}$ cluster units [100]. The $[Mo_3S_{13}]^{2-}$ cluster was first described by Kibsgaard et al. [20] in their study in 2014 as a hydrogen evolving catalyst. It is suggested that the presence of $\nu(S\text{-}S)_{te}$ and $\nu(S\text{-}S)_{br}$ in the cluster leads to a higher HER catalytic activity. The two peaks of terminal disulfide units ($\nu(S\text{-}S)_{te}$) and bridging counterparts ($\nu(S\text{-}S)_{br}$) in our RT sputtered MoS_x are less pronounced than in the $(NH_4)_2Mo_3S_{13}$ spectrum (red curve in Fig. 4.2B) because of a high degree of amorphicity of the MoS_x films sputtered at RT: the surrounding environment and the bondings between atoms are less defined than in $(NH_4)_2Mo_3S_{13}$. The spectrum of $(NH_4)_2Mo_3S_{13}$ deposited on FTO is shown by the red curve on Fig.4.2B. The structure of the $[Mo_3S_{13}]^{2-}$ cluster in $(NH_4)_2Mo_3S_{13}$ is depicted in Fig. 4.2C. From the coincidence of the Raman spectra it can be concluded that films deposited by reactive magnetron sputtering at RT have structural similarities with thin films prepared from a $(NH_4)_2Mo_3S_{13}$ solution by spin-coating.

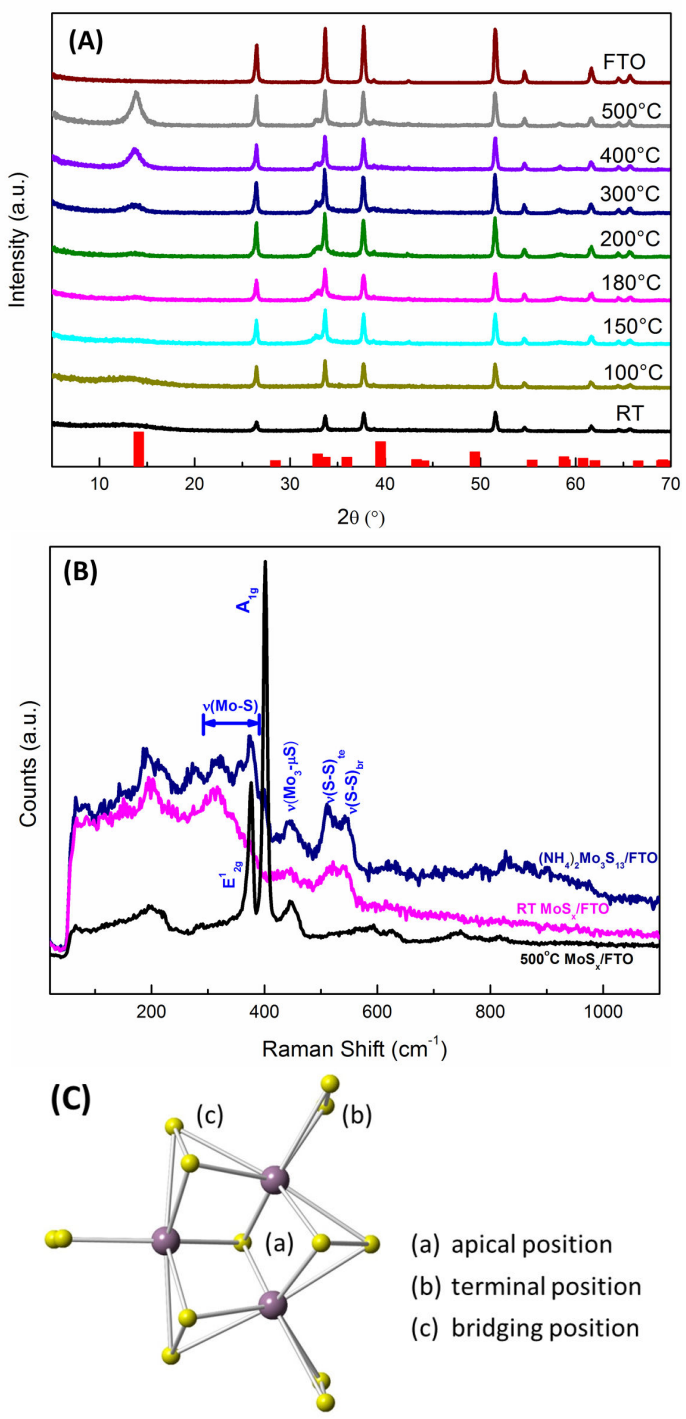

Figure 4.2: *(A) XRD patterns of molybdenum sulfide films sputtered at different substrate temperatures as well as the MoS_2 standard pattern shown by red bars on the bottom, (B) Raman spectra of different molybdenum sulfide films, (C) characteristic structure of a $[Mo_3S_{13}]^{2-}$ cluster unit (purple – molybdenum atoms, yellow – sulfur atoms) showing different sulfur bonds.*

4.2.2 Electrocatalytic performance of MoS_x films sputtered at different temperatures

The catalytic activity of the MoS_x electrodes deposited at different substrate temperatures was electrochemically investigated using cyclic voltammetry (CV) in the voltage range starting from 0.2 V to −0.3 V vs. RHE. Fig. 4.3A shows the result of the voltammetric measurements in the form of line scans. The overpotentials (η) of the electrodes at current densities of $-5\,mA/cm^2$ and $-10\,mA/cm^2$ were taken from these curves and are summarized in Fig. 4.4 along with calculated values of the Tafel slopes after curve fitting. Interestingly, an improvement of current density was noticed during the first 10 min of cycling of amorphous MoS_x electrodes deposited at RT and at 100 °C. But no further improvement was observed after longer electrochemical treatment. This behavior is interpreted as an activation step of the low temperature-deposited HER electrodes. In addition, the electrochemical behavior of un-activated MoS_x electrodes is displayed in Fig. 4.3A as dashed lines which showed higher overpotentials compared to the activated electrodes (see black and red curves in Fig. 4.3A).

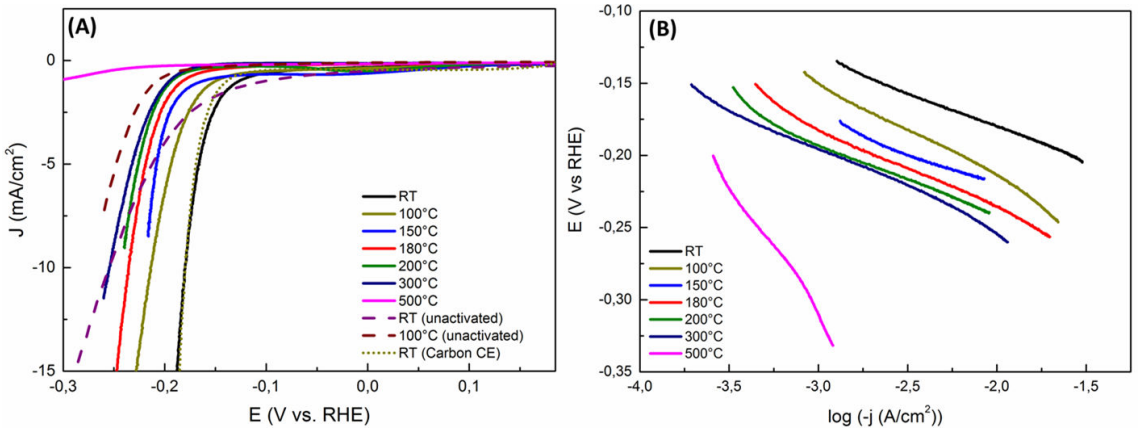

Figure 4.3: *(A) Polarization curves of molybdenum sulfide electrodes sputtered at different temperatures; (B) Tafel plots of the same electrodes deviated from CV measurements*

When using Pt as counter electrode, it has to be taken into account that Pt could be dissolved in the electrolyte, and re-deposited on the surface of the MoS_x electrode and then improve the catalytic ability. Therefore, glassy carbon was also used as counter electrode to rule out this possibility. The dotted line in Fig. 4.3A shows the polarization curve of RT sputtered MoS_x using a carbon CE. The same overpotential (η_{10}=180 mV) has been achieved by using carbon CE comparing to the curve using Pt as CE. Pt 4f XPS spectrum was measured as well after 2 h electrochemical

cycling of the working electrode, but no platinum could be found at the surface of the working electrode (see Appendix Fig. A.10). In addition, a current voltage curve of a bare FTO substrate was measured under the same conditions after cycling the electrode for half an hour. No additional signs for hydrogen evolution could be found (see Appendix Fig. A.11). These measurements prove that FTO itself is not catalytically active for HER and Pt could not be deposited on the MoS_x electrode during cycling.

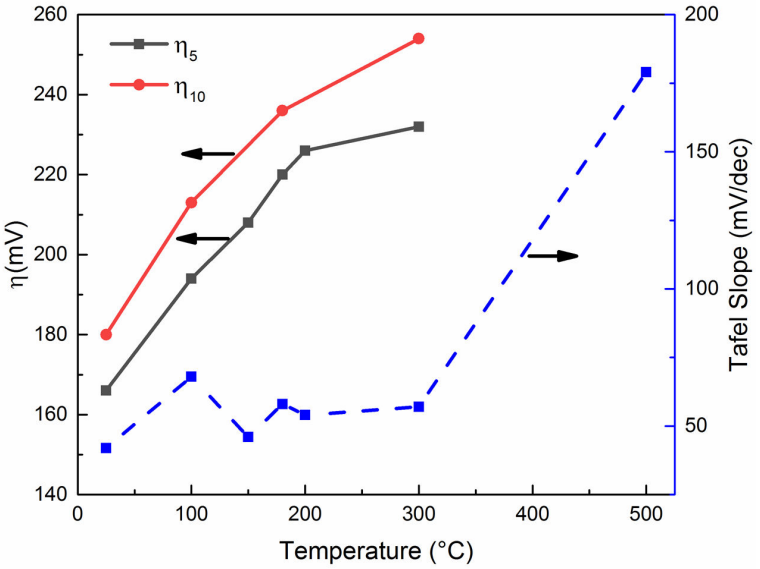

Figure 4.4: *Overpotentials and Tafel slopes of sputtered MoS_x vs. substrate temperatures*

The polarization curves elucidate that the overpotentials increase with increasing deposition temperature, also as shown in Fig. 4.4. Thus, best catalytic performance has been achieved with MoS_x electrodes deposited at room temperature. The overpotential of these electrodes at a current density of $-10\,mA/cm^2$ amounts to 180 mV which is among the highest performances reported for this material.

In crystalline MoS_2, the catalytic property activity is attributed to atoms located at the edge of the S-Mo-S layer units, which is proportional to the number of active sites at these edges. Therefore with growing MoS_2 particle size (see FWHM of the 00.2 peak in XRD patterns in Fig. 4.2A), the overpotential continuously increases correlated by a decreasing number of active sites owing to the growing particle sizes at increasing sputtering temperature. For instance, Fig. 4.5 shows a rough approximation of the edge lengths in the samples deposited at 150 °C and 500 °C for comparison. The total edge lengths of the samples sputtered at 150 °C and 500 °C are 22.1 μm and 14.8 μm, respectively, in an area of 1.41 μm^2. This means

that a sample prepared at 150 °C has more edge sites than a sample prepared at 500 °C. Besides, from XRD patterns of MoS_x deposited at different temperatures, the length (l) of particles and the thickness (d) of the upright standing crystallites can be calculated using the Scherrer equation. Fig.4.6 shows the results of these calculations. The particles in the films grown at temperatures above 300 °C exhibit enlarged basal planes since the l value increases from 10 nm to 23 nm. However, the d value only varies from 6 nm to 6.7 nm at this temperature range. This leads to an overall lowering of the total (01.0) facet area, where the catalytic centers are located, with increasing substrate temperature.

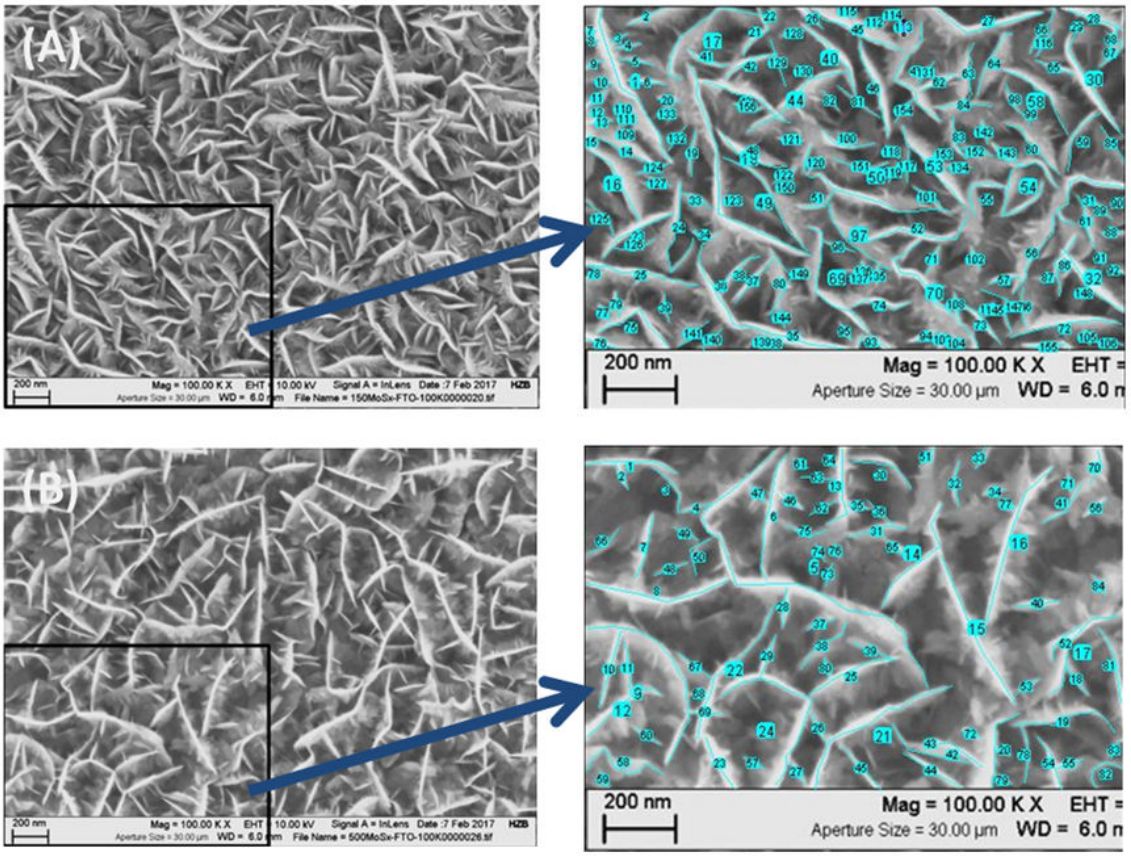

Figure 4.5: *Rough estimation of total edge length of MoS_x sputtered at: (A)* 150 °C*; (B)* 500 °C

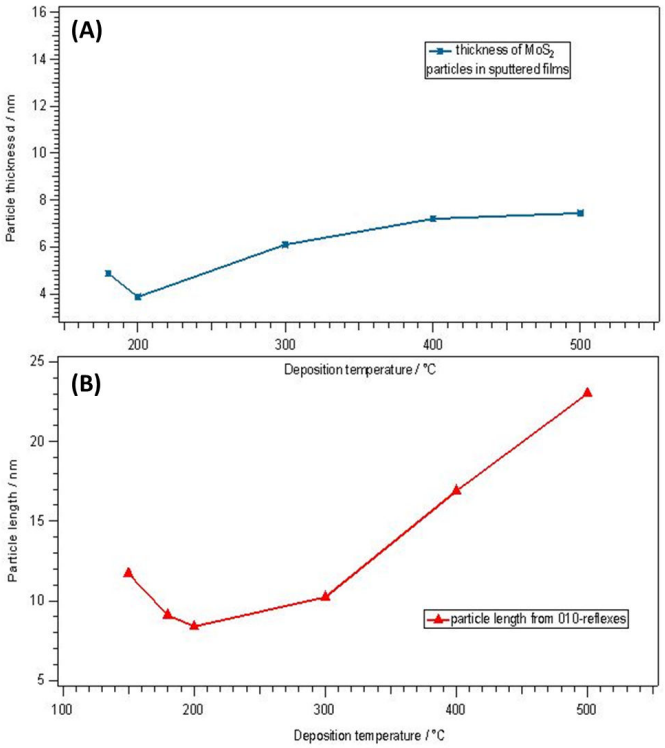

Figure 4.6: *(A) Mean thickness (d) of (00.1) oriented hexagonal platelets in the MoS_2 layers determined from FWHM values of X-ray diffractograms as shown in Fig. 4.2A using the Scherrer equation; (B) Mean length (l) of the facets of 01.0 oriented hexagonal platelets in the layers, determined from FWHM values of X-ray diffractograms shown in Fig. 4.2A using Scherrer equation*

Tafel slopes were determined from E(V) vs. log (-j) Tafel curves (Fig. 4.3B). To explain the changes of the Tafel slopes, fundamental equations of the hydrogen evolution reaction have to be taken into account [135]. These are firstly the proton reduction according to the Volmer step:

$$H^+ + e^- + * \rightarrow H^* \tag{4.1}$$

with b (Tafel slope) = 2.3RT/αF ≈ 120 mV.
Secondly the hydrogen desorption according to the Heyrovsky step:

$$H^+ + e^- + H^* \rightarrow H_2 \tag{4.2}$$

with b = 2.3RT/(1+α)F ≈ 40 mV
Or alternatively according to the Tafel step:

$$2H^* \rightarrow H_2 + 2* \tag{4.3}$$

with b= 2.3RT/2F ≈ 30 mV. In the Eq. 4.1, 4.2, and 4.3, the asterisk * represents an reactive site on the catalyst surface ready to react with hydrogen, R is the ideal

gas constant ($8.314\,JK^{-1}mol^{-1}$), T is the absolute temperature (in Kelvin) and α is related to the barrier symmetry factor, which is about 0.5. [129]
Although the correlation between Tafel slope and HER mechanism was developed for metal surfaces, Tafel analysis can still illustrate the inherent property of the catalyst which is determined by the rate-limiting step during the hydrogen producing process. [98] For instance, Pt has a Tafel slope of 30 mV/dec, which means that hydrogen evolution can be explained by the Volmer-Tafel mechanism whereas the Tafel step (recombination step) is the rate-limiting step. [136]
In our study, MoS_x samples prepared at temperatures ranging from RT to 300 °C have similar Tafel slopes ranging from 40 to 60 mV/dec. It shows that electrodes prepared in this temperature range are subjected to show a similar reaction mechanisms, and the rate limiting step in HER is the hydrogen desorption process. However, when the sputtering temperature is increased to 500 °C, the Tafel slope increases to 179 mV/dec indicating that the rate limiting step can now be explained by the Volmer step. Since the sulfur-dominated basal planes (van der Waals planes) of the hexagonal crystallites are not active as catalytic centers, a possible reason for this change could be that in the sample prepared at 500 °C, only a small number of active surface sites are available, located at the edges of the hexagonal platelets on the so-called non-van-der-Waals planes. These edges appear as white lines belonging to upright standing crystallites in Fig. 4.1E.
The active site number and the intrinsic catalytic property of each active site on the surface of the electrode are two crucial factors that determine the overall performance of a catalyst electrode. In our study, cyclic voltammetry was used to measure the electrochemical capacitance active surface area (ECSA) and to further estimate and compare the number of surface active sites. Firstly in capacitance measurements, the non-faradaic capacitive current of each sample prepared at a specified temperature was measured in the potential range from 0.1 V to 0.31 V vs. RHE because in this potential region no electrochemical reaction has been observed. According to Bard [137], the capacitive current is proportional to the ECSA and the scan rate (υ):

$$i \propto ECSA * \upsilon \tag{4.4}$$

Thus, the ECSA can be estimated from double layer capacitance (C_{dl}) measurements obtained by CV. [138] In our study, these measurements were done at different scan rates ranging from 10 mV/s to 160 mV/s to study the ECSA and the results are shown in Fig. 4.7.

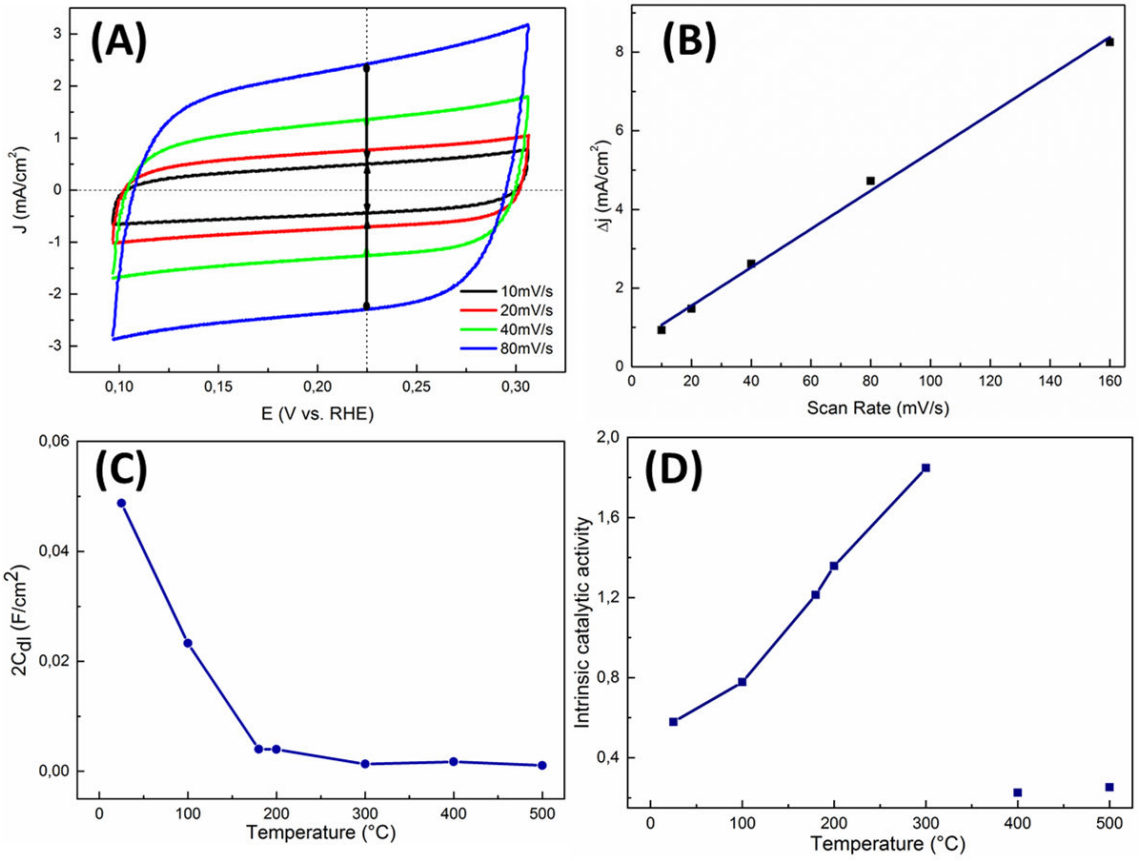

Figure 4.7: *(A) CV of RT sputtered MoS_x measured at different scan rate after activation; (B) Δj vs. scan rate; (C) $2C_{dl}$ vs. sputtering temperature; (D) intrinsic catalytic ability (current density of the electrodes at $-200mV$ vs. RHE divided by $2C_{dl}$ vs. sputtering temperature*

For example, the CV curves of the RT sputtered MoS_x electrode is shown in Fig. 4.7A. The difference between anodic and cathodic current density (Δj) at 0.225 V vs. RHE as a function of scan rate is displayed in Fig.4.7B. The slope of Δj vs. scan rate is equal to $2C_{dl}$. [138] Fig. 4.7C shows the $2C_{dl}$ capacitance as a function of sputtering temperature. The ECSA on different electrodes is proportional to this value which decreases with increasing sputtering temperature. Therefore, it can be concluded that activated RT sputtered MoS_x has a much higher ECSA value, but as soon as the leaf-like nanoflakes begin to grow on the electrode surface the ECSA decreases dramatically and becomes constant when the nanoflakes cover the whole surface.

In Fig. 4.7D, the y-axis shows the value of current density of the electrode at -0.2 V vs. RHE divided by $2C_{dl}$, indicating the intrinsic catalytic property of each electrode per ECSA. As shown in Fig. 4.7D, the intrinsic catalytic property of the electrode is increasing with sputtering temperature until 300 °C. However, when applying a deposition temperature higher than 300 °C, the catalytic property decreases dramat-

ically. It has been shown by XRD that the crystallinity of the molybdenum sulfide increases with increasing sputtering temperature. Therefore, it can be expected that the catalytic activity also increases with crystallinity. The decay of the intrinsic catalytic activity at electrodes deposited at temperature higher than 300 °C can be explained by the high overpotential ($\gg$300 mV) of the electrode since the calculations of the intrinsic catalytic activity were done at −0.2 V vs. RHE. (see Fig. 4.3A).

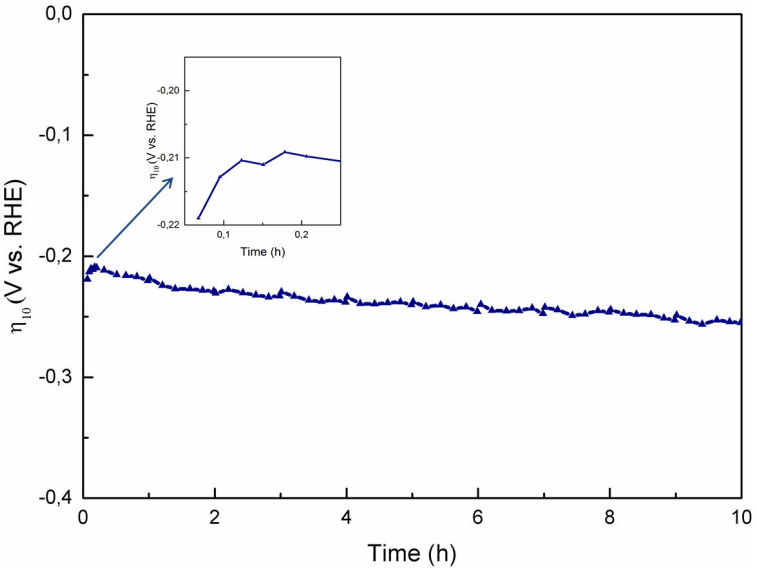

Figure 4.8: *Overpotential (η_{10}) of RT sputtered MoS_x vs. time*

Besides high ECSA and high activity, long term stability is an essential issue for all catalysts. Therefore, a stability test of the RT sputtered MoS_x electrode was performed by CV in the potential range from 0.2 V to −0.3 V vs. RHE applying a scan rate of 10 mV/s in the time frame of ten hours monitoring the change of overvoltage at a current density of $-10\,mA/cm^2$. Fig. 4.8 shows the result of the stability test, which was not iR corrected. In the beginning of the measurement, the overpotential (η_{10}) first decreased from 0.219 V to 0.209 V which corresponds to an activation step of the electrode which was mentioned above (see also inset in Fig. 4.8). Afterwards, the overpotential becomes stable, but increases slowly with time. At the end of the test, the overpotential amounted to −0.255 V. This value indicates an increase in overpotential at 10 $mAcm^{-2}$ of about 4.6 mV/h under the condition of a continuous cycling of the electrode.

There are some possible reasons for the drop of catalytic ability. Fig. A.12 in Appendix A shows the amorphous MoS_x electrode after electrochemical cycling for 10 min where the thickness of the sample has already decreased from originally 350 nm to 260 nm. Therefore, one possible explanation could be the loss of material

due to corrosion or H_2 bubble formation during the electrochemical measurement. Another reason could be the exposure of the FTO substrate to the electrolyte due to crack formation, leads to a decrease of catalytic performance as shown by the top view morphology of RT MoS_x electrode in Fig.A.13.

4.2.3 Electrochemical activation of RT sputtered MoS_x

DEMS measurements

Fig. 4.9A shows the first three CV scans of a typical RT sputtered MoS_x electrode using glassy carbon CE without iR correction. The current density of the electrode at $-0.3\,V$ increases from $12\,mAcm^{-2}$ to $16\,mAcm^{-2}$, which means that the catalytical activity of the electrode is significantly improved during the first three cycles. In subsequent cycles, the current density could not further be improved.

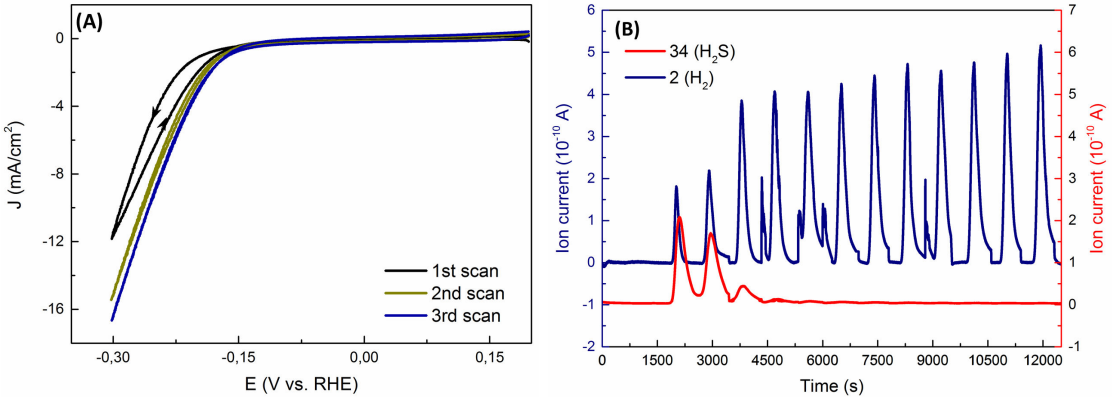

Figure 4.9: *(A). First three CV scans; (B)DEMS measurement of RT sputtered MoS_x with glassy carbon CE*

To study this activation process, gas evolution at the electrode was investigated by DEMS as a function of time. The result is shown in Fig. 4.9B. The signals of H_2^+ (mass/charge (m/q)=2) and H_2S^+ (m/q=34), respectively, were monitored while cycling the electrode in a potential range from $0.2\,V$ to $-0.3\,V$ vs. RHE with a scan rate of $1\,mV/s$. There are spikes in the H_2 signal for example at $4350\,s$, $5380\,s$ and $8790\,s$. They are caused by the release of hydrogen bubbles which accumulated at the surface. In addition, steps occur at the end of each CV cycle. The reason for these steps is that the electrolyte is saturated with H_2 after each CV cycle. And when refreshing the electrolyte after each CV cycle, the H_2 concentration suddenly drops and the signal of H_2 shows a step.

In the first three scans of the DEMS measurement, the H_2S^+ signal is relatively high, but decreases gradually and disappears by the end of the measurement. The result suggests that the activation process of RT sputtered MoS_x is accompanied by a release of sulfur in the material. The activation in the DEMS measurement takes longer than in CV measured in Fig.4.3 owing to ∼10 times lower current because of the high resistance of the DEMS cell.

X-ray photoelectron spectroscopy

To investigate the RT deposited amorphous MoS_x film and to study in detail its chemical changes before and after electrochemical treatment, XPS was employed to characterize the RT sputtered MoS_x electrode at three different stages: the as-prepared electrode, and the electrode that has been treated under CV condition for 10 min and 2 h. The results are shown in Fig. 4.10.

Figs. 4.10A and 4.10B show the XPS spectra of Mo 3d and S 2s of the as-prepared MoS_x film before electrochemical treatment. The Mo : S ratio calculated from the spectra equals 1 : 3.97, which suggests the presence of Mo_3S_{12} and/or Mo_3S_{13} entities. The peak positions of the Mo 3d 5/2 and 3d 3/2 at 229.1 eV and 232.2 eV, respectively, are fitting to Mo in the oxidation state 4+. From the S 2p spectra of the as-prepared MoS_x, it can be concluded that different sulfur ligands are bonded to molybdenum, as known from the Mo_3S_{13} cluster. According to work published by Weber et al., [139, 140] the sulfur ligands with a S 2p 3/2 peak at 161.8 eV can be assigned to terminal S_2^{2-} units and the sulfur peak at 162.9 eV to bridging sulfur. This result agrees well with the above discussed Raman spectra (Fig. 4.2B, pink curve) of amorphous MoS_x. In our measurements, a third sulfur peak was found located at 163.1 eV. This feature indicates the presence of a further sulfur species in the amorphous MoS_x layers which could be addressed to the shared S_2^{2-} at the terminal position connecting Mo_3S_{13} and/or Mo_3S_{12} units.

Fig. 4.10C and 4.10D show the related XPS spectra after 10 min CV. The Mo : S ratio now amounts to 1 : 1.89, indicating that a significant fraction of the sulfur atoms at the surface were released during electrochemical cycling. This is consistent with the release of sulfur in the form of H_2S that we observed in the DEMS results (see Fig. 4.9). From the fitted curve of XPS S 2p signal in Fig. 4.10D, we see a significant decrease of bridging S_2^{2-} signal and of the third sulfur species in the cluster units. In addition, the peak position of Mo^{4+} 3d 5/2 was shifted from 229.1 eV to 229.3 eV. On the other hand, the cyan curve with 3d 5/2 peak at about 232.5 eV in

Fig. 4.10C indicates the presence of Mo^{6+} in the layer after electrochemical treatment. The appearance of molybdenum in the oxidation state 6+ can be explained by the oxidation of the electrode surface exposed to air during the transferring from electrochmeical cell to the XPS chamber after the removal from the electrolyte.

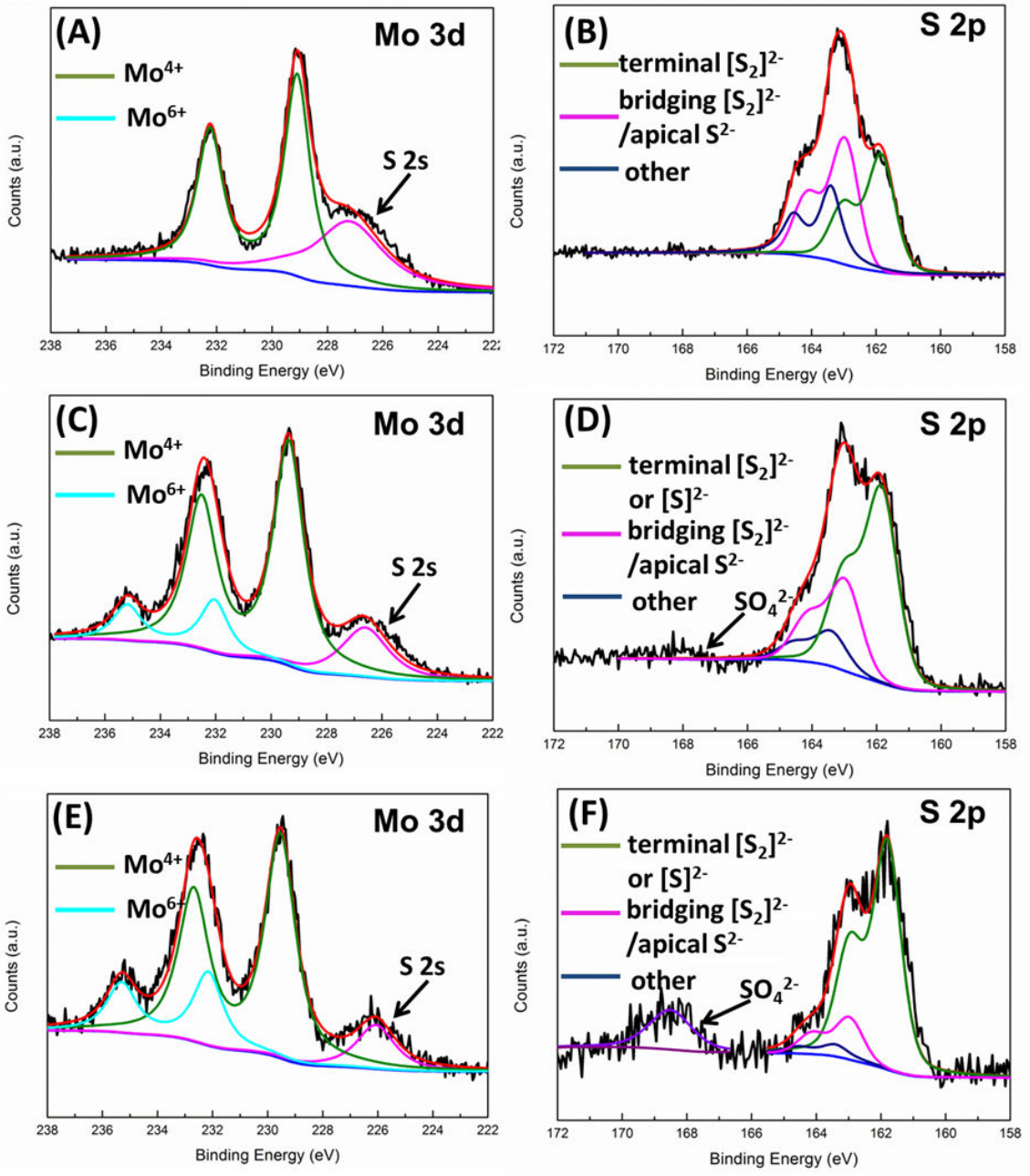

Figure 4.10: *XPS of Mo 3d, S 2s and S 2p: (A),(B) from as-prepared RT sputtered MoS_x; (C),(D) from MoS_x cycled for* 10 min*; (E),(F) from MoS_x cycled for* 2 h*. Raw curve (black), fitted curve (red), background (blue).*

As we can see from the XPS spectra of MoS_x after two hours CV scanning (see Fig. 4.10E and 4.10F), the Mo:S ratio increases further to 1 : 1.35. The Mo 3d

5/2 peak shifts to 229.5 eV, and most of the remaining sulfur is addressed to sulfur ligands with binding energy of 161.9 eV. Similar XPS results were also obtained by Benck et al. [95] and Catalongue et al. [141] in 2014 using in-line XPS.
From these results one possible explanation would be that the terminal S_2^{2-} ligand is the most stable ligand in the amorphous material after two hours of measurement. However, the dramatic loss of exclusively bridging sulfur should lead to a total disintegration of the $Mo_3S_{13}^{2-}$ clusters at the catalyst-electrolyte interface. Studying amorphous MoS_3, crystalline MoS_2 and $(NH_4)_2Mo_3S_{13}$ by XPS, Weber et al. [141] found that the S^{2-} atoms in hexagonal MoS_2 have the same binding energy as terminal S_2^{2-} ligands in $(NH_4)_2Mo_3S_{13}$. Therefore, our XPS results can be explained under the assumption that RT sputtered MoS_x transforms from an amorphous polymer chain structure consisting of Mo_3S_{13} and Mo_3S_{12} clusters to MoS_2 nano-islands.

In-situ / in-line Raman measurements

As proposed by Tran et al., [100] the S_2^{2-} ligands of the Mo_3S_{13} cluster are reduced and partly eliminated under potential bias in accordance with our DEMS experiment where H_2S evolution was observed (see Fig. 4.9B). Loss of terminal S_2^{2-} groups under H_2S formation coincides with our *in–situ* and in-line Raman measurements (Fig. 4.11) and DFT calculations of Mo_3S_{13} in Chapter 3 where a strong affinity of protons to react with terminal sulfur was found.
In this *in-situ*/in-line Raman measurement, the spectrum of the sample was firstly measured in an *in-situ* cell (see scheme in Fig. 2.9) through a quartz window without electrolyte before applying a potential (blue curve in Fig. 4.11A). After CV, the *in-situ* chamber was flushed with deionized water and then dried by nitrogen gas to prevent oxidation. As shown by the red curve in Fig. 4.11A after the electrochemical treatment, the vibration modes of terminal and bridging S_2^{2-} units almost disappeared. However, at a Raman shift of 404 cm^{-1}, a new vibration mode emerged which can be assigned to the A_{1g} mode from the layer structured MoS_2. Fig. 4.11B shows the *in-situ* Raman results in the presence of electrolyte. As we can see from all three curves, additional peaks appears in the range between 850 cm^{-1} to 1100 cm^{-1}. These are vibration modes from the sulfuric acid electrolyte. Despite these additional peaks, vibration modes from bridging and terminal S_2^{2-} can still be observed from the as-prepared sample before cycling. During the second cycle, the peaks from both bridging and terminal S_2^{2-} are becoming weaker than as prepared sample. After 10 cycles, these two peaks have nearly disappeared. How-

ever, the A_{1g} peak starts to emerge which is consistent with the in-line Raman result.

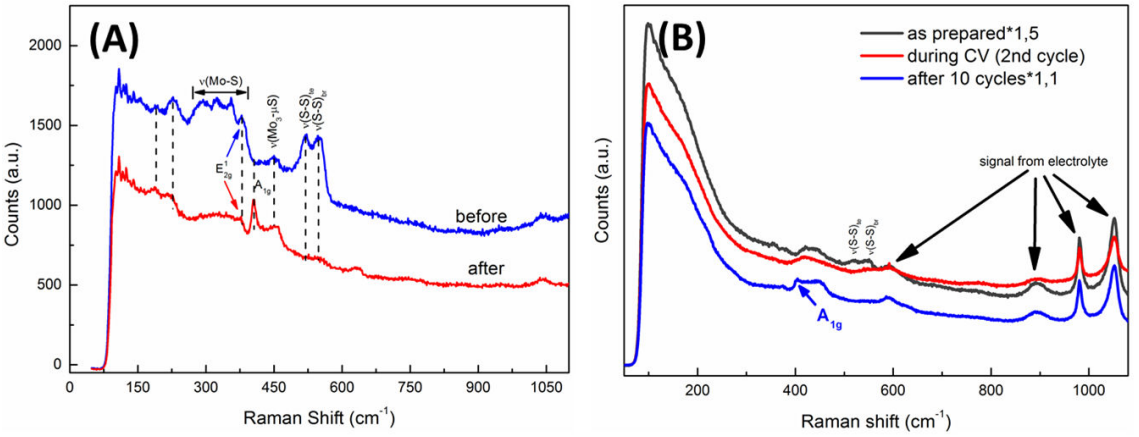

Figure 4.11: *(A) In-line Raman of MoS_x before (blue curve) and after (red curve) electrochemical activation (cycling from* $-0.6\,\mathrm{V}$ *to* $-2.1\,\mathrm{V}$ *vs. Pt CE); (B) in-situ Raman of MoS_x during cycling*

This fact suggests a structural change from interlinked Mo_3S_{13} and Mo_3S_{12} moieties to MoS_2 nano-islands. The transformation is in addition leading to an improvement of the catalytic property after 10 min cycling of the electrode (see the improvement of current density and $H_2{}^+$ signal in Fig. 4.9). A new feature at about $900\,\mathrm{cm}^{-1}$ is observed from the Raman spectra of activated amorphous MoS_x after exposing it in air which corresponds to MoO_3 formation (shown in Fig. A.14, Appendix A). This result also explains the presence of MoO_3 in the XPS spectra of measured samples.

Cross-section TEM

In literature, Li et al. [142] studied the activation of amorphous MoS_3 HER catalyst after electrochemical cycling. The authors came to the conclusion that using high resolution transmission electron microscopy (HRTEM) and electron energy loss spectroscopy (EELS) that the material partially crystallized but their results suggest that the amorphous molybdenum sulfide is the catalytic active phase while the crystalline phase rather contributes to a catalyst deactivation.

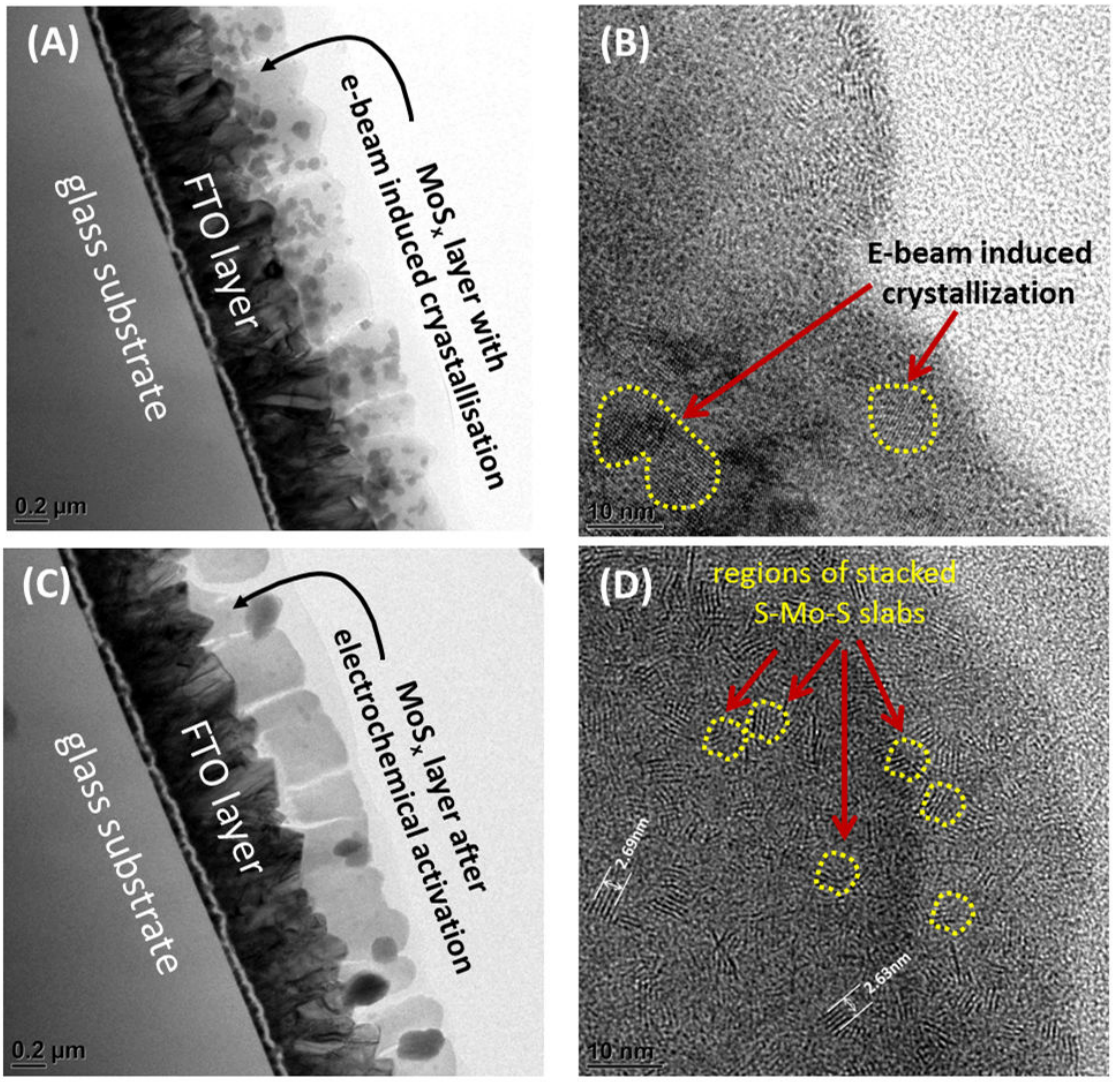

Figure 4.12: *Cross-section HRTEM of amorphous MoS_x: (A) and (B): as-prepared MoS_x, dark areas indicate e-beam crystallization of the MoS_x layer during TEM measurement; (C) and (D) MoS_x after electrochemical activation consisting of small particles with stacking S-Mo-S slabs, typical for 2H-MoS_2.*

With respect to the formation of stacked S-Mo-S slabs after electrochemical activation, we tried to visualize its presence by cross-section TEM as well. Fig. 4.12 shows TEM figures of amorphous MoS_x before and after electrochemical activation. Fig. 4.12A and B show the results of as-prepared sample. We noticed that as soon as the electron beam was directed to pristine sample, a crystallization process became visible as growing dark regions in the amorphous and transparent matrix. At higher magnification, crystallized regions up to 10 nm size were found with the layer distance of about 4.5 Å (Fig. 4.12B) which could be explained by the crystallization of sulfur polymorphs. In the sample after electrochemical activation, the electron beam induced crystallisation was not observed. In the activated sample, crystallized

sections with two to eight stacked S-Mo-S layers can be observed at higher magnification as shown in Fig. 4.12D. The distances between the slabs were evaluated from five stacked layers from different islands. A mean distance of 6.7 Å was evaluated which is very close to the value of 6.6 Å reported by Jaramillo et al. that corresponds to 2H-MoS_2. [17]

4.2.4 Phase transformation during electrochemical activation

A mechanism to explain the reaction of protons at the edges of polymerized chains of Mo_3S_{12} and Mo_3S_{13} clusters under formation of H_2S gas molecules is shown in Fig. 4.13.

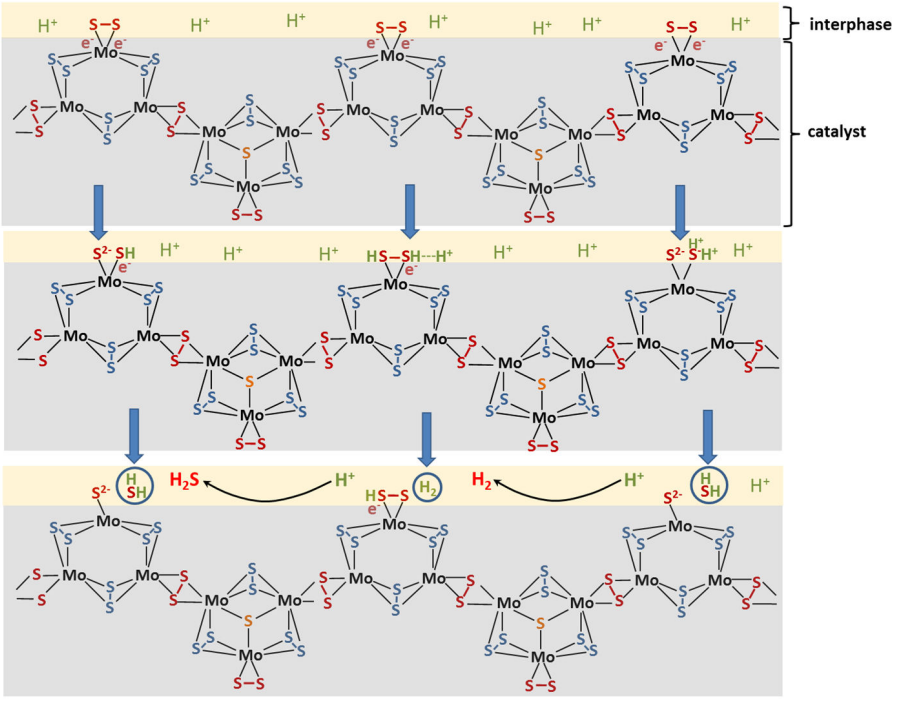

Figure 4.13: *Structural transformation process of RT sputtered MoS_x consisting of polymerized Mo_3S_{13} and Mo_3S_{12} units*

It is assumed that under electrochemical conditions the S_2^{2-} units, being present in polymerized Mo_3S_{13} and Mo_3S_{12} clusters, are reduced to S^{2-} when reacting with electrons under cathodic polarization. The reaction of electrons and protons with S_2^{2-} moieties is leading to the formation of H_2S gas molecules which will be released from the electrode surface. This transformation can be formulated by the equations:

$$Mo_3([S_2])_6 + 12H^+ + 12e^- \rightarrow Mo_3(S)_6 + 6H_2S \tag{4.5}$$

$$Mo_3(S)_6 + 4H^+ + 4e^- \rightarrow Mo_3([S]_4\square_2) + 2H_2S \tag{4.6}$$

The formation of MoS_2 islands after sulfur loss is illustrated in Fig. 4.14. Here MoS_2 fragments are considered to be formed including sulfur defects at the edges of nano-size S-Mo-S islands (see Fig. 4.12). Therefore, the presence of charged and activated sulfur defects is possibly leading to molybdenum hydride moieties in electrolyte under cathodic potential, as also proposed by Tran et al. [100]

In our model, the catalytic centers in nano-sized sulfur-defective MoS_{2-x} islands are similar to those in larger MoS_2 particles with dangling bonds, i.e. coordinatively unsaturated bonds, are thought to be the active centers. *In-situ* Raman spectra show that the terminal sulfur species are the first ones to be removed under electrochemical cycling (see Fig. 4.11). From this we conclude that $[S_2]^{2-}$ ligands are reduced to S^{2-} and/or eliminated as H_2S under turnover conditions.

The disappearance of terminal $[S_2]^{2-}$ and the reduction of bridging $[S_2]^{2-}$ to two S^{2-} is leading to unsaturated Mo^{4+} atoms at the edges of S-Mo-S layers. The loss of sulfur at the edges by the release of H_2S can be expressed by the Eq. 4.7 and 4.8:

$$MoS_2 + 2e^- + 2H^+ \rightarrow Mo[HS]_2 \tag{4.7}$$

$$MoS_2 + 2e^- + 2H^+ \rightarrow Mo-(S-\square) + H_2S \tag{4.8}$$

$$Mo[HS]_2 \rightarrow MoS_2 + H_2 \tag{4.9}$$

In Fig. 4.13, these reactions are displayed in three levels: in a first step terminal S_2^{2-} units (see top of Fig. 4.13) are reduced to two S^{2-} ligands (middle part of Fig. 4.13) whereas one of these reduced terminal sulfur atoms is immediately reacting with two H^+ ions under formation of H_2S (Eq. 4.8). It is also possible that one $[HS\text{-}HS]^{2-}$ unit formed in Eq.4.7 reacts under reduced conditions, forming H_2 and S_2^{2-} (see Eq.4.9). After MoS_2 fragments have formed, the release of H_2S stops mostly. A possible mechanism is described in Eq. 4.10, Eq. 4.11, Eq. 4.12:

$$Mo-(S-\square) + e^- + H^+ \rightarrow Mo-(S-H^*) \tag{4.10}$$

$$Mo-(S-H^*) + e^- + H^+ \rightarrow Mo-(S-\square) + H_2 \tag{4.11}$$

$$2Mo-(S-H^*) \rightarrow 2Mo-(S-\square) + H_2 \tag{4.12}$$

An unsaturated molybdenum bond at the edge of a nano-island reacts with a proton from the electrolyte and an electron from the cathode at the electrode/electrolyte interface to a Mo-H^* unit (see Eq. 4.10). In a next step, Mo-H^* reacts with a second proton and a second electron resulting in the formation of an H_2 gas molecule (see Eq. 4.11). This reaction mechanism is illustrated in Fig. 4.14 in three steps (a): reaction of a negatively charged unsaturated bond of Mo, (b) reaction with a proton

and formation of Mo-H* and (c) reaction of Mo-H* with a further proton and as second electron with H_2 evolution.

The transformation of amorphous MoS_x to MoS_2 is supported by results described by Casalongue et al. [141] presenting DFT calculations which model the edge structure of MoS_{2-x}. They propose that the edges are terminated by S monomers, which are depicted in our model as Mo atoms adjacent to a sulfur vacancy (see Fig. 4.14).

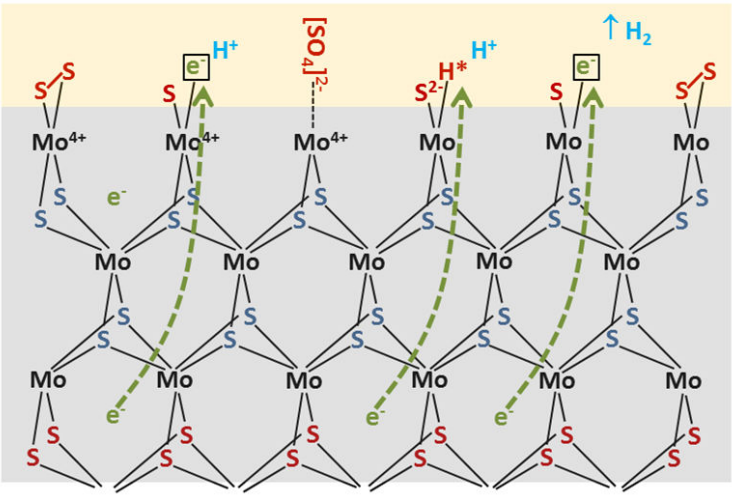

Figure 4.14: *Structure of RT sputtered MoS_x after activation: MoS_2 nano-island*

To summarize, during electrochemical cycling in the voltage range from 0.2 V to −0.3 V vs. RHE, the chain structure (Fig. 4.13) transforms continuously into a MoS_2 layer-type structure (see Fig. 4.14) under the release of H_2S. Gray areas in Fig. 4.13 are representing polymerized chains of Mo_3S_{12} and Mo_3S_{13} units, while yellow areas show the acidic electrolyte in contact with MoS_x. At the interface, S_2^{2-} units will be reduced and react under cathodic conditions with protons. Finally, H_2S and H_2 gas molecules will be released from the MoS_x chains as shown in the lower part in Fig. 4.13.

The presented model is supported by the fact that the cathode layer reacts with oxygen quickly under formation of Mo^{6+} after exposure to an ambient atmosphere since the edge Mo atoms with dangling bonds should be easily oxidized in air rather than Mo atoms bonded to sulfur atoms. The Mo^{4+}: Mo^{6+} ratio calculated from XPS results is given in Table. 4.1. Assuming that all oxidized Mo atoms are located at the edges of S-Mo-S units, the size of the MoS_{2-x} nano-islands can be approximately estimated from the ratio of Mo^{6+}/Mo^{4+}.

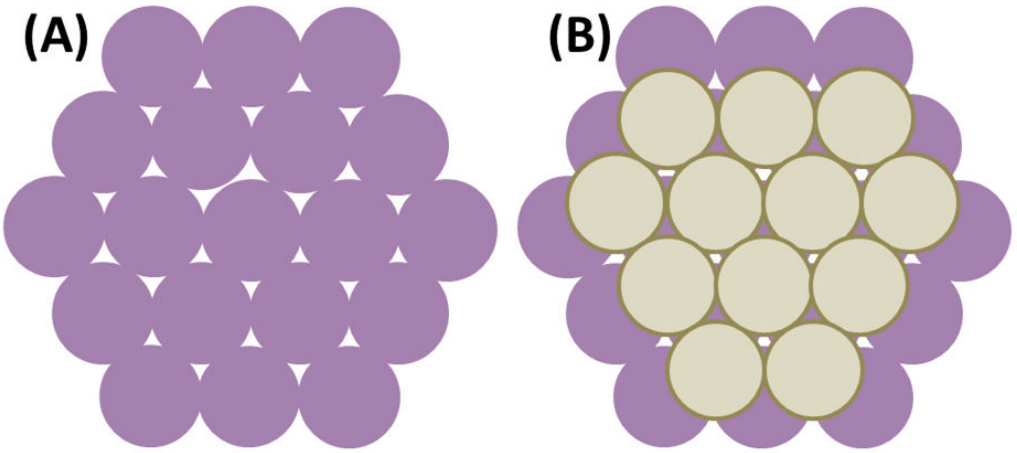

Figure 4.15: *Top-view scheme of: (A) a close packed Mo monolayer; (B) Mo layer sandwiched by two S layers forming hexagonal MoS_2 nano-islands*

For instance, Fig. 4.15A shows a close packed Mo monolayer with the shape of a regular hexagon while Fig. 4.15B shows the top-view scheme of a Mo layer sandwiched by two S layers. Assuming that the number of Mo atom on one edge is n, then in one nano-island with a hexagon Mo layer, the number of edge Mo atoms will be:

$$N_{\text{edge}} = 6n - 6 \tag{4.13}$$

The overall number of the Mo atoms is:

$$N_{\text{all}} = 3n^2 - 3n + 1 \tag{4.14}$$

Therefore, the inside Mo atoms number would be:

$$N_{\text{inside}} = N_{\text{all}} - N_{\text{edge}} = 3n^2 - 9n + 7 \tag{4.15}$$

On the other hand, the number of S atoms in this island can be written as:

$$N_{\text{S}} = 2 * (N_{\text{all}} - 3 * n + 2) = 6n^2 - 12n + 6 \tag{4.16}$$

Based on the assumption that only the edge Mo atoms that are not saturated with S atoms can be oxidized after exposure in air, then the ratio of Mo^{6+} to Mo^{4+} could be written as:

$$Mo^{6+} : Mo^{4+} = N_{\text{edge}} : N_{\text{inside}} \tag{4.17}$$

After 10 min of cycling, the ratio between Mo^{6+} with Mo^{4+} is 1:4.56 which gives an n value of around 11 corresponding to a nano-island size of about 931 atoms (331 Mo atoms and 600 S atoms). After 2 h, the ratio of Mo^{6+} to Mo^{4+} changed

to 1:3.14. The calculated n value is around 8, then the catalyst nano-islands with a mean of size of 363 atoms (169 Mo atoms and 294 S atoms) could be present. These considerations support the interpretation that the size of the MoS_{2-x} decreases during the electrochemical measurement. In the meantime, the small size of the MoS_{2-x} nano-islands after structural transformation can explain the high ECSA and the low overpotential of the activated MoS_x electrode.

Table 4.1: *Peak positions of Mo 3d and S 2p XPS features and deviated ratios from XPS*

MoS_x electrodes	Mo $3d_{5/2}$	Mo $3d_{3/2}$	S 2s	S_t	$S_{br/ap}$	S_{other}	Mo/S ratio	Mo^{6+}/ Mo^{4+}
as-prepared	229.1	232.3	227.2	161.9	163.0	163.5	1:3.97	—
after 10 min CV	229.3	232.5	226.8	161.9	163.0	163.5	1:1.84	1:4.56
after 2 h CV	229.5	232.7	226.1	161.9	163.0	163.5	1:1.37	1:3.14

4.3 Conclusion

Molybdenum sulfide layers have been deposited on FTO substrates by reactive magnetron sputtering using an Ar/H_2S gas atmosphere. As a function of substrate temperature, the sputtered layers exhibited an increasing degree of crystallinity with increasing temperature ranging from room temperature to 500 °C. The relationship between crystallinity and catalytic property with respect to hydrogen evolution was studied electrochemically. Best performance was achieved from amorphous MoS_x films sputtered at room temperature after an activation process, showing an overpotential of 180 mV at a current density of $-10\,mA/cm^2$. The stability of the electrodes was tested for 10 h. The production of hydrogen was demonstrated by DEMS. Combining results from Raman and XPS measurements, the presence of bridging and terminal S_2^{2-} are characteristic for the amorphous MoS_x layers. However, the catalytic activity is no longer exclusively owing to the presence of $[Mo_3S_{13}]^{2-}$ clusters as known from crystalline $(NH_4)_2Mo_3S_{13}$, but due to the formation of MoS_2 nano-island exhibiting a high number of sulfur vacancies at the edges of the S-Mo-S layers. We have assigned the active center to be the Mo atoms with dangling bonds which are located at the edges. These are expected to react with protons and form Mo-H^*

intermediates. These results pose the question how the catalytically active center found can further be improved, also under the aspect of long term stability.

Chapter 5

Sputtered molybdenum sulfide as possible catalyst candidate for CO_2 reduction reaction

Molybdenum sulfide, a well known catalyst for hydrogen evolution reaction (HER), has also the promising potential as catalyst for CO_2 reduction reaction (CO_2RR). In this chapter, molybdenum sulfide films prepared by reactive magnetron sputtering at different temperatures on gas diffusion electrode (GDE), were tested for their catalytic activity for CO_2 reduction. Combining electrochemical measurements with the analysis of CO_2 reduction products, the catalytic properties of sputtered molybdenum sulfide films for CO_2RR were evaluated.

5.1 Introduction

As discussed in Chapter 1, the electro-catalysis for CO_2RR remains challenging and MoS_2 could be a possible candidate as a CO_2RR catalyst according to theoretical calculations. [79] However, there are only few publications of MoS_2 as CO_2RR catalyst and the catalytic mechanism remains still unknown.
Therefore in our study, MoS_2 films were prepared by reactive magnetron sputtering at different temperatures and the CO_2RR products were studied by mass spectrometry (MS), headspace gas chromatography (HS-GC), and high performance liquid chromatography (HPLC). RT sputtered amorphous layers and the layers prepared at 470 °C were chosen as examples in this chapter, investigating the catalytic activity of amorphous and crystallized molybdenum sulfide for CO_2RR. Both samples obtained high current densities during electrochemical measurements. However, according to the analysis of MS, GC and HPLC results, only low amounts of formaldehyde, methanol and ethanol could be detected because most of the current was attributed to hydrogen production. These results suggest that both amorphous MoS_x and crystallized MoS_2 is more catalytically active for HER than for CO_2RR.

5.2 Results and discussions

5.2.1 Structural characterization of sputtered molybdenum sulfide

Fig. 5.1 shows the morphology of molybdenum sulfide films sputtered at different temperatures on gas diffusion electrode (GDE) substrates. The samples show relatively similar morphologies than those obtained on FTO substrates shown in Fig. 4.1 in Chapter 4. RT sputtered MoS_x has a more compact structure (see Fig. 5.1A) while MoS_2 sputtered at 470 °C in Fig. 5.1B shows a flake-like morphology. The morphology of a bare GDE substrate consisting of hydrophobic micro-porous carbon layer and macro-porous carbon layer are also shown in Fig. 5.1C.

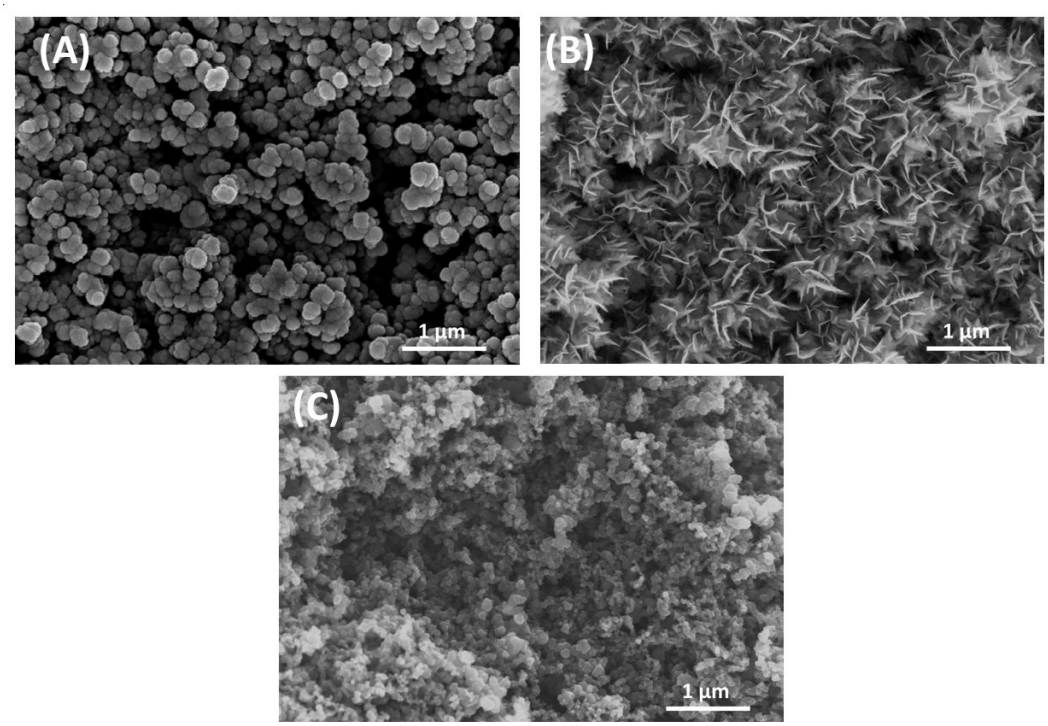

Figure 5.1: *Top-view morphology of: (A) RT sputtered molybdenum sulfide on GDE; (B) molybdenum sulfide sputtered at* 470 °C *on GDE; (C) bare GDE*

The XRD patterns of the samples deposited at different temperatures are shown in Fig. 5.2 along with the pattern of a blank GDE substrate shown by the black color and the standard 2H-MoS_2 XRD pattern shown by the red bar chart on the bottom.

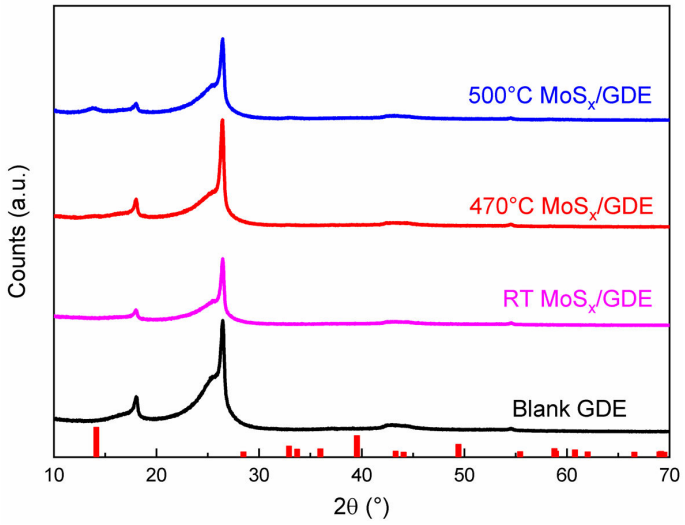

Figure 5.2: *XRD patterns of molybdenum sulfide films sputtered on GDE at different temperatures*

It can be observed from the figure that blank GDE has characteristic peaks at about 17 ° and in the range from 24 ° to 27 ° which are also present in the patterns of all

molybdenum sulfide samples deposited on GDE substrates. Due to the relatively high diffraction signals from the substrates, only a small peak at 14 °, which corresponds to 2H-MoS_2, is visible in the XRD pattern of the sample deposited at 500 °C. From Chapter 4, it is known that the crystallinity of the sputtered molybdenum sulfide on FTO is increasing with increasing substrate temperature and RT sputtered MoS_x is XRD amorphous. Therefore, from the similar morphology observed in SEM figures, it can be speculated from the XRD patterns that MoS_x deposited on GDE at RT is XRD amorphous and the sputtered molybdenum sulfide films become more crystallized in the form of 2H-MoS_2 as the substrate temperature increases.

5.2.2 Catalytic ability of magnetron sputtered MoS_2 for CO_2RR

Quantify the gaseous products in electrochemical measurements

As shown by Fig. 2.4 in Chapter 2, the gaseous products during electrochemical measurements can be analyzed by a mass spectrometer (MS) which is connected to the gas outlet of the electrochemical cell. However, MS is not a quantitative method. Therefore, calibrations are needed for each electrode to approximately calculate the gaseous products and the faradaic efficiencies (FE) for the products. In our experiments, only H_2 is calibrated since H_2 is the main gaseous product as we observed in the electrochemical measurements with CO_2 purging.

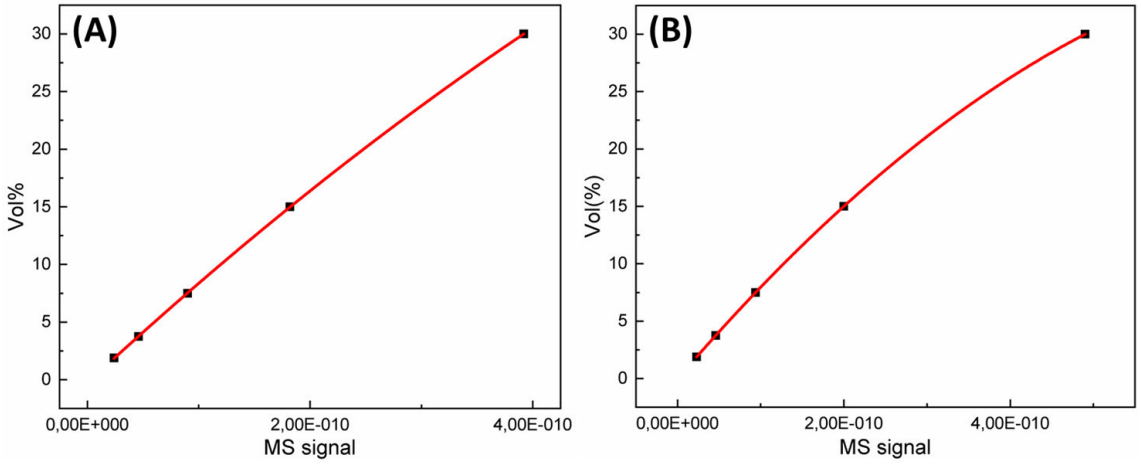

Figure 5.3: *H_2 calibration of MoS_2 sputtered at* 470 °C *in different gases: (A) Ar; (B) CO_2*

The calibration process for sample sputtered at 470 °C are taken as an example. And the calibration curve of sample prepared at RT are shown in Fig. A.15 in Ap-

pendix A. Since the mass signal of H_2 is dependent on the volume concentration of H_2 in the outlet, H_2 mass signals with different concentrations in Ar and CO_2 are measured respectively and the results are shown in Fig. 5.3.

According to the calibration curves, the volume concentration of H_2 could be approximately calculated from MS signals. Since 250 mL/h CO_2 was purged during the electrochemical measurement, and no large signals of other gaseous products from CO_2RR can be observed from MS signals, the gas leaving the cell mainly consists of H_2 and CO_2. Therefore, the volume concentration of the H_2 in the outlet gas can be formulated as:

$$R_{H_2} = \frac{v_{H_2}}{v_{all}} = \frac{v_{H_2}}{250 + v_{H_2} - v_{CO_2}} \tag{5.1}$$

In this equation, R_{H_2} stands for the volume concentration of H_2 in the outlet gas, v_{H_2} is the velocity of H_2 production and the unit is mL/h, v_{CO_2} is the velocity of CO_2 consumption in mL/h and v_{all} is the volume flow rate of the gas outlet.

Meanwhile, the hydrogen partial current in the electrochemical measurement can be calculated by the following equation:

$$I_{H_2} = \frac{nF \cdot v_{H_2}}{V_m \cdot 3600} \tag{5.2}$$

F in the equation is the faradaic constant which is 96 485 As/mol, n is the number of eletrons needed to produce one H_2 molecule and in this case n equals to 2, and V_m is the molar volume of the gas which is 24.5 L/mol at room temperature. From these two equations, the partial current of HER can be calculated and then the FE of hydrogen production can be formulated as:

$$FE_{H_2} = \frac{I_{H_2}}{I_{all}} \tag{5.3}$$

I_{all} is the overall current obtained from the electrochemical measurements. In an ideal case where no other reactions happen, the overall current should be equal to the sum of the HER and CO_2RR currents.

Catalytic ability of MoS_2 sputtered at different temperatures

Samples deposited at RT and 470 °C were chosen as examples to study their catalytic ability with respect to CO_2RR. Fig. 5.5 shows the LSV results of MoS_2 electrodes measured in CO_2 saturated 0.5 M $KHCO_3$ and K_2SO_4 electrolyte (pH 7.5) under CO_2 purging. As shown in this figure, molybdenum sulfide electrodes on GDE substrates can achieve relatively high current densities ($\sim$100 mA/cm^2 at -2 V). The current of the RT sputtered sample onsets at about -0.75 V vs. the standard

hydrogen electrode (SHE) while the current of the MoS_2 sputtered at 470 °C onsets at about −0.8 V vs. SHE. However, the current of the MoS_2 layer sputtered at 470 °C increases more steeply than the RT sputtered sample when the potential goes negatively which may suggest different catalytic mechanisms.

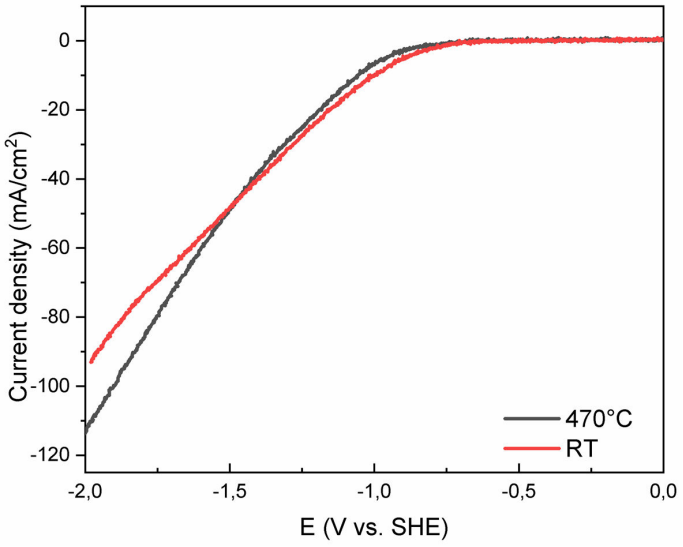

Figure 5.4: *CV curves of RT sputtered MoS_x and* 470 °C *sputtered MoS_2 on GDE substrates in* 0.5 M *$KHCO_3$ +* 0.5 M *K_2SO_4 aqueous electrolyte with* 250 mL/h *CO_2 purging*

The MS signals of these two samples during LSV are shown in Fig. 5.4 as a function of applied potential vs. SHE. As mentioned before, the main gas product of molybdenum sulfide electrodes in the LSV measurement is hydrogen. The MS signals of hydrogen are shown by the red curves in Fig. 5.5. The H_2 signal of the RT sputtered sample starts to increase at about −0.8 V while the H_2 signal of the sample sputtered at 470 °C starts to increase at −0.9 V. Only one clear MS signal has been observed originating from CO_2RR in the LSV measurement having a mass/charge ratio of 29. Since no potential-dependent change of signal 31 could be observed, the signal 29 could probably be from the formation of formaldehyde which has a molar mass of 30 g/mol, other than methanol which has a molar mass of 32 g/mol. The peak of the signal 29 observed between −0.3 V and −1 V vs. SHE shown in Fig. 5.5A from the RT sputtered sample always appear with the release of H_2S. Similar peaks can be found at the signal 15, 32 and 44 which are also correlated to the release of H_2S. However, the reason for the impact of H_2S on these signals is not clear yet and will be studied in the future.

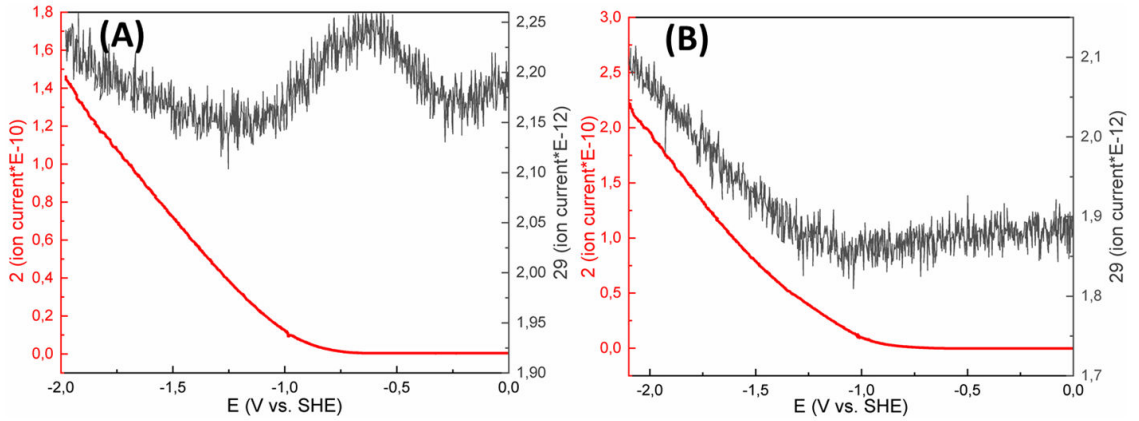

Figure 5.5: *MS signal of 2 and 29 during LSV in the potential range from* 0 V *to* −2 V *with* CO_2 *purging: (A) RT sputtered* MoS_x*;(B)* 470 °C *sputtered* MoS_2

Combining the calibration curves shown in Fig. 5.3 and A.15, the ratio of H_2 in the gas outlet and the related FE of HER can be calculated from the MS results.
In addition, to detect the liquid products, HS-GC and HPLC are performed. Only very low amounts of ethanol and methanol, formaldehyde could be detected in the electrolyte samples at the end of LSV and potentiostatic measurements at −700 mV (<0.1 mM). Therefore, the main product from CO_2RR with molybdenum sulfide samples could be formaldehyde which is also formed in small amount only.
For the MoS_2 sample sputtered at 470 °C, it can be speculated from Eq. 5.1 that if all the current was attributed to HER, the ratio of H_2 in the gas outlet could be calculated by the equation:

$$R_{H_2} = \frac{v_{H_2}}{v_{all}} = \frac{v_{H_2}}{250 + v_{H_2}} \tag{5.4}$$

Then at −2 V, according to the observed current, around 13.09% of H_2 , while the ratio of H_2 calculated from the calibration curve (see Fig. 5.3) and the current (see Fig. 5.4) is around 10.63% and a FE of around 80% of hydrogen production could be approximately calculated as shown in Fig. 5.6. Compared to the FE of H_2 production with Ar purging as shown in Fig. 5.3B, the values at potential more negative than −1.4 V is similar while the value of Ar purging measurement is smaller when the potential is positive than −1.4 V. Possible reason for that could be with CO_2 purging, the electrolyte is more acidic which favors HER than other reactions, therefore at low overpotential range (0 - −1.4 V), the FE of hydrogen is higher with CO_2 purging. As soon as the potential goes negatively, the applied overpotential for HER is relatively high, so most of the current goes to hydrogen production as well, which makes the FE for hydrogen production similar, when purging with CO_2 and Ar. At potential lower than −1.6 V, the FE of the sample with CO_2 purging for H_2

is lower than the one purged with Ar, which suggests that this small part of the current could be assigned to CO_2RR since we assume the current obtained with Ar purging doesn't contain much CO_2RR because there is no continuous CO_2 supply except the little amount of CO_2 dissolved in the electrolyte. Similar calculations of the FE of RT sputtered MoS_x electrode is shown in Fig. A.16 where the FE of hydrogen production almost reach 100% at about −2 V vs. SHE. For both figures, the calibration fitting in the region where applied potential is more positive than −1.2 V could be inaccurate since the hydrogen was not calibrated for this low ratios.

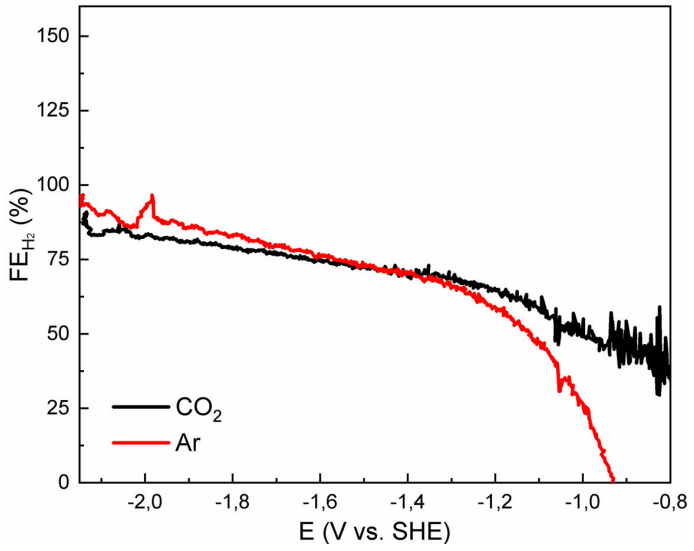

Figure 5.6: *Faradaic efficiency of MoS_2 sputtered at 470 °C plotted as a function of applied potential: with Ar purging (red); with CO_2 purging*

From these measurements, it can be concluded that both the RT sputtered sample and the sample prepared at 470 °C are more active as HER catalyst than CO_2 since only small amount of products such as formaldehyde, methanol and ethanol have been detected.

5.3 Conclusion

Molybdenum sulfide films with different degrees of crystallinity can be prepared on GDE substrates using reactive magnetron sputtering by varying the substrate temperature. The sample prepared at RT and at 470 °C were tested with respect to their catalytic ability for CO_2RR. According to the results of the electrochemical

measurements and the study of the products, both samples obtained high current densities. However, most of the current is from hydrogen evolution and only a very low amount from the formation of formaldehyde, methanol and ethanol, which means HER is more competitive than CO_2RR when molybdenum sulfide is used as catalyst. This result may suggest that combining molybdenum sulfide with another catalyst or doping with other elements that can suppress its catalytic ability for HER, could be a strategy to further develop MoS_2 as an efficient CO_2RR catalyst.

Chapter 6

Conclusion

A transition from fossil fuels to sustainable energy resources is required to stop a further accumulation of CO_2 in the atmosphere, which is responsible for the global warming. Solar fuels have attracted much attention since they can convert the intermittent solar power and store it in the form of chemical bonds. Among them, hydrogen production by water splitting and hydrocarbon production by CO_2 reduction driven by solar energy, are two most studied topics. Molybdenum sulfide was chosen in this thesis as a promising catalyst for both reactions.

From previous studies, it is known that the active sites of hexagonal molybdenum sulfide with a layer structure, are the edge sites while the basal planes of the material are catalytically inert. Different strategies have been tested to improve its catalytic ability and many studies have been performed to understand its catalytic mechanism. In this thesis, the study of molybdenum sulfide catalysts mainly consists of three parts: (i) the study of the catalytic performance and catalytic mechanism for $(NH_4)_2Mo_3S_{13}$ cluster compounds as electro-catalyst and co-catalyst in a $WSe_2/(NH_4)_2Mo_3S_{13}$ hetero-junction, (ii) the phase transformation during the activation of amorphous MoS_x as a hydrogen evolving catalyst, (iii) molybdenum sulfides deposited on gas diffusion electrodes as a catalyst candidate for the CO_2 reduction reaction.

In Chapter 3 of this thesis, $(NH_4)_2Mo_3S_{13}$ clusters were investigated as an electrocatalyst for hydrogen evolution reaction. Best catalytic activity of $(NH_4)_2Mo_3S_{13}$ has been obtained by depositing thin layers of $(NH_4)_2Mo_3S_{13}$ using dimethyl sulfoxide as slovent. Its overpotential is about 220 mV at a current density of $-10\,mA/cm^2$. From DFT calculations, the terminal sulfide atoms in the Mo_3S_{13} cluster could be identified as the catalytic active sites in HER. The thermal stability of the cluster material was also studied to order to study its behavior during heat treatment at higher temperatures. In addition, the $(NH_4)_2Mo_3S_{13}$ cluster was deposited on p-

type WSe_2 photocathodes as a co-catalyst. By this means, the photocurrent of the electrode increased from $0.02\,mA/cm^2$ to $2.4\,mA/cm^2$ at 0 V vs. RHE. This effect could be explained by the semiconducting properties of $(NH_4)_2Mo_3S_{13}$. As an intrinsic semiconductor itself with a direct band gap of 1.9 eV, it has been proven by intensity modulated photocurrent spectroscopy and open circuit potential difference measurements that $(NH_4)_2Mo_3S_{13}$ can passivate the surface states of WSe_2 and form a hetero-junction with WSe_2. Combining the band positions of $(NH_4)_2Mo_3S_{13}$ and WSe_2 measured by Kelvin probe, the band structure of the $WSe_2/(NH_4)_2Mo_3S_{13}$ electrode could be constructed showing a beneficial band bending for hydrogen evolution.

In Chapter 4, molybdenum sulfide films were prepared by reactive magnetron sputtering at different substrate temperatures. The samples sputtered at room temperature are XRD amorphous and the crystallinity of the films increases with substrate temperature. Best catalytic activity was obtained from the room temperature sputtered, amorphous MoS_x films, which are initially composed of Mo_3S_{13} and Mo_3S_{12} units. In the beginning of the electrochemical cycling, an activation of the catalyst film can be observed such that its catalytic ability as a hydrogen evolving catalyst improved remarkably, along with a release of H_2S and a change of the sulfur content. By *in-situ*/in-line Raman measurements, a phase transformation of the RT sputtered MoS_x film, from an amorphous structure to a layer-type MoS_{2-x} with sulfur defects on the edge sites was discovered. Therefore, after activation, the catalytic ability of amorphous MoS_x is no longer attributed to the existence of terminal and bridging $[S_2]^{2-}$ in the Mo_3S_{13} entities, but to unsaturated Mo atoms located on the edge sites of the MoS_{2-x} nano-islands.

In Chapter 5, molybdenum sulfide samples were prepared on GDE substrates by reactive magnetron sputtering. Samples prepared at RT and 470 °C were chosen as examples to be tested as catalysts for CO_2 reduction. Although high current density could be obtained from both samples, the current is mainly assigned to hydrogen evolution since the faradaic efficiency for HER is over 80% and only a small amount of products from CO_2RR could be addressed, such as formaldehyde, methanol and ethanol. To improve its selectivity towards CO_2RR rather than HER, a combination of molybdenum sulfide with other catalysts or doping/alloying of molybdenum sulfide with other elements has to be tested in future studies.

Appendix A

Appendix 1: Supplementary information

Figure A.1: *Optical photographs of $(NH_4)_2Mo_3S_{13}$ spin-coated on FTO (left) and bare FTO substrate (right)*

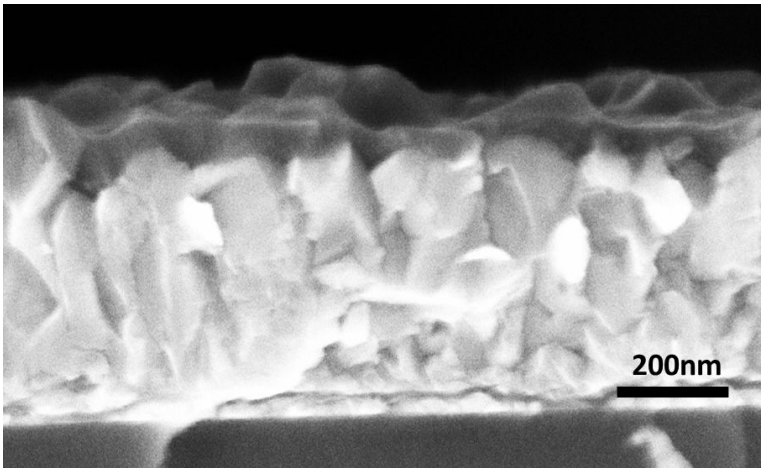

Figure A.2: *Cross-section SEM of 5-layer spin-coated $(NH_4)_2Mo_3S_{13}$ on FTO substrate*

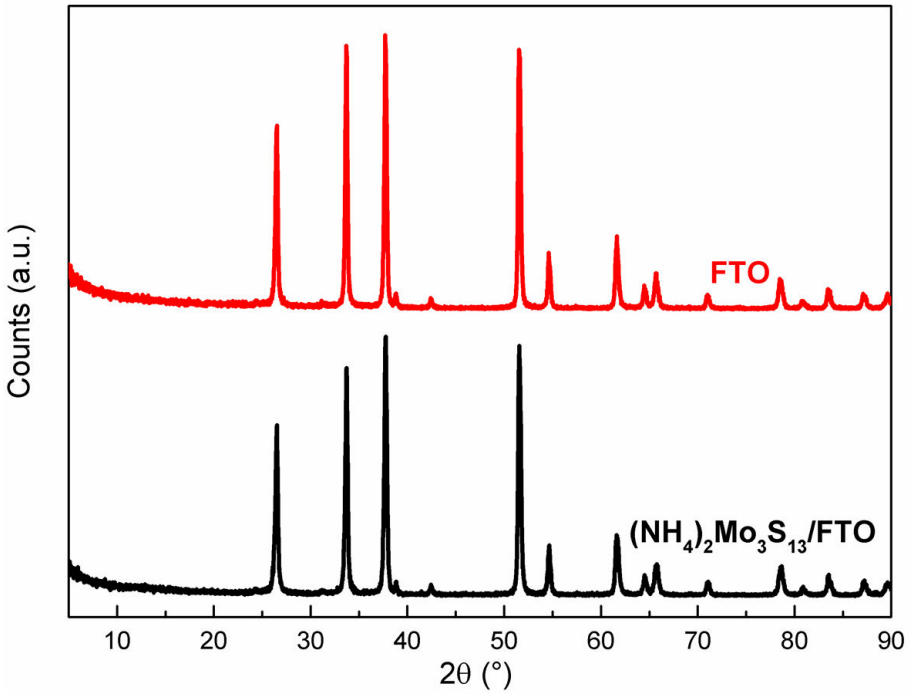

Figure A.3: *XRD patterns of spin-coated $(NH_4)_2Mo_3S_{13}$ on FTO (red curve) and bare FTO substrate (black curve)*

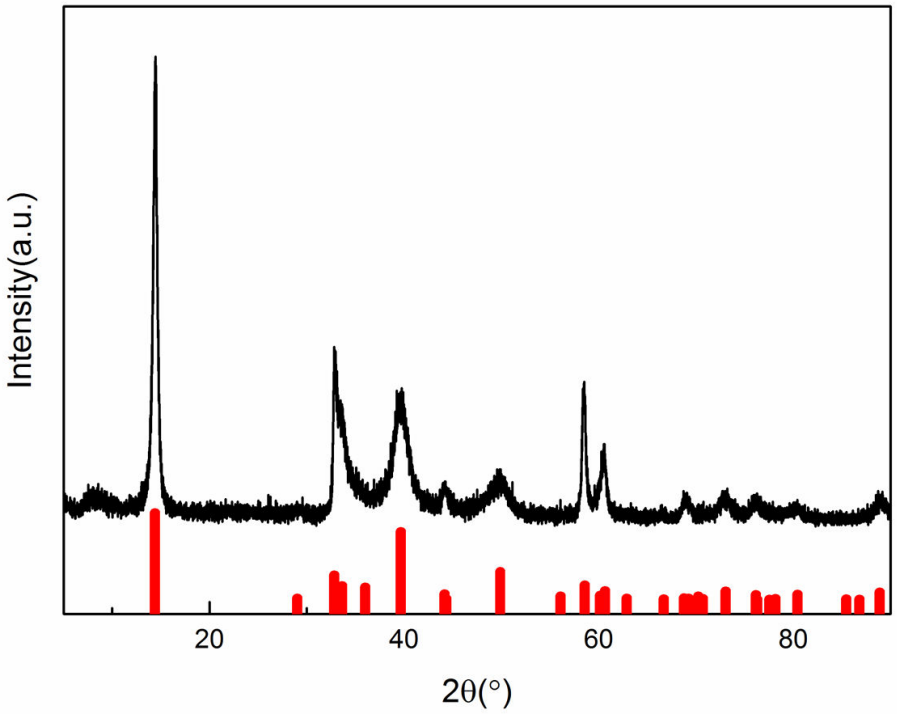

Figure A.4: *XRD patterns of $(NH_4)_2Mo_3S_{13}$ powder after TG (black) with standard 2H-MoS_2 (red)*

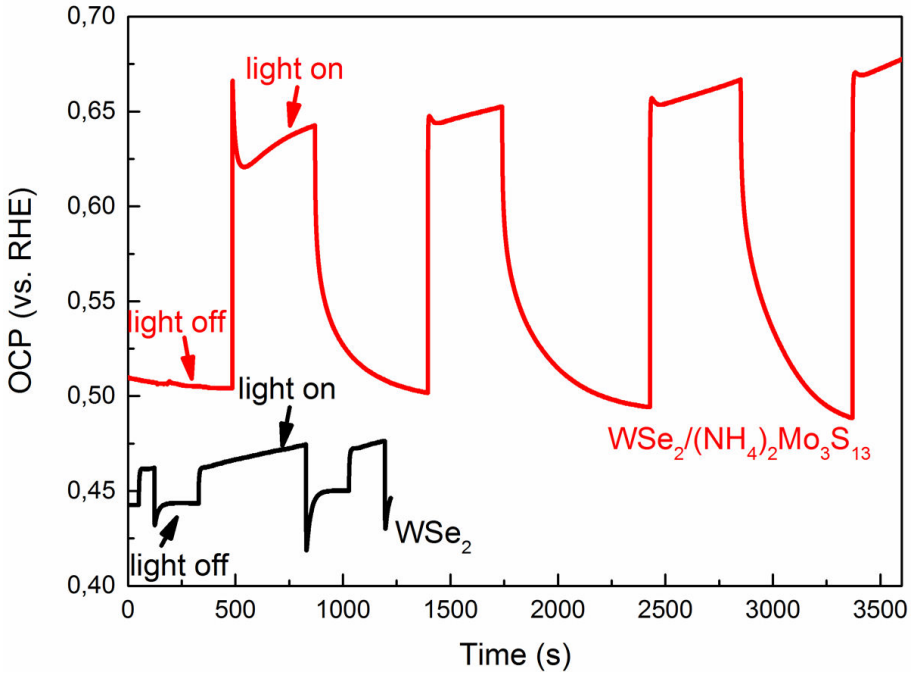

Figure A.5: *ΔOCP measurement under illumination with Ar ion laser: WSe_2 (black), $WSe_2/(NH_4)_2Mo_3S_{13}$ (red)*

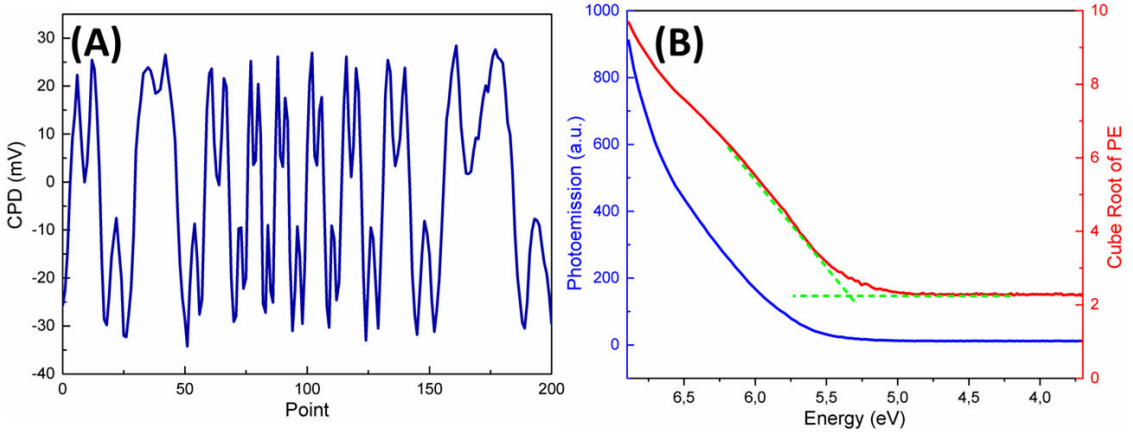

Figure A.6: *Kelvin Probe measurements of WSe_2: (A) CPD measurement (Φ_{tip}=5.028 V, ΔCPD=29mV); (B) AES measurement*

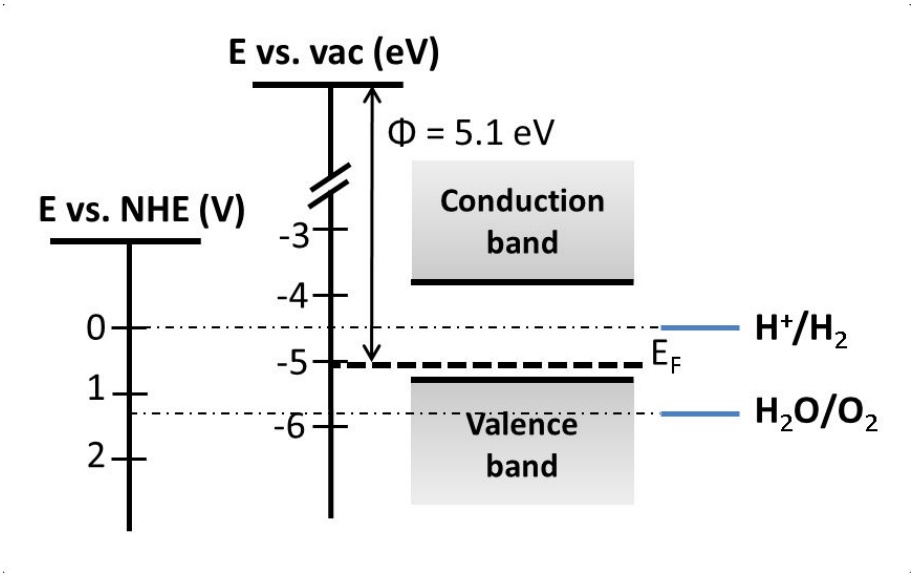

Figure A.7: *Band alignment of WSe_2 with respect to vacuum level and NHE potential*

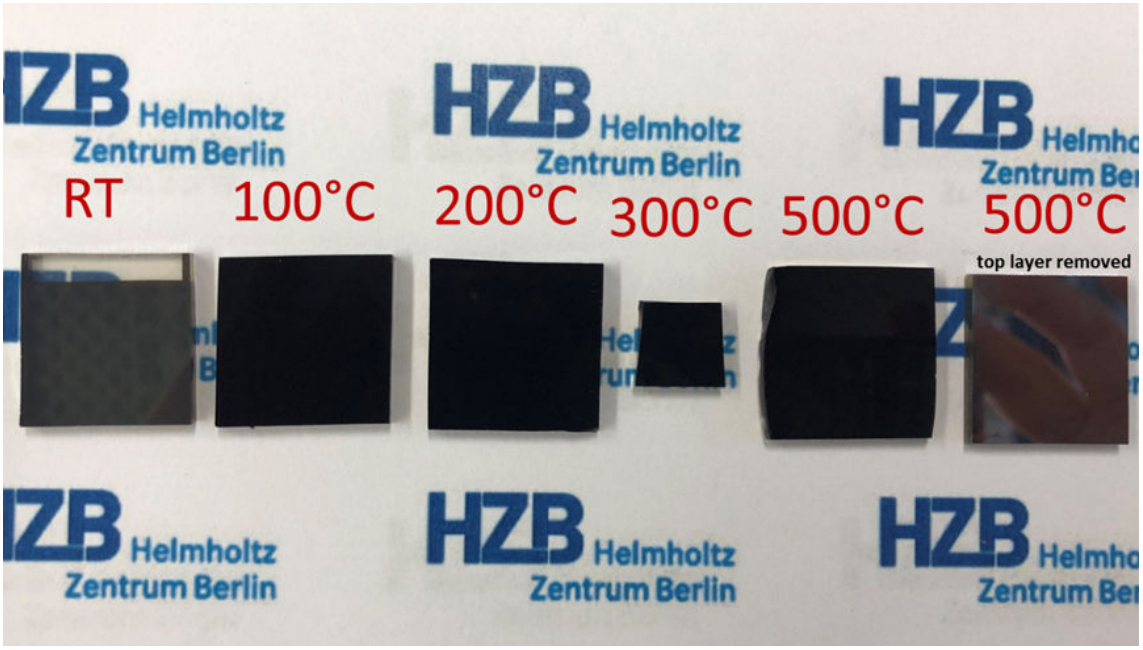

Figure A.8: *Optical photographs of molybdenum sulfide films sputtered at different temperatures on FTO substrates (the first sample on the right side: MoS_2 deposited at* 500 °C *with top layer removed)*

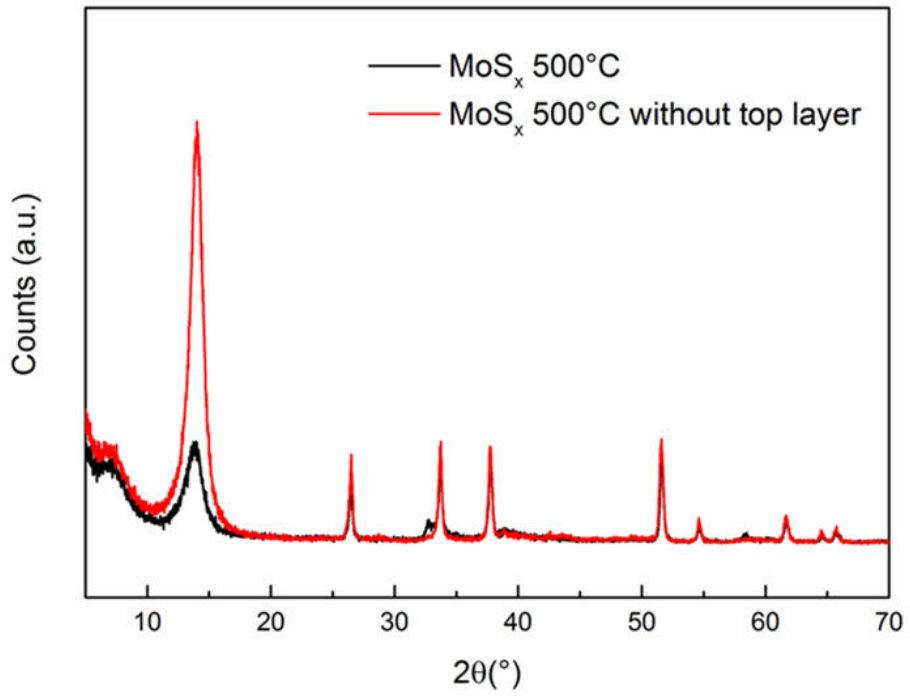

Figure A.9: *XRD patterns of MoS_2 electrodes sputtered at* 500 °C *as grown (black curve) and after removal of the porous layer on top (red curve)*

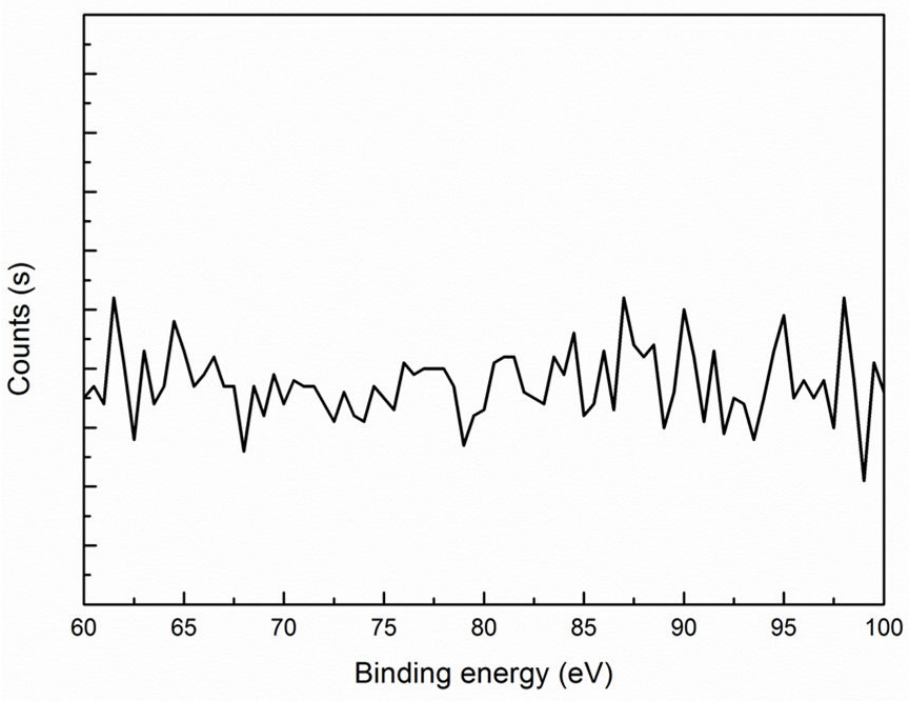

Figure A.10: *Pt 4f spectrum of RT sputtered MoS_x after* 2 h *CV cycling*

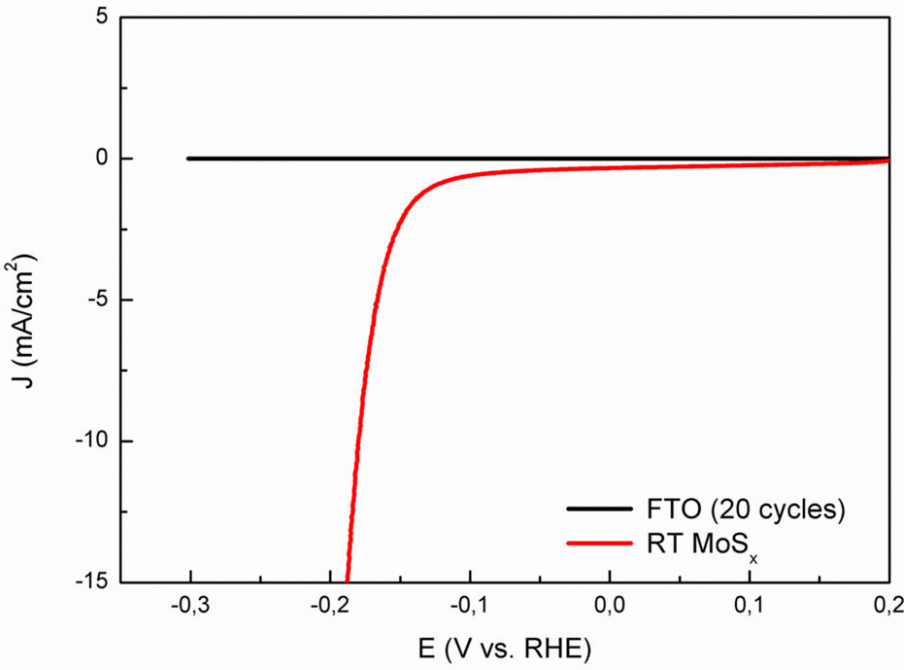

Figure A.11: *CV of FTO substrate for 20 CV cycles (33 min) compared to CV of RT sputtered* MoS_x

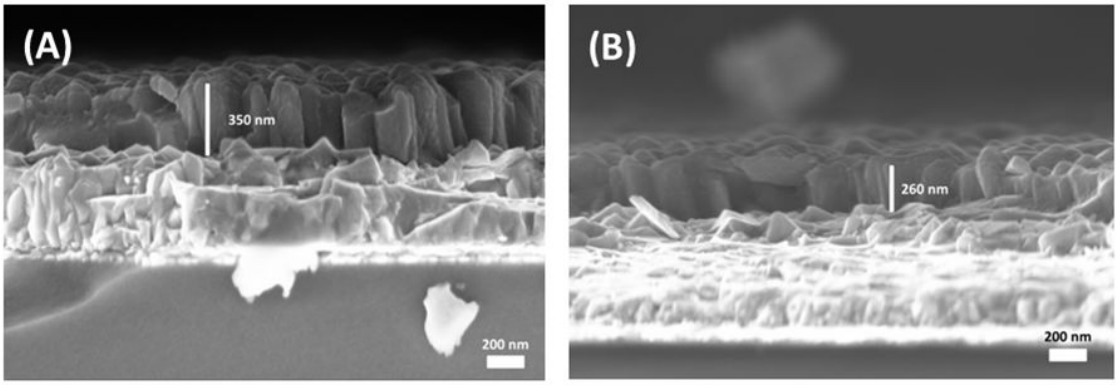

Figure A.12: *Cross-section SEM figures of (A) as-prepared RT sputtered* MoS_x*; (B) RT sputtered* MoS_x *after* 10 min *electrochemical cycling*

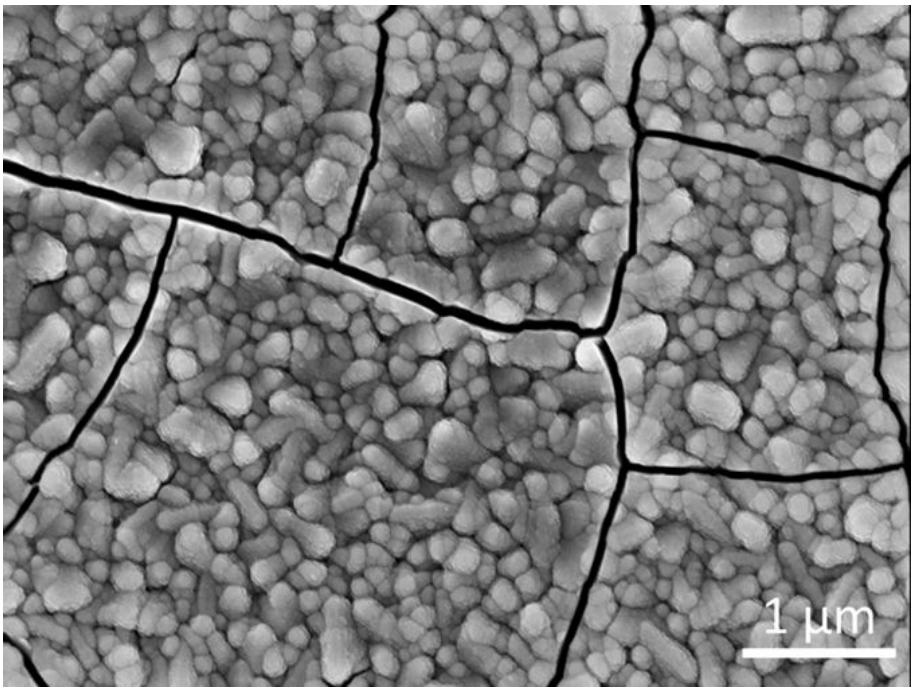

Figure A.13: *SEM top-view morphology of RT sputtered MoS_x after* 2 h *electrochemical cycling*

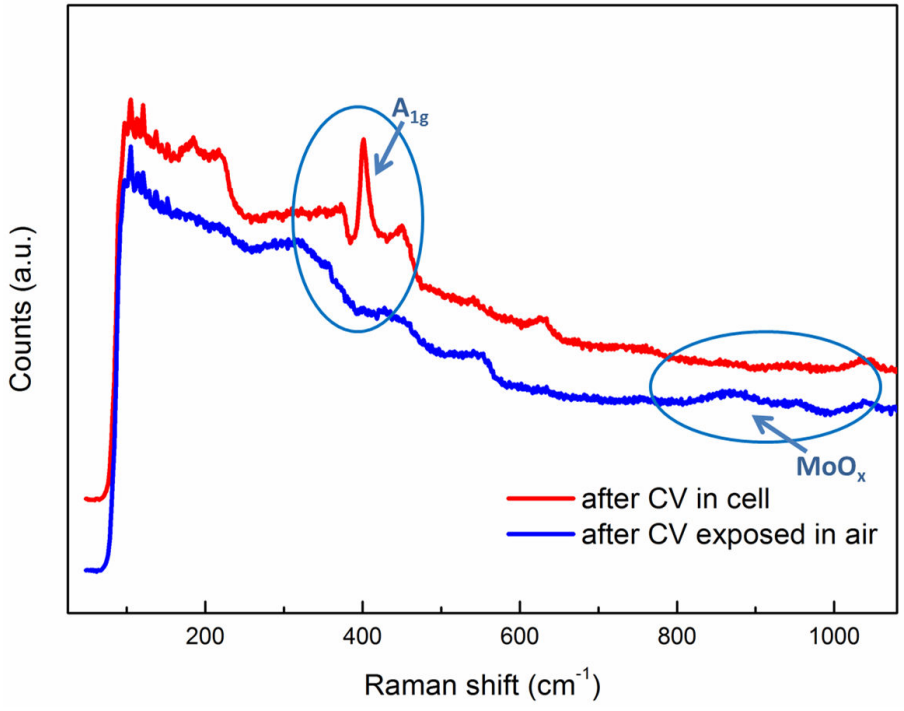

Figure A.14: *Raman spectra of RT sputtered MoS_x after activation (original electrode shown by red curve and electrode after exposure to air shown by blue curve*

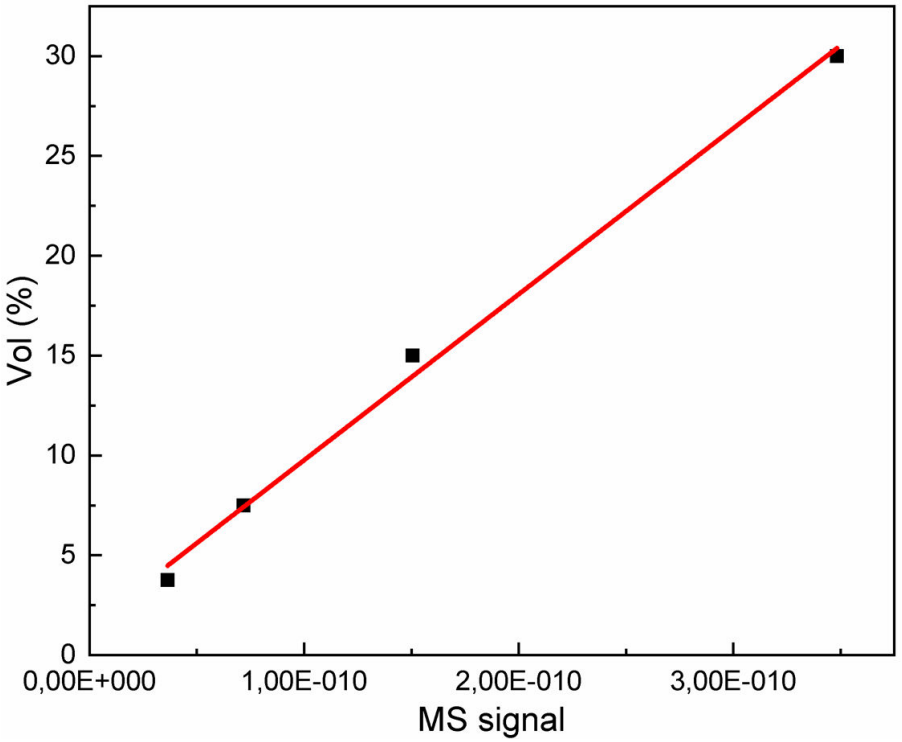

Figure A.15: *H_2 calibration of RT sputtered MoS_x in CO_2 gas*

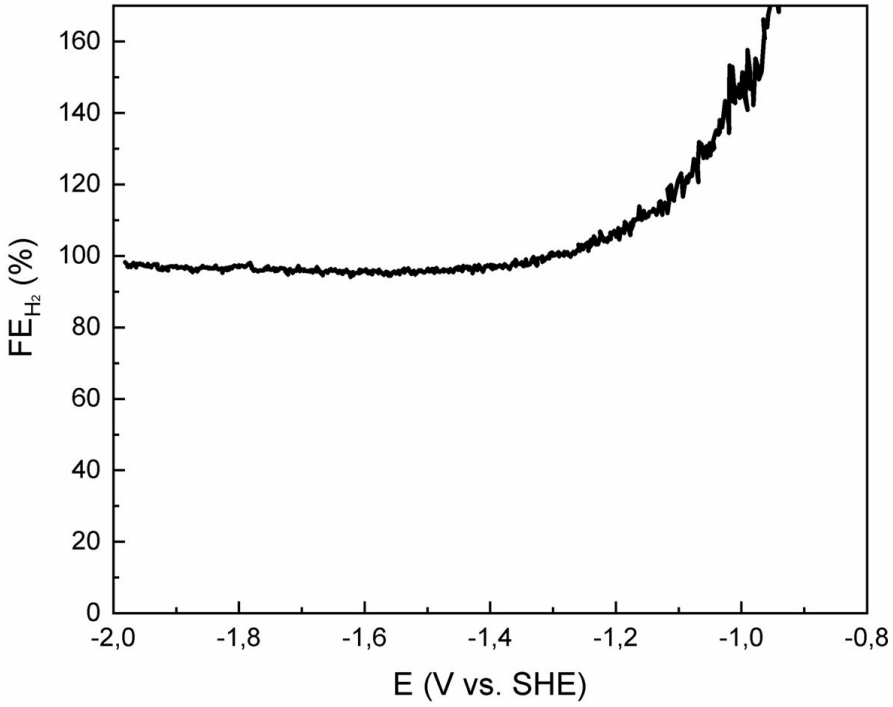

Figure A.16: *Faradaic efficiency of MoS_2 sputtered at RT with CO_2 purging plotted as a function of applied potential*

Appendix B

Appendix 2: List of publications

Xi F, Bogdanoff P, Harbauer K, et al. Structural transformation identification of sputtered amorphous MoSx as efficient hydrogen evolving catalyst during electrochemical activation. *ACS Catalysis*, 2019. **DOI: 10.1021/acscatal.8b04884**

Xi F, et al. $(NH_4)_2Mo_3S_{13}$ as electrocatalyst and semiconducting co-catalyst on WSe_2 photocathode for water splitting. *In preparation.*

Bozheyev F, Xi F, et al. Efficient charge transfer at a homogeneously distributed $(NH_4)_2Mo_3S_{13}/WSe_2$ heterojunction for solar hydrogen evolution. *Journal of Materials Chemistry A*, 2019. **DOI: 10.1039/C9TA01220F**

Appendix C

Appendix 3: List of abbreviations

List of abbreviations

aSLcS	solid-liquid crystalline solid process
A	Absorptance
AM1.5	Air mass 1.5 (terrestrial solar spectrum where the sun is 41° above the horizon)
APS	Ambient pressure photoemission spectroscopy
ATM	Ammonium thiomolybdate ($(NH_4)_2Mo_3S_{13}$)
CBM	Conduction band minimum
CE	Counter electrode
CO_2RR	CO_2 reduction reaction
C_H	Capacitance of the Helmholtz-double layer
CPD	Contact potential difference
C_{SC}	Capacitance of the space charge layer
CV	Cyclic voltammogram
DEMS	Differential electrochemical mass spectrometry
DFT	Density functional theory
DOS	Density of states
$E_{binding}$	Binding energy of the electrons
E_F	Fermi level
E_g	Bandgap
E_{ph}	Photon energy
E_{vac}	Vacuum energy level
FE	Faradaic efficiency
FID	Flame ionization detector

FTO	Fluorine-doped tin oxide
GC	Gas chromatography
GDE	Gas diffusion electrode
GDL	Gas diffusion layer
h	Planck's constant
HER	Hydrogen evolution reaction
HPLC	High performance liquid chromatography
HS-GC	Headspace gas chromatography
j_e	Electron current density
j_{photo}	Photocurrent
LSV	linear scan voltammetry
MS	Mass spectrometry
NHE	Normal hydrogen electrode
OER	Oxygen evolution reaction
OCP	Open circuit potential
PEC	Photoelectrochemical
QW	Quartz window
R	Reflectance
RE	Reference electrode
RHE	Reversible hydrogen electrode
RT	Room temperature
sccm	Standard cubic centimeters per minute
SEM	Scanning electron microscopy
SHE	Standard hydrogen electrode
STH	Solar to hydrogen
T	Transmittance
TGA	Thermogravimetric analysis
TR	Transflectance
UV-vis	Ultraviolet-visible
VBM	Valence band maximum
WE	Working electrode
XPS	X-ray photoelectron spectroscopy
XRD	X-ray diffraction

α	Absorption coefficient
λ	Wavelength
η	Overpotential
η_{CS}	Fraction of minority carriers reach the semicondutor surface
η_{CT}	Fraction of minority carriers transfers from semiconductor to electrolyte
η_{LH}	Light harvesting efficiency
φ	Illumination intensity
Φ	Work function

Appendix D

Acknowledgement

Many people have helped me during my study.
First of all, I would like to give my thanks to my supervisor, Prof. Sebastian Fiechter, who was always willing to help me with any difficulties I had during my study in here, and gave me many good suggestions for both my experiments and writing. In the meantime, I would also like to thank Prof. Roel van de Krol for providing such a great working environment with nice equipments and also for his constant feedback on my work.
Additionally, I am really honored to be a student of Prof. Frank Behrendt who made my study at the Technische Universität Berlin possible, and enjoyed the fruitful discussions with him. And I am grateful to him for giving me good suggestions and also for reading my thesis.
I would like to thank Peter Bogdanoff for the his great help in electrochemistry, especially for the DEMS and CO_2RR systems. Fatwa Abdi and Sean berglund are gratefully acknowledged for their help in photoelectrochemistry, for instance IMPS, Mott-Schottky and OCP measurements. Abdelkrim Chemseddine provided me nice chemistry labs for material synthesis. And Karsten Harbauer helped me a lot in reactive magnetron sputtering. I also want to thank Dennis Ehrhardt, Laura Pardo Perez, Sasho Stojkovikj, Alexander Arndt for their help in the characterization of CO_2RR products, Jörg Rappich for the *in-situ*/inline Raman measurement, Christian Höhn and Paul Plate, Marco Favaro for XPS analysis, Marin Rusu for Kelvin Probe measurements, Xiaoyu Han from University College London for DFT calculations and Ulrike Bloeck for TEM measurements. Thanks to Alexander Esau for the help with sample preparation, electrochemical measurements and German translation for my thesis. Thanks also go to Prince Bassi, Ibbi Ahmet and Matthew Mayer for correcting my thesis. Other group members like Moritz Kölbach, Merlene Lamers, Angang Songand Rowshanak Irani, also helped me a lot in many different

aspects.
Last but not least, I would like to thank my parents for their love and support during my study in Germany. Although they live very far away in China and we couldn't see each other quite often, I am always loved. Besides, I would also like to thank Zi for understanding me, bearing me, and encouraging me during my PhD.

Bibliography

[1] Co2 ice core data. *https://www.co2.earth/co2-ice-core-data*, 2018.

[2] Thomas Stocker. *Climate change 2013: the physical science basis: Working Group I contribution to the Fifth assessment report of the Intergovernmental Panel on Climate Change*. Cambridge University Press, 2014.

[3] Marc Perez and Richard Perez. Update 2015–a fundamental look at supply side energy reserves for the planet. *Natural Gas*, 2(9):215, 2015.

[4] Xiaoxin Zou and Yu Zhang. Noble metal-free hydrogen evolution catalysts for water splitting. *Chemical Society Reviews*, 44(15):5148–5180, 2015.

[5] Jingshan Luo, Jeong-Hyeok Im, Matthew T Mayer, Marcel Schreier, Mohammad Khaja Nazeeruddin, Nam-Gyu Park, S David Tilley, Hong Jin Fan, and Michael Grätzel. Water photolysis at 12.3% efficiency via perovskite photovoltaics and earth-abundant catalysts. *Science*, 345(6204):1593–1596, 2014.

[6] Kevin Sivula and Roel Van De Krol. Semiconducting materials for photoelectrochemical energy conversion. *Nature Reviews Materials*, 1(2):15010, 2016.

[7] Fatwa F Abdi and Sean P Berglund. Recent developments in complex metal oxide photoelectrodes. *Journal of Physics D: Applied Physics*, 50(19):193002, 2017.

[8] Roel Van de Krol. Principles of photoelectrochemical cells. In *Photoelectrochemical hydrogen production*, pages 13–67. Springer, 2012.

[9] Nian-Tzu Suen, Sung-Fu Hung, Quan Quan, Nan Zhang, Yi-Jun Xu, and Hao Ming Chen. Electrocatalysis for the oxygen evolution reaction: recent development and future perspectives. *Chemical Society Reviews*, 46(2):337–365, 2017.

[10] Charles CL McCrory, Suho Jung, Ivonne M Ferrer, Shawn M Chatman, Jonas C Peters, and Thomas F Jaramillo. Benchmarking hydrogen evolving reaction and oxygen evolving reaction electrocatalysts for solar water splitting devices. *Journal of the American Chemical Society*, 137(13):4347–4357, 2015.

[11] Yoshio Hori, Katsuhei Kikuchi, and Shin Suzuki. Production of co and ch4 in electrochemical reduction of co2 at metal electrodes in aqueous hydrogencarbonate solution. *Chemistry Letters*, 14(11):1695–1698, 1985.

[12] Alexander Bagger, Wen Ju, Ana Sofia Varela, Peter Strasser, and Jan Rossmeisl. Electrochemical co2 reduction: a classification problem. *ChemPhysChem*, 18(22):3266–3273, 2017.

[13] Rulle Reske, Hemma Mistry, Farzad Behafarid, Beatriz Roldan Cuenya, and Peter Strasser. Particle size effects in the catalytic electroreduction of co2 on cu nanoparticles. *Journal of the American Chemical Society*, 136(19):6978–6986, 2014.

[14] Bing Han and Yun Hang Hu. Mos2 as a co-catalyst for photocatalytic hydrogen production from water. *Energy Science & Engineering*, 4(5):285–304, 2016.

[15] Agnieszka Kuc. Low-dimensional transition-metal dichalcogenides. *Chem. Modell*, 11(1), 2014.

[16] Thomas F Jaramillo, Kristina P Jørgensen, Jacob Bonde, Jane H Nielsen, Sebastian Horch, and Ib Chorkendorff. Identification of active edge sites for electrochemical h2 evolution from mos2 nanocatalysts. *science*, 317(5834):100–102, 2007.

[17] Jakob Kibsgaard, Zhebo Chen, Benjamin N Reinecke, and Thomas F Jaramillo. Engineering the surface structure of mos 2 to preferentially expose active edge sites for electrocatalysis. *Nature materials*, 11(11):963, 2012.

[18] Hong Li, Charlie Tsai, Ai Leen Koh, Lili Cai, Alex W Contryman, Alex H Fragapane, Jiheng Zhao, Hyun Soo Han, Hari C Manoharan, Frank Abild-Pedersen, et al. Activating and optimizing mos 2 basal planes for hydrogen evolution through the formation of strained sulphur vacancies. *Nature materials*, 15(1):48, 2016.

[19] Thomas F Jaramillo, Jacob Bonde, Jingdong Zhang, Bee-Lean Ooi, Klas Andersson, Jens Ulstrup, and Ib Chorkendorff. Hydrogen evolution on supported incomplete cubane-type [mo3s4] 4+ electrocatalysts. *The Journal of Physical Chemistry C*, 112(45):17492–17498, 2008.

[20] Jakob Kibsgaard, Thomas F Jaramillo, and Flemming Besenbacher. Building an appropriate active-site motif into a hydrogen-evolution catalyst with thiomolybdate [mo 3 s 13] 2- clusters. *Nature chemistry*, 6(3):248, 2014.

[21] Carlos G Morales-Guio and Xile Hu. Amorphous molybdenum sulfides as hydrogen evolution catalysts. *Accounts of chemical research*, 47(8):2671–2681, 2014.

[22] Sonja A Francis, Jesus M Velazquez, Ivonne M Ferrer, Daniel A Torelli, Dan Guevarra, Matthew T McDowell, Ke Sun, Xinghao Zhou, Fadl H Saadi, Jimmy John, et al. Reduction of aqueous co2 to 1-propanol at mos2 electrodes. *Chemistry of Materials*, 30(15):4902–4908, 2018.

[23] Pedram Abbasi, Mohammad Asadi, Cong Liu, Soroosh Sharifi-Asl, Baharak Sayahpour, Amirhossein Behranginia, Peter Zapol, Reza Shahbazian-Yassar, Larry A Curtiss, and Amin Salehi-Khojin. Tailoring the edge structure of molybdenum disulfide toward electrocatalytic reduction of carbon dioxide. *ACS nano*, 11(1):453–460, 2016.

[24] Carolin Zachäus, Fatwa F Abdi, Laurence M Peter, and Roel Van De Krol. Photocurrent of bivo 4 is limited by surface recombination, not surface catalysis. *Chemical science*, 8(5):3712–3719, 2017.

[25] Roel Van de Krol and Michael Grätzel. *Photoelectrochemical hydrogen production*, volume 90. Springer, 2012.

[26] Nathan S Lewis and Daniel G Nocera. Powering the planet: Chemical challenges in solar energy utilization. *Proceedings of the National Academy of Sciences*, 103(43):15729–15735, 2006.

[27] Personalized energy presentation at poptech.

[28] AllenJ Bard. *Standard potentials in aqueous solution*. Routledge, 2017.

[29] Jinli Qiao, Yuyu Liu, Feng Hong, and Jiujun Zhang. A review of catalysts for the electroreduction of carbon dioxide to produce low-carbon fuels. *Chemical Society Reviews*, 43(2):631–675, 2014.

[30] Shahriar Shafiee and Erkan Topal. When will fossil fuel reserves be diminished? *Energy policy*, 37(1):181–189, 2009.

[31] NASA. Global climate change. *https://climate.nasa.gov/effects/*, 2018.

[32] George W Crabtree and Nathan S Lewis. Solar energy conversion. *Physics today*, 60(3):37–42, 2007.

[33] Martin A Green. Solar cells: operating principles, technology, and system applications. *Englewood Cliffs, NJ, Prentice-Hall, Inc., 1982. 288 p.*, 1982.

[34] Soteris A Kalogirou. Solar thermal collectors and applications. *Progress in energy and combustion science*, 30(3):231–295, 2004.

[35] Fatwa Firdaus Abdi. *Towards highly efficient bias-free solar water splitting*. PhD thesis, TU Delft, Delft University of Technology, 2013.

[36] Peter CK Vesborg, Brian Seger, and IB Chorkendorff. Recent development in hydrogen evolution reaction catalysts and their practical implementation. *The journal of physical chemistry letters*, 6(6):951–957, 2015.

[37] Mary Rakowski Dubois and Daniel L Dubois. Development of molecular electrocatalysts for co2 reduction and h2 production/oxidation. *Accounts of Chemical Research*, 42(12):1974–1982, 2009.

[38] Yufei Zhao, Yuxia Zhang, Zhiyu Yang, Yiming Yan, and Kening Sun. Synthesis of mos2 and moo2 for their applications in h2 generation and lithium ion batteries: a review. *Science and technology of advanced materials*, 14(4):043501, 2013.

[39] T Jesper Jacobsson, Viktor Fjällström, Marika Edoff, and Tomas Edvinsson. Sustainable solar hydrogen production: from photoelectrochemical cells to pv-electrolyzers and back again. *Energy & Environmental Science*, 7(7):2056–2070, 2014.

[40] O Khaselev, A Bansal, and JA Turner. High-efficiency integrated multijunction photovoltaic/electrolysis systems for hydrogen production. *International Journal of Hydrogen Energy*, 26(2):127–132, 2001.

[41] PJ Boddy. Oxygen evolution on semiconducting tio2. *Journal of the Electrochemical Society*, 115(2):199–203, 1968.

[42] Akira Fujishima and Kenichi Honda. Electrochemical photolysis of water at a semiconductor electrode. *nature*, 238(5358):37, 1972.

[43] Fatwa F Abdi, Lihao Han, Arno HM Smets, Miro Zeman, Bernard Dam, and Roel Van De Krol. Efficient solar water splitting by enhanced charge separation in a bismuth vanadate-silicon tandem photoelectrode. *Nature communications*, 4:2195, 2013.

[44] Roel van de Krol, Yongqi Liang, and Joop Schoonman. Solar hydrogen production with nanostructured metal oxides. *Journal of Materials Chemistry*, 18(20):2311–2320, 2008.

[45] Oscar Khaselev and John A Turner. A monolithic photovoltaic-photoelectrochemical device for hydrogen production via water splitting. *Science*, 280(5362):425–427, 1998.

[46] Wen-Hui Cheng, Matthias H Richter, Matthias M May, Jens Ohlmann, David Lackner, Frank Dimroth, Thomas Hannappel, Harry A Atwater, and Hans-Joachim Lewerenz. Monolithic photoelectrochemical device for direct water splitting with 19% efficiency. *ACS Energy Letters*, 3(8):1795–1800, 2018.

[47] Prince Saurabh Bassi, Rajini P Antony, Pablo P Boix, Yanan Fang, James Barber, and Lydia Helena Wong. Crystalline fe2o3/fe2tio5 heterojunction nanorods with efficient charge separation and hole injection as photoanode for solar water oxidation. *Nano Energy*, 22:310–318, 2016.

[48] Fuxian Wang, Wilman Septina, Abdelkrim Chemseddine, Fatwa F Abdi, Dennis Friedrich, Peter Bogdanoff, Roel van de Krol, S David Tilley, and Sean P Berglund. Gradient self-doped cubi2o4 with highly improved charge separation efficiency. *Journal of the American Chemical Society*, 139(42):15094–15103, 2017.

[49] Xia Long, Jinkai Li, Shuang Xiao, Keyou Yan, Zilong Wang, Haining Chen, and Shihe Yang. A strongly coupled graphene and feni double hydroxide hybrid as an excellent electrocatalyst for the oxygen evolution reaction. *Angewandte Chemie*, 126(29):7714–7718, 2014.

[50] Yang Zhao, Fei Zhao, Xiaopeng Wang, Chenyu Xu, Zhipan Zhang, Gaoquan Shi, and Liangti Qu. Graphitic carbon nitride nanoribbons: graphene-assisted formation and synergic function for highly efficient hydrogen evolution. *Angewandte Chemie International Edition*, 53(50):13934–13939, 2014.

[51] Ju Seong Kim, Byunghoon Kim, Hyunah Kim, and Kisuk Kang. Recent progress on multimetal oxide catalysts for the oxygen evolution reaction. 2018.

[52] Tobias Reier, Mehtap Oezaslan, and Peter Strasser. Electrocatalytic oxygen evolution reaction (oer) on ru, ir, and pt catalysts: a comparative study of nanoparticles and bulk materials. *Acs Catalysis*, 2(8):1765–1772, 2012.

[53] Muhammad Tahir, Lun Pan, Faryal Idrees, Xiangwen Zhang, Li Wang, Ji-Jun Zou, and Zhong Lin Wang. Electrocatalytic oxygen evolution reaction for energy conversion and storage: a comprehensive review. *Nano Energy*, 37:136–157, 2017.

[54] Rasmus Frydendal, Elisa A Paoli, Brian P Knudsen, Björn Wickman, Paolo Malacrida, Ifan EL Stephens, and Ib Chorkendorff. Benchmarking the stability of oxygen evolution reaction catalysts: the importance of monitoring mass losses. *ChemElectroChem*, 1(12):2075–2081, 2014.

[55] R.+ Kötz, HJ Lewerenz, and S Stucki. Xps studies of oxygen evolution on ru and ruo2 anodes. *Journal of The Electrochemical Society*, 130(4):825–829, 1983.

[56] Thandavarayan Maiyalagan, Karalee A Jarvis, Soosairaj Therese, Paulo J Ferreira, and Arumugam Manthiram. Spinel-type lithium cobalt oxide as a bifunctional electrocatalyst for the oxygen evolution and oxygen reduction reactions. *Nature communications*, 5:3949, 2014.

[57] Alejandra Ramírez, Philipp Hillebrand, Diana Stellmach, Matthias M May, Peter Bogdanoff, and Sebastian Fiechter. Evaluation of mno x, mn2o3, and mn3o4 electrodeposited films for the oxygen evolution reaction of water. *The Journal of Physical Chemistry C*, 118(26):14073–14081, 2014.

[58] Minrui Gao, Wenchao Sheng, Zhongbin Zhuang, Qianrong Fang, Shuang Gu, Jun Jiang, and Yushan Yan. Efficient water oxidation using nanostructured α-nickel-hydroxide as an electrocatalyst. *Journal of the American Chemical Society*, 136(19):7077–7084, 2014.

[59] Matthew W Kanan, Junko Yano, Yogesh Surendranath, Mircea Dinca, Vittal K Yachandra, and Daniel G Nocera. Structure and valency of a cobalt-phosphate water oxidation catalyst determined by in situ x-ray spectroscopy. *Journal of the American Chemical Society*, 132(39):13692–13701, 2010.

[60] Gregory Jerkiewicz. Hydrogen sorption atin electrodes. *Progress in Surface Science*, 57(2):137–186, 1998.

[61] J Barber, S Morin, and BE Conway. Specificity of the kinetics of h2 evolution to the structure of single-crystal pt surfaces, and the relation between opd and upd h. *Journal of Electroanalytical Chemistry*, 446(1-2):125–138, 1998.

[62] BE Conway and G Jerkiewicz. Relation of energies and coverages of underpotential and overpotential deposited h at pt and other metals to the 'volcano curve'for cathodic h2 evolution kinetics. *Electrochimica Acta*, 45(25-26):4075–4083, 2000.

[63] Jens Kehlet Nørskov, Thomas Bligaard, Ashildur Logadottir, JR Kitchin, Jingguang G Chen, S Pandelov, and U Stimming. Trends in the exchange current for hydrogen evolution. *Journal of the Electrochemical Society*, 152(3):J23–J26, 2005.

[64] Sergio Trasatti. Work function, electronegativity, and electrochemical behaviour of metals: Iii. electrolytic hydrogen evolution in acid solutions. *Journal of Electroanalytical Chemistry and Interfacial Electrochemistry*, 39(1):163–184, 1972.

[65] KC Neyerlin, Wenbin Gu, Jacob Jorne, and Hubert A Gasteiger. Study of the exchange current density for the hydrogen oxidation and evolution reactions. *Journal of The Electrochemical Society*, 154(7):B631–B635, 2007.

[66] Current (2009) state-of-the-art hydrogen production cost estimate using water electrolysis. *https://www.energy.gov/sites/prod/files/2014/03/f10/46676.pdf*, 2009.

[67] James R McKone, Bryce F Sadtler, Caroline A Werlang, Nathan S Lewis, and Harry B Gray. Ni–mo nanopowders for efficient electrochemical hydrogen evolution. *ACS catalysis*, 3(2):166–169, 2013.

[68] Daniel G Nocera. The artificial leaf. *Accounts of chemical research*, 45(5):767–776, 2012.

[69] Jakob Kibsgaard, Charlie Tsai, Karen Chan, Jesse D Benck, Jens K Nørskov, Frank Abild-Pedersen, and Thomas F Jaramillo. Designing an improved transition metal phosphide catalyst for hydrogen evolution using experimental and theoretical trends. *Energy & Environmental Science*, 8(10):3022–3029, 2015.

[70] Shengjie Peng, Linlin Li, Xiaopeng Han, Wenping Sun, Madhavi Srinivasan, Subodh G Mhaisalkar, Fangyi Cheng, Qingyu Yan, Jun Chen, and Seeram Ramakrishna. Cobalt sulfide nanosheet/graphene/carbon nanotube nanocomposites as flexible electrodes for hydrogen evolution. *Angewandte Chemie*, 126(46):12802–12807, 2014.

[71] Jieun Yang, Damien Voiry, Seong Joon Ahn, Dongwoo Kang, Ah Young Kim, Manish Chhowalla, and Hyeon Suk Shin. Two-dimensional hybrid nanosheets of tungsten disulfide and reduced graphene oxide as catalysts for enhanced hydrogen evolution. *Angewandte Chemie*, 125(51):13996–13999, 2013.

[72] Eric J Popczun, James R McKone, Carlos G Read, Adam J Biacchi, Alex M Wiltrout, Nathan S Lewis, and Raymond E Schaak. Nanostructured nickel phosphide as an electrocatalyst for the hydrogen evolution reaction. *Journal of the American Chemical Society*, 135(25):9267–9270, 2013.

[73] Eric J Popczun, Carlos G Read, Christopher W Roske, Nathan S Lewis, and Raymond E Schaak. Highly active electrocatalysis of the hydrogen evolution reaction by cobalt phosphide nanoparticles. *Angewandte Chemie International Edition*, 53(21):5427–5430, 2014.

[74] Peng Xiao, Mahasin Alam Sk, Larissa Thia, Xiaoming Ge, Rern Jern Lim, Jing-Yuan Wang, Kok Hwa Lim, and Xin Wang. Molybdenum phosphide as an efficient electrocatalyst for the hydrogen evolution reaction. *Energy & Environmental Science*, 7(8):2624–2629, 2014.

[75] Louis Schlapbach and Andreas Züttel. Hydrogen-storage materials for mobile applications. In *Materials for sustainable energy: a collection of peer-reviewed research and review articles from nature publishing group*, pages 265–270. World Scientific, 2011.

[76] Alan T Landers, Meredith Fields, Daniel A Torelli, Jianping Xiao, Thomas R Hellstern, Sonja A Francis, Charlie Tsai, Jakob Kibsgaard, Nathan S Lewis, Karen Chan, et al. The predominance of hydrogen evolution on transition metal sulfides and phosphides under co2 reduction conditions: An experimental and theoretical study. *ACS Energy Letters*, 3(6):1450–1457, 2018.

[77] Chuan Shi, Heine A Hansen, Adam C Lausche, and Jens K Nørskov. Trends in electrochemical co 2 reduction activity for open and close-packed metal surfaces. *Physical Chemistry Chemical Physics*, 16(10):4720–4727, 2014.

[78] Andrew A Peterson and Jens K Nørskov. Activity descriptors for co2 electroreduction to methane on transition-metal catalysts. *The Journal of Physical Chemistry Letters*, 3(2):251–258, 2012.

[79] Karen Chan, Charlie Tsai, Heine A Hansen, and Jens K Nørskov. Molybdenum sulfides and selenides as possible electrocatalysts for co2 reduction. *ChemCatChem*, 6(7):1899–1905, 2014.

[80] Truman E Teeter and Pierre Van Rysselberghe. Reduction of carbon dioxide on mercury cathodes. *The Journal of Chemical Physics*, 22(4):759–760, 1954.

[81] Yoshio Hori, Akira Murata, and Ryutaro Takahashi. Formation of hydrocarbons in the electrochemical reduction of carbon dioxide at a copper electrode in aqueous solution. *Journal of the Chemical Society, Faraday Transactions 1: Physical Chemistry in Condensed Phases*, 85(8):2309–2326, 1989.

[82] Line Sjolte Byskov, Bjørk Hammer, Jens Kehlet Nørskov, Bjerne S Clausen, and Henrik Topsøe. Sulfur bonding in mos 2 and co-mo-s structures. *Catalysis letters*, 47(3-4):177–182, 1997.

[83] RR Chianelli, TA Pecoraro, TR Halbert, W-H Pan, and EI Stiefel. Transition metal sulfide catalysis: Relation of the synergic systems to the periodic trends in hydrodesulfurization. *Journal of Catalysis*, 86(1):226–230, 1984.

[84] Han Wang, Lili Yu, Yi-Hsien Lee, Yumeng Shi, Allen Hsu, Matthew L Chin, Lain-Jong Li, Madan Dubey, Jing Kong, and Tomas Palacios. Integrated circuits based on bilayer mos2 transistors. *Nano letters*, 12(9):4674–4680, 2012.

[85] Harold E Sliney. Solid lubricant materials for high temperatures—a review. *Tribology International*, 15(5):303–315, 1982.

[86] AR Beal, JC Knights, and WY Liang. Transmission spectra of some transition metal dichalcogenides. ii. group via: trigonal prismatic coordination. *Journal of Physics C: Solid State Physics*, 5(24):3540, 1972.

[87] Sharmila N Shirodkar and Umesh V Waghmare. Emergence of ferroelectricity at a metal-semiconductor transition in a 1 t monolayer of mos 2. *Physical review letters*, 112(15):157601, 2014.

[88] D Yang, S Jiménez Sandoval, WMR Divigalpitiya, JC Irwin, and RF Frindt. Structure of single-molecular-layer mos 2. *Physical Review B*, 43(14):12053, 1991.

[89] Dattatray J Late, Bin Liu, HSS Ramakrishna Matte, Vinayak P Dravid, and CNR Rao. Hysteresis in single-layer mos2 field effect transistors. *ACS nano*, 6(6):5635–5641, 2012.

[90] Leopold Gmelin. *Handbuch der anorganischen Chemie*, volume 1. C. Winter, 1886.

[91] Kin Fai Mak, Changgu Lee, James Hone, Jie Shan, and Tony F Heinz. Atomically thin mos 2: a new direct-gap semiconductor. *Physical review letters*, 105(13):136805, 2010.

[92] H Tributsch. Layer-type transition metal dichalcogenides—a new class of electrodes for electrochemical solar cells. *Berichte der Bunsengesellschaft für physikalische Chemie*, 81(4):361–369, 1977.

[93] Daisuke Kiriya, Peter Lobaccaro, Hnin Yin Yin Nyein, Peyman Taheri, Mark Hettick, Hiroshi Shiraki, Carolin M Sutter-Fella, Peida Zhao, Wei Gao, Roya Maboudian, et al. General thermal texturization process of mos2 for efficient electrocatalytic hydrogen evolution reaction. *Nano letters*, 16(7):4047–4053, 2016.

[94] Daniel Merki, Stéphane Fierro, Heron Vrubel, and Xile Hu. Amorphous molybdenum sulfide films as catalysts for electrochemical hydrogen production in water. *Chemical Science*, 2(7):1262–1267, 2011.

[95] Jesse D Benck, Zhebo Chen, Leah Y Kuritzky, Arnold J Forman, and Thomas F Jaramillo. Amorphous molybdenum sulfide catalysts for electrochemical hydrogen production: insights into the origin of their catalytic activity. *Acs Catalysis*, 2(9):1916–1923, 2012.

[96] Jesse D Benck, Thomas R Hellstern, Jakob Kibsgaard, Pongkarn Chakthranont, and Thomas F Jaramillo. Catalyzing the hydrogen evolution reaction (her) with molybdenum sulfide nanomaterials. *Acs Catalysis*, 4(11):3957–3971, 2014.

[97] Heron Vrubel, Daniel Merki, and Xile Hu. Hydrogen evolution catalyzed by mos 3 and mos 2 particles. *Energy & Environmental Science*, 5(3):6136–6144, 2012.

[98] Daniel Merki, Heron Vrubel, Lorenzo Rovelli, Stéphane Fierro, and Xile Hu. Fe, co, and ni ions promote the catalytic activity of amorphous molybdenum sulfide films for hydrogen evolution. *Chemical Science*, 3(8):2515–2525, 2012.

[99] Louisa Rui Lin Ting, Yilin Deng, Liang Ma, Yin-Jia Zhang, Andrew A Peterson, and Boon Siang Yeo. Catalytic activities of sulfur atoms in amorphous molybdenum sulfide for the electrochemical hydrogen evolution reaction. *ACS Catalysis*, 6(2):861–867, 2016.

[100] Phong D Tran, Thu V Tran, Maylis Orio, Stephane Torelli, Quang Duc Truong, Keiichiro Nayuki, Yoshikazu Sasaki, Sing Yang Chiam, Ren Yi, Itaru Honma, et al. Coordination polymer structure and revisited hydrogen evolution catalytic mechanism for amorphous molybdenum sulfide. *Nature materials*, 15(6):640, 2016.

[101] Mark A Lukowski, Andrew S Daniel, Fei Meng, Audrey Forticaux, Linsen Li, and Song Jin. Enhanced hydrogen evolution catalysis from chemically exfoliated metallic mos2 nanosheets. *Journal of the American Chemical Society*, 135(28):10274–10277, 2013.

[102] Mohammad Asadi, Bijandra Kumar, Amirhossein Behranginia, Brian A Rosen, Artem Baskin, Nikita Repnin, Davide Pisasale, Patrick Phillips, Wei Zhu, Richard Haasch, et al. Robust carbon dioxide reduction on molybdenum disulphide edges. *Nature communications*, 5:4470, 2014.

[103] Mohammad Asadi, Kibum Kim, Cong Liu, Aditya Venkata Addepalli, Pedram Abbasi, Poya Yasaei, Patrick Phillips, Amirhossein Behranginia, José M Cerrato, Richard Haasch, et al. Nanostructured transition metal dichalcogenide electrocatalysts for co2 reduction in ionic liquid. *Science*, 353(6298):467–470, 2016.

[104] Fengwang Li, Shu-Feng Zhao, Lu Chen, Azam Khan, Douglas R MacFarlane, and Jie Zhang. Polyethylenimine promoted electrocatalytic reduction of co 2 to co in aqueous medium by graphene-supported amorphous molybdenum sulphide. *Energy & Environmental Science*, 9(1):216–223, 2016.

[105] Achim Müller, Sabyasachi Sarkar, Ram Gopal Bhattacharyya, Siegfried Pohl, and Mechtild Dartmann. Directed synthesis of [mo3s13] 2-, an isolated cluster containing sulfur atoms in three different states of bonding. *Angewandte Chemie International Edition in English*, 17(7):535–535, 1978.

[106] FM Penning and JHA Moubis. Cathode sputtering in a magnetic field. In *Proc. Kon. Ned. Akad. Wetensch*, volume 43, pages 41–56, 1940.

[107] S Swann. Magnetron sputtering. *Physics in technology*, 19(2):67, 1988.

[108] Sigracet gas diffusion layers for pem fuel cells, electrolyzers and batteries. *http://www.sglgroup.com*, 2016.

[109] MF Mathias, Joerg Roth, Jerry Fleming, and Werner Lehnert. Diffusion media materials and characterization. *Handbook of fuel cells—fundamentals, technology and applications*, 3:517–537, 2003.

[110] Ahmad El-Kharouf, Thomas J Mason, Dan JL Brett, and Bruno G Pollet. Ex-situ characterisation of gas diffusion layers for proton exchange membrane fuel cells. *Journal of Power Sources*, 218:393–404, 2012.

[111] Rong Chen, Cangjie Yang, Weizheng Cai, Hsin-Yi Wang, Jianwei Miao, Liping Zhang, Shengli Chen, and Bin Liu. Use of platinum as the counter electrode to study the activity of nonprecious metal catalysts for the hydrogen evolution reaction. *ACS Energy Letters*, 2(5):1070–1075, 2017.

[112] P Bogdanoff and N Alonso-Vante. A kinetic approach of competitive photoelectrooxidation of hcooh and h2o on tio2 anatase thin layers via on-line mass detection. *Journal of Electroanalytical Chemistry*, 379(1-2):415–421, 1994.

[113] LM Peter, J Li, and R Peat. Surface recombination at semiconductor electrodes: Part i. transient and steady-state photocurrents. *Journal of electroanalytical chemistry and interfacial electrochemistry*, 165(1-2):29–40, 1984.

[114] Halina K Dunn, Johann M Feckl, Alexander Müller, Dina Fattakhova-Rohlfing, Samuel G Morehead, Julian Roos, Laurence M Peter, Christina Scheu, and Thomas Bein. Tin doping speeds up hole transfer during light-driven water oxidation at hematite photoanodes. *Physical Chemistry Chemical Physics*, 16(44):24610–24620, 2014.

[115] Charles Y Cummings, Frank Marken, Laurence M Peter, Asif A Tahir, and KG Upul Wijayantha. Kinetics and mechanism of light-driven oxygen evolution at thin film α-fe 2 o 3 electrodes. *Chemical Communications*, 48(14):2027–2029, 2012.

[116] James E Thorne, Ji-Wook Jang, Erik Y Liu, and Dunwei Wang. Understanding the origin of photoelectrode performance enhancement by probing surface kinetics. *Chemical Science*, 7(5):3347–3354, 2016.

[117] Simon M Sze and Kwok K Ng. *Physics of semiconductor devices*. John wiley & sons, 2006.

[118] M Anwar and CA Hogarth. Optical properties of amorphous thin films of moo3 deposited by vacuum evaporation. *physica status solidi (a)*, 109(2):469–478, 1988.

[119] K Santra, CK Sarkar, MK Mukherjee, and B Ghosh. Copper oxide thin films grown by plasma evaporation method. *Thin Solid Films*, 213(2):226–229, 1992.

[120] F-P_ Koffyberg, K Dwight, and A Wold. Interband transitions of semiconducting oxides determined from photoelectrolysis spectra. *Solid State Communications*, 30(7):433–437, 1979.

[121] Rudy Schlaf. Tutorial on kelvin probe measurements. *Tampa: USF Surface Science Laboratory, Dept of Electrical Engineering at University of South Florida*, 2007.

[122] Ralph H Fowler. The analysis of photoelectric sensitivity curves for clean metals at various temperatures. *Physical review*, 38(1):45, 1931.

[123] H Tributsch. Solar energy-assisted electrochemical splitting of water. some energetical, kinetical and catalytical considerations verified on mos2 layer crystal surfaces. *Zeitschrift für Naturforschung A*, 32(9):972–985, 1977.

[124] H Tributsch and JC Bennett. Electrochemistry and photochemistry of mos2 layer crystals. i. *Journal of Electroanalytical Chemistry and Interfacial Electrochemistry*, 81(1):97–111, 1977.

[125] Jesse D Benck, Sang Chul Lee, Kara D Fong, Jakob Kibsgaard, Robert Sinclair, and Thomas F Jaramillo. Designing active and stable silicon photocathodes for solar hydrogen production using molybdenum sulfide nanomaterials. *Advanced Energy Materials*, 4(18):1400739, 2014.

[126] Thomas R Hellstern, Jakob Kibsgaard, Charlie Tsai, David W Palm, Laurie A King, Frank Abild-Pedersen, and Thomas F Jaramillo. Investigating catalyst–support interactions to improve the hydrogen evolution reaction activity of thiomolybdate [mo3s13] 2–nanoclusters. *ACS Catalysis*, 7(10):7126–7130, 2017.

[127] G Kline, K Kam, D Canfield, and BA Parkinson. Efficient and stable photoelectrochemical cells constructed with wse2 and mose2 photoanodes. *Solar Energy Materials*, 4(3):301–308, 1981.

[128] Achim Müller, V Wittneben, Erich Krickemeyer, Hartmut Bögge, and M Lemke. Studies on the triangular cluster [mo3s13] 2-: Electronic structure (xα calculations, xps), crystal structure of (ph4as) 2 [mo3s13]. 2ch3cn and a refinement of the crystal structure of (nh4) 2 [mo3s13]· h2o. *Zeitschrift für anorganische und allgemeine Chemie*, 605(1):175–188, 1991.

[129] Stephen Fletcher. Tafel slopes from first principles. *Journal of Solid State Electrochemistry*, 13(4):537–549, 2009.

[130] Farabi Bozheyev, Fanxing Xi, Paul Plate, Thomas Dittrich, Sebastian Fiechter, and Klaus Ellmer. Efficient charge transfer at a homogeneously distributed (nh 4) 2 mo 3 s 13/wse 2 heterojunction for solar hydrogen evolution. *Journal of Materials Chemistry A*, 2019.

[131] KG Upul Wijayantha, Sina Saremi-Yarahmadi, and Laurence M Peter. Kinetics of oxygen evolution at α-fe 2 o 3 photoanodes: a study by photoelectrochemical impedance spectroscopy. *Physical Chemistry Chemical Physics*, 13(12):5264–5270, 2011.

[132] EA Ponomarev and LM Peter. A generalized theory of intensity modulated photocurrent spectroscopy (imps). *Journal of Electroanalytical Chemistry*, 396(1-2):219–226, 1995.

[133] Seokhee Shin, Zhenyu Jin, Do Hyun Kwon, Ranjith Bose, and Yo-Sep Min. High turnover frequency of hydrogen evolution reaction on amorphous mos2 thin film directly grown by atomic layer deposition. *Langmuir*, 31(3):1196–1202, 2015.

[134] Shu Min Tan, Adriano Ambrosi, Zdeněk Sofer, Štěpán Huber, David Sedmidubskỳ, and Martin Pumera. Pristine basal-and edge-plane-oriented molybdenite mos2 exhibiting highly anisotropic properties. *Chemistry–A European Journal*, 21(19):7170–7178, 2015.

[135] JO'M Bockris and EC Potter. The mechanism of the cathodic hydrogen evolution reaction. *Journal of The Electrochemical Society*, 99(4):169–186, 1952.

[136] BE Conway and BV Tilak. Interfacial processes involving electrocatalytic evolution and oxidation of h2, and the role of chemisorbed h. *Electrochimica Acta*, 47(22-23):3571–3594, 2002.

[137] Allen J Bard and Larry R Faulkner. Electrochemical methods: fundamentals and applications. department of chemistry and biochemistry university of texas at austin, 2001.

[138] John Benson, Meixian Li, Shuangbao Wang, Peng Wang, and Pagona Papakonstantinou. Electrocatalytic hydrogen evolution reaction on edges of a few layer molybdenum disulfide nanodots. *ACS applied materials & interfaces*, 7(25):14113–14122, 2015.

[139] Th Weber, JC Muijsers, and JW Niemantsverdriet. Structure of amorphous mos3. *The Journal of Physical Chemistry*, 99(22):9194–9200, 1995.

[140] JC Muijsers, Th Weber, RM Vanhardeveld, H W_ Zandbergen, and JW Niemantsverdriet. Sulfidation study of molybdenum oxide using moo3/sio2/si (100) model catalysts and mo-iv3-sulfur cluster compounds. *Journal of Catalysis*, 157(2):698–705, 1995.

[141] Hernan G Sanchez Casalongue, Jesse D Benck, Charlie Tsai, Rasmus KB Karlsson, Sarp Kaya, May Ling Ng, Lars GM Pettersson, Frank Abild-Pedersen, JK Nørskov, Hirohito Ogasawara, et al. Operando characterization of an amorphous molybdenum sulfide nanoparticle catalyst during the hydrogen evolution reaction. *The Journal of Physical Chemistry C*, 118(50):29252–29259, 2014.

[142] Sang Chul Lee, Jesse D Benck, Charlie Tsai, Joonsuk Park, Ai Leen Koh, Frank Abild-Pedersen, Thomas F Jaramillo, and Robert Sinclair. Chemical and phase evolution of amorphous molybdenum sulfide catalysts for electrochemical hydrogen production. *ACS nano*, 10(1):624–632, 2015.

[143] Kevin Sivula, Florian Le Formal, and Michael Grätzel. Solar water splitting: progress using hematite (α-fe2o3) photoelectrodes. *ChemSusChem*, 4(4):432–449, 2011.

[144] Yanguang Li, Hailiang Wang, Liming Xie, Yongye Liang, Guosong Hong, and Hongjie Dai. Mos2 nanoparticles grown on graphene: an advanced catalyst for the hydrogen evolution reaction. *Journal of the American Chemical Society*, 133(19):7296–7299, 2011.

[145] Jacob Bonde, Poul G Moses, Thomas F Jaramillo, Jens K Nørskov, and Ib Chorkendorff. Hydrogen evolution on nano-particulate transition metal sulfides. *Faraday discussions*, 140:219–231, 2009.

[146] Haotian Wang, Zhiyi Lu, Desheng Kong, Jie Sun, Thomas M Hymel, and Yi Cui. Electrochemical tuning of mos2 nanoparticles on three-dimensional substrate for efficient hydrogen evolution. *ACS nano*, 8(5):4940–4947, 2014.

[147] Roger Parsons. The rate of electrolytic hydrogen evolution and the heat of adsorption of hydrogen. *Transactions of the Faraday Society*, 54:1053–1063, 1958.

[148] Phong D Tran, Lydia H Wong, James Barber, and Joachim SC Loo. Recent advances in hybrid photocatalysts for solar fuel production. *Energy & Environmental Science*, 5(3):5902–5918, 2012.

[149] Harry B Gray. Powering the planet with solar fuel. *Nature chemistry*, 1(1):7, 2009.

[150] Daniel Merki and Xile Hu. Recent developments of molybdenum and tungsten sulfides as hydrogen evolution catalysts. *Energy & Environmental Science*, 4(10):3878–3888, 2011.

[151] Shubin Yang, Yongji Gong, Jinshui Zhang, Liang Zhan, Lulu Ma, Zheyu Fang, Robert Vajtai, Xinchen Wang, and Pulickel M Ajayan. Exfoliated graphitic carbon nitride nanosheets as efficient catalysts for hydrogen evolution under visible light. *Advanced materials*, 25(17):2452–2456, 2013.

[152] Damien Voiry, Hisato Yamaguchi, Junwen Li, Rafael Silva, Diego CB Alves, Takeshi Fujita, Mingwei Chen, Tewodros Asefa, Vivek B Shenoy, Goki Eda, et al. Enhanced catalytic activity in strained chemically exfoliated ws 2 nanosheets for hydrogen evolution. *Nature materials*, 12(9):850, 2013.

[153] Nikolay Kornienko, Joaquin Resasco, Nigel Becknell, Chang-Ming Jiang, Yi-Sheng Liu, Kaiqi Nie, Xuhui Sun, Jinghua Guo, Stephen R Leone, and Peidong Yang. Operando spectroscopic analysis of an amorphous cobalt sulfide hydrogen evolution electrocatalyst. *Journal of the American Chemical Society*, 137(23):7448–7455, 2015.

[154] Lei Liao, Sinong Wang, Jingjing Xiao, Xiaojun Bian, Yahong Zhang, Micheál D Scanlon, Xile Hu, Yi Tang, Baohong Liu, and Hubert H Girault. A nanoporous molybdenum carbide nanowire as an electrocatalyst for hydrogen evolution reaction. *Energy & Environmental Science*, 7(1):387–392, 2014.

[155] Wei-Fu Chen, James T Muckerman, and Etsuko Fujita. Recent developments in transition metal carbides and nitrides as hydrogen evolution electrocatalysts. *Chemical communications*, 49(79):8896–8909, 2013.

[156] Cheng Wan, Yagya N Regmi, and Brian M Leonard. Multiple phases of molybdenum carbide as electrocatalysts for the hydrogen evolution reaction. *Angewandte Chemie*, 126(25):6525–6528, 2014.

[157] Yi-Hsien Lee, Xin-Quan Zhang, Wenjing Zhang, Mu-Tung Chang, Cheng-Te Lin, Kai-Di Chang, Ya-Chu Yu, Jacob Tse-Wei Wang, Chia-Seng Chang, Lain-Jong Li, et al. Synthesis of large-area mos2 atomic layers with chemical vapor deposition. *Advanced materials*, 24(17):2320–2325, 2012.

[158] TA Pecoraro and RR Chianelli. Hydrodesulfurization catalysis by transition metal sulfides. *Journal of Catalysis*, 67(2):430–445, 1981.

[159] S Helveg, J Vang Lauritsen, Erik Lægsgaard, Ivan Stensgaard, Jens Kehlet Nørskov, BS Clausen, H Topsøe, and Flemming Besenbacher. Atomic-scale structure of single-layer mos 2 nanoclusters. *Physical review letters*, 84(5):951, 2000.

[160] Jakob Kibsgaard and Thomas F Jaramillo. Molybdenum phosphosulfide: An active, acid-stable, earth-abundant catalyst for the hydrogen evolution reaction. *Angewandte Chemie International Edition*, 53(52):14433–14437, 2014.

[161] Berit Hinnemann, Poul Georg Moses, Jacob Bonde, Kristina P Jørgensen, Jane H Nielsen, Sebastian Horch, Ib Chorkendorff, and Jens K Nørskov. Biomimetic hydrogen evolution: Mos2 nanoparticles as catalyst for hydrogen evolution. *Journal of the American Chemical Society*, 127(15):5308–5309, 2005.

[162] Yun-Hyuk Choi, Junsang Cho, Allen M Lunsford, Mohammed Al-Hashimi, Lei Fang, and Sarbajit Banerjee. Mapping the electrocatalytic activity of mos 2 across its amorphous to crystalline transition. *Journal of Materials Chemistry A*, 5(10):5129–5141, 2017.

[163] John A Turner. Sustainable hydrogen production. *Science*, 305(5686):972–974, 2004.

[164] AR Beal and WY Liang. Excitons in 2h-wse2 and 3r-ws2. *Journal of Physics C: Solid State Physics*, 9(12):2459, 1976.

[165] Farabi Bozheyev, Dennis Friedrich, Man Nie, Mythili Rengachari, and Klaus Ellmer. Preparation of highly (001)-oriented photoactive tungsten diselenide (wse2) films by an amorphous solid–liquid-crystalline solid (aslcs) rapid-crystallization process. *physica status solidi (a)*, 211(9):2013–2019, 2014.

[166] Farabi Bozheyev, Karsten Harbauer, and Klaus Ellmer. Highly (001)-textured p-type wse 2 thin films as efficient large-area photocathodes for solar hydrogen evolution. *Scientific reports*, 7(1):16003, 2017.

[167] Marc TM Koper. Thermodynamic theory of multi-electron transfer reactions: Implications for electrocatalysis. *Journal of Electroanalytical Chemistry*, 660(2):254–260, 2011.

[168] Mohammed-Ibrahim Jamesh and Xiaoming Sun. Recent progress on earth abundant electrocatalysts for oxygen evolution reaction (oer) in alkaline medium to achieve efficient water splitting–a review. *Journal of Power Sources*, 400:31–68, 2018.

[169] Philipp Grosse, Dunfeng Gao, Fabian Scholten, Ilya Sinev, Hemma Mistry, and Beatriz Roldan Cuenya. Dynamic changes in the structure, chemical state and catalytic selectivity of cu nanocubes during co2 electroreduction: Size and support effects. *Angewandte Chemie*, 130(21):6300–6305, 2018.